



From particle scale to continuum modeling of size segregation in bedload transport : a theoretical and experimental study.

Hugo Rousseau

► To cite this version:

Hugo Rousseau. From particle scale to continuum modeling of size segregation in bedload transport : a theoretical and experimental study.. Hydrology. Université Grenoble Alpes [2020-..], 2021. English.
NNT : 2021GRALU029 . tel-03522599

HAL Id: tel-03522599

<https://theses.hal.science/tel-03522599>

Submitted on 12 Jan 2022

HAL is a multi-disciplinary open access archive for the deposit and dissemination of scientific research documents, whether they are published or not. The documents may come from teaching and research institutions in France or abroad, or from public or private research centers.

L'archive ouverte pluridisciplinaire **HAL**, est destinée au dépôt et à la diffusion de documents scientifiques de niveau recherche, publiés ou non, émanant des établissements d'enseignement et de recherche français ou étrangers, des laboratoires publics ou privés.

THÈSE

Pour obtenir le grade de

DOCTEUR DE L'UNIVERSITÉ GRENOBLE ALPES

Spécialité : Océan, Atmosphère, Hydrologie (CEOAH)

Arrêté ministériel : 25 mai 2016

Présentée par

Hugo ROUSSEAU

Thèse dirigée par **Philippe FREY** et **Julien CHAUCHAT**,
préparée au sein du **Laboratoire INRAE, UR ETNA**
dans l'**École Doctorale Sciences de la Terre de**
l'Environnement et des Planètes

**De l'échelle granulaire à la modélisation
continue du phénomène de ségrégation par
taille en transport par charriage : étude
théorique et expérimentale**

**From particle scale to continuum modeling of
size segregation in bedload transport: a
theoretical and experimental study**

Thèse soutenue publiquement le **17 Novembre 2021**,
devant le jury composé de :

M. Alexandre VALANCE

Directeur de recherche, CNRS, IPR, Université Rennes 1, Président

M. Eric LAJEUNESSE

Physicien, CNAP, IPGP, Rapporteur

M. Anthony R. THORNTON

Professor, University of Twente, Rapporteur

M. Christophe ANCEY

Professeur, EPFL, LHE, Examinateur

M. Philippe FREY

Chercheur HDR, INRAE, UR ETNA, Université Grenoble Alpes, Directeur de thèse

M. Julien CHAUCHAT

Maître de conférence, LEGI, Université Grenoble Alpes, Co-directeur de thèse

M. Raphaël MAURIN

Maître de conférence, IMFT, Toulouse INP, Invité



RÉSUMÉ

Dans les rivières, le transport de sédiments s'opère sous deux régimes. D'une part les sédiments transportés en suspension dans l'eau et d'autre part le charriage, représentant les particules transportées sur le fond du cours d'eau. En montagne où les pentes sont fortes le transport par charriage peut devenir intense, causant souvent de nombreux dégâts. Face à ce danger, prédire l'évolution morphologique de la rivière est primordiale. Pourtant, après plus d'un siècle de recherche moderne, ce phénomène reste mal compris. L'une des raisons provient du tri granulométrique, aussi appelé ségrégation par taille. Ce phénomène provient en grande partie d'interactions à l'échelle granulaire et impacte sensiblement le transport des sédiments et la morphologie des cours d'eau.

Si la physique des milieux granulaires semble indispensable pour mieux comprendre les interactions à l'échelle des grains, il est aussi nécessaire de recourir à la modélisation continue pour étudier les processus à grande échelle et ainsi mieux prévoir l'impact sur la géomorphologie des cours d'eau. L'objectif de cette thèse est de faire le lien entre les forces identifiées à l'échelle granulaire et la modélisation continue.

Grâce à des avancées sur la compréhension des forces de ségrégation, ([Tripathi and Khakhar, 2013](#); [Guillard et al., 2016](#)) une équation Lagrangienne théorique pour la ségrégation verticale d'un intrus dans un lit de petites particules est proposée. A partir de cette équation, un modèle 1D multi-phasique continu pour la ségrégation d'un ensemble de deux tailles de particules en transport par charriage est développé. Ce modèle est résolu numériquement et les résultats sont comparés à des simulations discrètes proposées par [Chassagne et al. \(2020b\)](#). Le modèle reproduit qualitativement les simulations discrètes et des dépendances supplémentaires permettent de reproduire quantitativement les résultats. Ces équations multi-phasiques permettent ensuite de proposer une équation d'advection-diffusion pour la ségrégation verticale par taille, sur le modèle de [Thornton et al. \(2006\)](#). Cela apporte une vision simplifiée du problème tout en gardant les paramètres physiques du processus à l'échelle granulaire.

Dans un second temps, des expériences en laboratoire ont été menées sur la ségrégation d'un intrus en transport par charriage dans un canal de pente 10% avec un lit de billes de verre. Deux nombres de Shields différents ont été explorés ainsi que huit ratios de tailles. Des techniques d'analyse d'images ont permis de suivre l'intrus dans le temps et l'espace ainsi que de déterminer le profil de vitesse du lit de petites particules. L'équation Lagrangienne proposée au début de ce travail a été comparée aux résultats expérimentaux et donne le bon comportement. Plus surprenant, la trajectoire de l'intrus apparaît comme linéaire avec une pente qui ne dépend ni du nombre de Shields, ni du ratio de taille. Ce comportement pourrait aider à mieux comprendre la dynamique de ségrégation d'un intrus dans les écoulements cisaillés.

ABSTRACT

Bedload transport, the coarser sediment load transported by the water flow in close contact with the mobile river bed, has consequences for public safety, water resources and fluvial ecology. After a century of modern research, bedload transport is still difficult to predict. The main reason pertains to size segregation. Size segregation largely originates from local interparticle interactions but has huge consequences on the particle size repartition both in the downward and streamwise directions over a much larger scale, affecting sediment mobility and the entire channel morphodynamics. The physics of granular media has been advocated to address segregation at the granular scale. While investigating segregation at the granular scale, usually with discrete methods, is invaluable, it is also necessary to consider continuum modelling to address larger scales, which requires a deep understanding of the physical processes at the granular scale. The aim of this theoretical and experimental PhD thesis is to bridge the gap between the granular scale processes and the continuum modelling.

Based on recent advances on the interaction forces between a large particle and its surrounding smaller particles ([Tripathi and Khakhar, 2013](#); [Guillard et al., 2016](#)), a theoretical equation for the vertical segregation of a large particle was proposed. Based on this equation, a 1D multi-phase continuum model for bidisperse vertical size segregation in bedload transport has been developed. The model was validated using results from discrete numerical simulations of [Chassagne et al. \(2020b\)](#). Our model qualitatively reproduced the results of the discrete numerical simulations but additional dependencies have been identified and made it possible to match quantitatively the discrete numerical simulations. This new continuum model also provided more physical parameters into the advection-diffusion equation for size segregation, proposed by [Thornton et al. \(2006\)](#). This work was published in *Journal of Fluid Mechanics* ([Rousseau et al., 2021](#)).

In a second step, the behaviour of a large intruder segregating in a bedload configuration was experimentally investigated in a 10% steep flume using spherical glass beads. Two different Shields numbers and eight size ratios were investigated. Image analysis was used to quantitatively track the large intruder and acquire the mean bed particle velocity profile. The theoretical vertical equation proposed for the large intruder was successfully compared to our experimental data. Surprisingly, it was found that large particles always segregate along a linear trajectory with an angle that is independent on the initial depth or the size ratio. This behaviour could help understand further the dynamics of segregation.

REMERCIEMENTS

Une thèse c'est trois années pour s'initier à la recherche par la recherche. C'est trois années particulièrement stimulantes intellectuellement, de belles rencontres, mais aussi du travail et de la persévérance. Un ami me disait que « ce qui compte ce n'est pas d'aller vite mais c'est d'aller longtemps » et je pense que l'on ne peut pas « aller longtemps » si l'on est pas bien entouré. Je profite donc de ces lignes pour remercier toutes les personnes qui ont contribué de près ou de loin à ce travail de longue haleine.

J'ai d'abord une pensée pour les personnes qui m'ont fait découvrir la recherche: Pascale Aussillous, Jacques Massoni et Laurence Bergougnoux à Marseille et Gauthier Rousseau et Christophe Ancey à Lausanne.

Mes remerciements vont ensuite aux membres du jury. Aux rapporteurs, Eric Lajeunesse et Anthony Thornton qui ont relu attentivement mon manuscrit, mais aussi à Alexandre Valance qui a accepté de présider mon jury. Soutenir ma thèse devant vous était une véritable chance. Vos commentaires et vos questions m'ont permis de prendre du recul sur mon travail et de discerner de futurs objectifs.

Bien évidemment, une thèse ne se fait pas sans encadrants et j'ai eu la chance d'être supervisé par une équipe de choc: « les trois mousquetaires ». D'abord, merci Raphaël Maurin, pour ton soutien sans faille et la qualité de tes conseils. Tes commentaires ont grandement amélioré mon travail et je retiendrai ta rigueur intellectuelle. Merci aussi pour tes encouragements quand parfois je doutais. Ton soutien m'a toujours motivé à poursuivre mes efforts. Ensuite, je te remercie Julien Chauchat. Ton encadrement à commencé avant ma thèse, lors de mon stage de fin d'étude, et j'ai beaucoup appris grâce à toi. Je retiendrai ton pragmatisme ainsi que ton intuition et je m'efforcerai de développer ces qualités dans la suite de mon parcours. Enfin, merci beaucoup Philippe Frey pour ton appui quotidien et pour l'autonomie que tu m'as laissé. Tu m'as aussi appris la rigueur expérimentale et je pense que c'est une de tes grandes qualités. Par la suite, j'espère pouvoir continuer à interagir avec vous trois.

À l'heure d'écrire ces lignes, je repense bien sûr à ma vie quotidienne à INRAE Grenoble. Lorsque j'arrive au bureau, il y a Charlie, déjà là depuis une heure. Charlie, c'est celui qui me suit dans mon humour et je dois dire que le bureau est désormais bien triste depuis que tu as déménagé si loin, dans le bureau d'en face. En général, Rémi Chassagne arrive quelques minutes après moi dans le bureau. Je crois que durant les deux ans où nous avons travaillé ensemble, les journées où nous n'avons pas tenté de comprendre la physique des milieux granulaires ensemble, au tableau, doivent se compter sur les doigts de la main. Travailler avec toi a été vraiment enrichissant. J'ai

beaucoup progressé grâce à ta vision et ma thèse n'aurait sûrement pas été la même sans nos interactions. Je te souhaite de la réussite pour la suite et j'espère que nous aurons encore l'occasion de collaborer.

Lors de nos pauses, nous descendons au bureau n° 27. Si ils sont là, Erwan, Cécile et Coline se font un plaisir de nous accueillir pour un thé, une tisane ou un café. Merci pour toutes ces super pauses et ces repas du midi. Ces petits moments ont participé à rendre les journées particulièrement agréables.

Merci aussi à toute celles et ceux qui rendent la vie du labo aussi plaisante. Merci aux doctorant·e·s : Suzanne, Cécile, Marco, Mohamad, Benjamin et Colin. Merci aux stagiaires que j'ai cotoyé: Adèle, Romain, Robin... Merci aux permanent·e·s et particulièrement à Florence, Guillaume, Thierry et Gaël, avec qui j'ai eu de très bonnes discussions. Merci à Rémi, Coline, Guillaume, Hugo et Firmin pour les séances de grimpe et les discussions montagne. Merci à Hervé, Christian et Alexis pour votre gentillesse ainsi que pour l'aide précieuse au labo et à l'atelier. C'était toujours génial d'échanger avec vous et de bénéficier de vos conseils. J'ai aussi une pensée pour Xavier. Je te remercie du fond du coeur pour avoir toujours fait en sorte de nous amener sur le terrain. Merci aussi aux agent·e·s d'entretiens qui nous permettent de travailler tous les jours dans de super conditions.

Dans cette histoire, il y a aussi les ami·e·s avec qui j'ai pu profiter de mon temps libre en m'épanouissant dans des sorties de montagne toujours plus longues et plus fatiguantes qu'une journée de travail. Alors merci Paulo, Ragnar, Noël, Léo, Ben, Anne et Max pour tous ces moments de partage. Je remercie aussi Maé, Claire, Tamara et Alex qui ont su me changer les idées à coup d'apéros et de soirées jeux.

Je finis ces lignes en remerciant ma famille. D'abord vous, Papa et Maman, qui m'avez permis de pouvoir rêver. Romain, Tiphaïne, je vous souhaite de la réussite dans vos futurs projets. Merci Lisa, ma partenaire de vie, toujours là pour me rassurer, m'écouter et relire mon anglais. Je te souhaite du courage pour finir ta thèse ! Et enfin, merci à Miage, mon chat, toujours présent pour réclamer des câlins (alors que je travail) ou pour écrire « jiofh5vpsd nws4hdhuivg » au milieu d'un article.

TABLE DES MATIÈRES

I Introduction	1
I.1 Context	1
I.2 Size segregation in granular media	4
I.2.1 Macroscopic description	5
I.2.2 Continuum modeling	6
I.2.3 Description at the particle scale	8
I.2.4 Grain-size segregation in the framework of bedload transport	12
I.3 Objectives and scope	14
I.4 Outline of the dissertation	15
II Theoretical modeling	17
II.1 A large intruder in a bed of small particles	18
II.1.1 General equation	18
II.1.2 Force balance on a large intruder segregating in a bed of small particles	19
II.1.3 Granular drag and lift forces	20
II.1.4 Dimensionless equation for the large intruder	22
II.2 Multi-phase flow model	24
II.2.1 3D general governing equations	24
II.2.2 Simplified 1D vertical multi-phase flow model	25
II.2.3 Closures for the granular stress	27
II.2.4 Numerical implementation	28
II.3 Advection-diffusion model	33
III Validation and Discussion	37
III.1 DEM investigation of segregation in bedload transport	38
III.2 Validation of the multi-phase flow model	41
III.3 Evaluation of the advection-diffusion model	43
III.4 Discussion	43
III.4.1 Investigation of the empirical segregation function \mathcal{F}_l	44
III.4.2 Missing dependencies in the particle-scale forces	46
III.4.3 Consistency of the model with the new formulations	50
III.4.4 Influence of the size ratio	51
III.5 Conclusion	52

TABLE DES MATIÈRES

IV Experiments	55
IV.1 Experimental setup	56
IV.2 Procedure	57
IV.3 Experimental constraints	57
IV.3.1 Constraint linked to the detection of the intruder	57
IV.3.2 Constraint linked to the bedload configuration	58
IV.4 Hydraulic and granular parameters	59
IV.5 Image processing	62
IV.6 Results	64
IV.7 Discussion	69
IV.7.1 Segregation dynamics	69
IV.7.2 Origin of the linear trajectory	73
IV.7.3 Assessing the particle-scale forces with our experiments	78
IV.8 Conclusion	82
V Conclusions & Perspectives	83
V.1 Conclusions	83
V.2 Perspectives	85
V.2.1 Refining closures for granular scale forces	85
V.2.2 Upscaling size segregation	87
V.2.3 Refining experiments on a single intruder	88
V.2.4 DEM simulations	89
A Numerical scheme for the multi-phase flow model	93
A.1 Discretisation for the mixture	93
A.1.1 Discretisation of the mixture mass conservation equation	95
A.1.2 Discretisation of the mixture momentum conservation equation	96
A.2 Velocity predictor step	97
A.3 Computing the pressure $\{p_f\}^*$	98
A.4 Velocity corrector step	100
B Image velocimetry processing	101
B.1 The <i>OpyFlow</i> toolbox	101
B.1.1 Step 1: Selecting the <i>good features to track</i>	101
B.1.2 Step 2: Velocimetry processing	102
B.1.3 step 3: Interpolation scheme	102
B.1.4 step 4: Streamwise velocity profile	103
B.2 Validation of the results	103
C Vanoni and Brooks sidewall correction	107
D Determination of the particle volume fraction	109
Bibliographie	110

TABLE DES FIGURES

I.1	(a) Damages caused by erosion and sediment transport in the Vésubie valley (source: La Provence). (b) Aerial image of a village in the Vésubie valley before and after the flood (source: Le Télégramme)	1
I.2	Polydispersity in a mountain stream (Vénéon river, La Bérarde, French Alps). In green the sand, in red the medium cobbles and in blue the large boulders.	3
I.3	Flow regime as a function of the inertial number I (from Andreotti et al. (2013))	6
I.4	Figures adapted from Duran et al. (1993). (a) Experimental observation for large steel disks of size ratio $r = 16$ (top picture) and $r = 2$ (bottom picture). (b) Photography of the 2D experiments showing the arching effect: the intruder is supported by the small particle arrangement on its right side. (c) Schematic diagram describing the vault effect (also called arching).	9
I.5	Figures adapted from Ding et al. (2011). (a) Schematic of the experimental set-up of Ding et al. (2011).(b) Lift force F_z measured by Ding et al. (2011) as a function of depth for three different cross sections of the cylinder (circular, square and half circular)	9
I.6	Scheme of the asymmetric force distribution around a cylindric intruder (adapted from Guillard et al. (2014))	10
I.7	Set-up of the numerical experiment from Guillard et al. (2016). A disk is fixed to a virtual spring that counterbalances gravity and the segregation force (adapted from Guillard et al. (2016)).	11
I.8	Set-up of the numerical experiment from Tripathi and Khakhar (2013). A heavy particle is falling by gravity through the lighter bath of particles. (adapted from Tripathi and Khakhar (2013))	12
I.9	Scheme summarising the upscaling process from the understanding of the segregation forces at the granular scale (\mathbb{O}) to the modeling at a large scale of the impact of size segregation on geomorphology. The red box represents the different scales addressed in this PhD thesis.	14

TABLE DES FIGURES

II.1 Forces acting on a large intruder. Π_f (—) is the buoyancy due to the fluid, Π_p (—) is the granular buoyancy and f_l (—) is the lift force identified by Guillard et al. (2014, 2016). The particle is also submitted to the drag forces $f_d^p = f_{dx}^p + f_{dz}^p$ (—) and $f_d^f = f_{dx}^f + f_{dz}^f$ (—) respectively due to the interaction with small particles (Tripathi and Khakhar, 2013) and the fluid.	19
II.2 Empirical segregation function $\mathcal{F}(\mu)$ of the segregation force $f_{seg} = V_l \mathcal{F}(\mu) \partial p^s / \partial z$ found by Guillard et al. (2016) as a function of the local friction coefficient μ . + are the simulation results found by Guillard et al. (2016) using DEM. — is the function they proposed and — is $\mathcal{F}(\mu) = 1/\Phi + (1 - e^{-70(\mu - \mu_c)})$, the improved function proposed.	22
II.3 The whole domain is meshed in N cells of size Δz for each timestep n . The scalar values such as the volume fractions Φ^k and the pressures p^k are defined at the center of the cells. The velocity vectors w^k are defined at the faces of the cells. The yellow surface represents the j^{th} control volume on which the scalar values are integrated. The blue surface represents the j^{th} control volume on which the velocity fluxes are integrated.	32
III.1 Dimensionless profiles and configuration from the DEM simulations. (a) Streamwise mixture velocity profile in the bed (—) and mixture volume fraction (—). The inset is the semilog plot of the velocity profile. (b) Solid shear rate (—) and the corresponding fit $\dot{\gamma}^m = \gamma_0 e^{z/s_0}$ (---) with $\gamma_0 = 1.64 \times 10^{-7}$ and $s_0 = 0.74$. (c) Solid shear stress and the corresponding fit $\tau_{xz}^m = a_0 z + \tau_0$ (---) with $a_0 = -0.078$ and $\tau_0 = 0.91$. The top and lower boundary of the quasi-static bed are represented by -----. (d) Sketch of the numerical experiment with the input profiles for the rheology. (e) Concentration profile of small particles at the initial state for the DEM (----) and its Gaussian fit (—), taken as an input for the multi-phase flow model. The concentration profile, ϕ , of the mixture (—) is also represented.	39
III.2 Spatio-temporal plot of the small particle concentration in the bed obtained with (a) the multi phase model, (b) the DEM simulation.	41
III.3 Results of the simulation for the multi-phase flow model (---), the advection-diffusion model of (II.71) (—) and the DEM (----). (a) Temporal evolution of the center of mass. (b) Concentration profiles of small particles at the end of the simulation ($t \simeq 60000$). ■ represents the maximum concentration of the profiles.	42
III.4 Comparison with the DEM (----) for various values of $\mathcal{F}_l = cste$ for the temporal evolution of (a) the center of mass and (b) the maximum concentration of ϕ^s	44
III.5 (a) Advection coefficient in the bed (equation II.71) with $\mathcal{F}_l = 1$, for $N_s = 1.5$ (—) and $S_{r0} I^{0.85}$ proposed by Chassagne et al. (2020b) (----). (b) Diffusion coefficient in the bed from equation (II.71) for $\phi^s = \max(\phi^s)$ for the case $N_s = 1.5$ (—) and $D_0 I^{0.85}$ proposed by Chassagne et al. (2020b) (----).	47

TABLE DES FIGURES

III.6 $I^{0.85}$ computed from DEM results (—) and its exponential fit $I'_0 e^{-z/s_2}$ (----) compared with $\sqrt{p^m} I / \mu$ (—) and its exponential fit $D'_0 e^{-z/s_3}$ (---). $I'_0 = 7.52 \times 10^{-7}$, $s_2 = 0.8$, $D'_0 = 8.46 \times 10^{-7}$ and $s_3 = 0.78$	48
III.7 Upper part of the panel: temporal evolution of the center of mass for $N_s = 0.5, 1, 1.5, 2$. Lower part of the panel: final small particle concentration profile for $N_s = 0.5, 1, 1.5, 2$. ---- are the DEM results from Chassagne et al. (2020b). The concentration profile obtained without any parametrisation, in the case $N_s = 1.5$ (from figure III.3b), has also been plotted (.....).	50
III.8 Upper part of the panel: temporal evolution of the center of mass for $N_s = 1$ and $r = 1.25, 1.5, 1.75, 2, 2.25$. Lower part of the panel: final small particle concentration profile for $N_s = 1$ and $r = 1.25, 1.5, 1.75, 2, 2.25$. In these figures, — corresponds to the advection-diffusion model and ---- are the DEM results from Chassagne et al. (2020b).	52
IV.1 a) Experimental set-up. b) Picture of the set-up at INRAE Grenoble laboratory . \oplus is the bead feeder, \otimes is the flow meter, \mathfrak{O} is the LED backlight. c) Granular bed with the intruder in the flume, \oplus is the camera used for recording. d) \mathbb{O} is the Region Of Interest (ROI).	56
IV.2 Initial position of the large particle in the granular bed. The surface of the granular bed is at a position h_b and the depth of the center of the intruder is z_I . The scheme on the left represents the case where the intruder is sufficiently large to avoid being hidden. On the right scheme, $W - d_l > d_s$ so the particle has to be plunged against the wall to avoid a small particle to slide ahead of it.	58
IV.3 Diagram showing the manner of placing the intruder in the bed depending on the number of particles in the width of the flume (W/d_s) and the size ratio investigated. The green area represents the configuration where it is possible to find a manner of placing the intruder. Above the line $W/d_s = r + 1$, the intruder has to be placed against the sidewall. Below this line, the intruder can be tracked without a bed particle hiding it. The blue dotted lines represents the value of W/d_s for both Shields numbers investigated and the size ratio that can be investigated.	59
IV.4 Image of the Region Of Interest (ROI). The black particle is the large intruder of diameter d_l . The horizontal blue line is the average free surface line and the green horizontal line is the average bedline. Red crosses correspond to the average velocity profile measured with the <i>opyflow</i> toolbox. The black dashed line is the linear fit.	63

TABLE DES FIGURES

IV.5 Vertical position of the center of the intruder with time for the different size ratios. (a) is the case $\tau^* = 0.13$, (b) is the case $\tau^* = 0.25$ and (c) is the comparison between $W/d_s = 3$ (left column) and $W/d_s = 7.5$ (right column) for a size ratio $r = 2.5$ with $\tau^* = 0.13$. The green envelope only given for clarity on each first configuration, corresponds to the potential error on the detection of the particle center. The red horizontal envelope for each size ratio represents the transition between the quasi-static regime and the liquid flow regime. The upper boundary corresponds to $I = 0.01$ while the lower limit is $I = 0.001$. In (a), for the size ratio $r = 1.2$, the averaged streamwise velocity profile of the particle bed is represented in the inset.	66
IV.6 Vertical displacement of the center of the intruder as a function of the streamwise displacement. The dashed line (----) corresponds to the averaged slope on all repetitions. (a) $\tau^* = 0.13$, (b) $\tau^* = 0.25$ and (c) compares the case $W/d_s = 3$ and $W/d_s = 7.5$ for $\tau^* = 0.13$. x_0 and z_0 are for the initial position.	68
IV.7 Semi-log plot of the intruder center elevation as a function of time, rescaled by the final time t_{end} , $z(t) - z(t_{end})$. The 0 value on the horizontal axis represents the last time. (a) $\tau^* = 0.13$. (b) $\tau^* = 0.25$. Colors correspond to the same repetitions as in figure IV.5.	70
IV.8 Average segregation final time t_{end} as a function of the size ratio. Blue circles for $\tau^* = 0.13$, red squares for $\tau^* = 0.25$. Errorbars give maximum and minimum segregation final times.	72
IV.9 Mean slope measured on the trajectories $z(x)$ for each size ratio. Blue circles for $\tau^* = 0.13$, red squares for $\tau^* = 0.25$. Errorbars give maximum and minimum slope values.	73
IV.10 Gathering of all the linear trajectories obtained experimentally. The black dotted line is the averaged slope measured. The standard deviation on the average slope is $\sigma(\tan \alpha) = 9.7 \times 10^{-2}$	74
IV.11(a) Initial layout before the observed mechanism occurs, for two repetitions with size ratio $r = 2.5$. (b) Mean images over a period $t \sim 70s$, with 1 image/s, after the initial layout presented in figure (a). (c) Mean images until the end of the experiments.	75
IV.12 Local vertical force measurement by Ding et al. (2011) for a circular intruder. Black arrows represent the front of the intruder. Green area represent the angle at which the constraint is measured.	77
IV.13 Trajectory $z(x)$ of the intruder predicted by our model with the closures of Guillard et al. (2016) and Tripathi and Khakhar (2013) (+) and the results with the new closures proposed in section III.4.2 (----). The average trajectory measured in our experiments is the black dashed line (----).	80
IV.14 Position of the center of the intruder with time $z(t)$ for the experiments (—), the model with the closures of Guillard et al. (2016) and Tripathi and Khakhar (2013) (+) and the results with the new closures proposed in section III.4.2 (----)	80

 TABLE DES FIGURES

IV.15	Trajectory of the intruder obtained with equations (IV.10) and (IV.11) (----). The average trajectory measured in our experiments is the black dashed line (---)	82
V.1	Vertical position of the center of the intruders with time obtained with DEM simulations. Size ratio $r = 2$ and Shields number $Sh = 0.2$	90
V.2	Trajectory of the intruders obtained with DEM simulations. Size ratio $r = 2$ and Shields number $Sh = 0.2$. x_0 and z_0 are initial positions and the black dashed line (---) is the mean slope.	90
A.1	The whole domain is meshed in N cells of size Δz for each timestep n . The scalar values such as the volume fractions Φ^k and the pressures p^k are defined at the center of the cells. The velocity vectors w^k are defined at the faces of the cells. The yellow surface represents the j^{th} control volume on which the scalar values are integrated. The blue surface represents the j^{th} control volume on which the velocity fluxes are integrated.	94
B.1	Good features to track (in red) detected on an image. One can see that the good features generally correspond to the edge of the particles.	102
B.2	(a): Streamwise velocity profile of the granular bed measured with the PTV algorithm (o) and the <i>OpyFlow</i> toolbox (+) for the experiments of Frey et al. (2020). (b): Linear fits performed on both velocity profiles (white dashed lines). (c): Error, in percent, of the velocity measured with the <i>OpyFlow</i> toolbox u^{opyf} compared with the velocity measured with the PTV u^{ref}	105
B.3	(a): Streamwise velocity profile of the granular bed measured with the PTV algorithm (o) and the <i>OpyFlow</i> toolbox (+) for the experiments of Dudill et al. (2018). (b): Linear fits performed on both velocity profiles (white dashed lines). (c): Error, in percent, of the velocity measured with the <i>OpyFlow</i> toolbox u^{opyf} compared with the velocity measured with the PTV u^{ref}	106
D.1	Image of the granular bed in the flume. The green area corresponds to the volume of particles that has been removed for the measuring of the volume fraction.	109

TABLE DES FIGURES

LISTE DES TABLEAUX

IV.1 Summary of the configurations explored with their associated parameters. A configuration is defined by Sh (1 for the lowest Shiels number or 2 for the highest Shields number), W(1 for $W/d_s \sim 3$ and 2 for $W/d_s = 7.5$) and the size ratio r. d_s and d_l are respectively the sizes of the particle in the bed and of the intruder. Q_s is the sediment rate and Q_w is the water flow rate. The last column gives the number of repetitions for each configuration.	61
IV.2 Dimensionless numbers for the configurations. h_w is the mean depth on the configurations and repetitions.	61
IV.3 Uncertainties Δ for the parameters linked to the granular material and standard deviation σ associated to the water depth and the Shields number.	62

LISTE DES TABLEAUX

CHAPITRE I

INTRODUCTION

I.1 Context

Rivers transport sediments from the watershed upstream or from the alluvial bed itself. The slope and the water discharge strongly affect the sediment load. In mountain streams, slopes are steeper and the flow rate can rise significantly during extreme events, leading to strong sediment transport with coarser sediments than in lowland rivers. During such events, the transported blocks can reach one meter and have major consequences on public safety and ecosystems. As an example, on 2nd October 2020, in the Mercantour massif (south east of France), an intense flood destroyed the Vésubie and the Roya valleys. Damages induced by erosion and sediment transport on public infrastructure were estimated to more than 200 million euros. The valleys were inaccessible for several days forcing authorities to provide supplies by helicopter. Furthermore, nine people died and the aquatic fauna was annihilated. Against such hazards, predictions on geomorphological evolution due to sediment transport is of major concern to protect people and the environment.



FIG. I.1: (a) Damages caused by erosion and sediment transport in the Vésubie valley (source: La Provence). (b) Aerial image of a village in the Vésubie valley before and after the flood (source: Le Télégramme).

Sediment transport is generally divided into two modes of transport. First, on the entire depth of the river, small particles can be put into suspension by the turbulent

eddies. Secondly, near the river bed, bedload is the transport of coarser sediments in close contact with the mobile river bed by sliding, rolling or saltating. For mountain rivers, bedload transport is far from negligible since it represents 30% to 50% of the total sediment load ([Turowski et al., 2010](#)). Yet, in spite of one century of modern research, predicting bedload transport rate within one order of magnitude is still difficult ([Recking et al., 2012](#)).

Classical models for bedload are based on two principles:

- Bedload occurs above a critical threshold of motion for the particles. To define this threshold, [Shields \(1936\)](#) proposed to make the bottom shear stress applied by the fluid τ_b^f (i.e. the force that has a tendency to drag the particles) dimensionless by the buoyancy weight of the characteristic particles at the bed surface (i.e. the resistive force):

$$\tau^* = \frac{\tau_b^f}{(\rho^p - \rho^f) gd}, \quad (\text{I.1})$$

where ρ^p is the particle density, ρ^f the fluid density, g is the gravity acceleration and d is the diameter of the characteristic bed particles. The motion threshold is found for a critical value of τ^* noted τ_c^* and characterized by a variability both in its definition and in its available measurements. As an example, $\tau_c^* = 0.047$ in the well known value for the formula of [Meyer-Peter and Müller \(1948\)](#).

- The bedload transport rate per unit width, Q_s , is a nonlinear function of the bottom shear stress. This transport rate is usually presented without dimension using the Einstein parameter ([Einstein, 1942](#)):

$$Q_s^* = \frac{Q_s}{\sqrt{(\rho^p/\rho^f - 1) gd^3}}. \quad (\text{I.2})$$

In the last century, much research was done to determine the influence of the bottom shear stress on the sediment discharge. For gravel bed rivers, it is classically admitted that the sediment discharge is linked to the dimensionless excess bottom shear stress $\tau^* - \tau_c^*$ as ([Meyer-Peter and Müller, 1948](#); [Wong and Parker, 2006](#))

$$Q_s^* = A (\tau^* - \tau_c^*)^{3/2}, \quad (\text{I.3})$$

where A varies between the configurations but was proposed, for example, to be equal to 8 by [Meyer-Peter and Müller \(1948\)](#) or 3.97 by [Wong and Parker \(2006\)](#). The dependency on the dimensionless bed shear stress to the power 3/2 is generally confirmed in flume experiments, where conditions are well-controlled. However, it has been revealed to poorly fit field data ([Gomez, 1991](#); [Recking et al., 2012](#)). Other works such as [Lajeunesse et al. \(2010\)](#) and [Recking \(2010\)](#) have proposed improved formulations still based on the dimensionless excess bottom shear stress. Yet, the concept of constant threshold for incipient motion is debatable. In turbulent flows, velocity fluctuations can overcome the resisting forces and drag the particles away while the average bottom shear stress remains lower than the resistive forces. Hysteresis effects can also play a role in the motion of the particles: the stress at which a particle is eroded can be different from the one at which it is deposited ([Graf and Pazis, 1977](#)).



FIG. I.2: Polydispersity in a mountain stream (Vénéon river, La Bérarde, French Alps). In green the sand, in red the medium cobbles and in blue the large boulders.

These examples highlight the necessity to consider the physical processes at the scale of the granular bed in order to improve the theoretical bedload transport equations. In this context, [Ancey \(2020\)](#) identified two main challenges:

- Understand how near bed turbulence affects bedload transport.
- Understand the mechanisms linked to the effects of particle size variability.

The present dissertation focuses on the second point. As figure I.2 shows, mountain streams can contain a large size distribution, from less than a millimeter, for sands, to a meter for large blocks, that can affect transport. Particularly, size variability (also called polydispersity) was shown to increase the transport rate in the field ([Ferguson et al., 1989](#); [Montgomery et al., 1999](#)) but also in laboratory experiments ([Gilbert and Murphy, 1914](#); [Iseya and Ikeda, 1987](#); [Ikeda and Iseya, 1988](#); [Cui et al., 2003](#); [Venditti et al., 2010](#); [Dudill et al., 2018](#); [Hill et al., 2017](#)). In addition, with a bimodal distribution of bed particles (two size of particles), [Houssais and Lajeunesse \(2012\)](#) observed that the critical threshold of motion was reduced for both sizes of grains.

Polydispersity can be taken into account in transport models by replacing the dependency on the median diameter d_{50} by d_{84} , corresponding to 84% of the particles below this diameter, as proposed by [Recking \(2013\)](#). More complex models propose to consider each class of particles separately using hiding functions. These functions adapt the critical Shields number to each particle size in order to model the effect of size repartition on bedload transport ([Egiazaroff, 1965](#); [Proffitt and Sutherland, 1983](#); [Wilcock and Crowe, 2003](#); [Houssais and Lajeunesse, 2012](#)).

However those approaches remain largely empirical and ignore the complexity of particle-particle interactions. For [Frey and Church \(2009\)](#) and [Frey and Church \(2011\)](#), with significant advances in the science of granular media, considering bedload transport from a granular perspective could be a decisive turning point for the comprehension and the modeling of effects linked to polydispersity. We identified two studies that adopted this point of view. Viewing the bed in motion as a granular flow, [Chassagne et al. \(2020a\)](#) investigated a bimodal armoured bed, i.e. small particles protected from erosion by the

coarse particles located above, using discrete simulations. The authors found that the small particles were dragged more easily and played the role of a conveyor belt for the large grains, demonstrating the granular origin of the increased mobility. [Ferdowsi et al. \(2017\)](#) performed laboratory and numerical experiments on a bimodal bed in laminar bedload transport and attributed the armouring process to a granular phenomenon called grain-size segregation. They showed that a better knowledge of segregation is of major importance for the accurate prediction of size repartition in the bed.

Granular segregation is the tendency for particles having different properties, shapes, densities or sizes to separate spatially, creating different patterns in the river beds ([Bridgwater, 1976](#); [Knight et al., 1993](#); [Thomas, 2000](#); [Zhu et al., 2020](#)). For size ratios (ratio between the diameters of the coarse and the fine particles) above six, spontaneous percolation occurs: fine particles percolate spontaneously into the gaps between the largest particles under the effect of gravity, without any motion of the granular mixture. Such a phenomenon was observed in bedload transport by [Beschta and Jackson \(1979\)](#); [Gibson et al. \(2010\)](#) and [Dudill et al. \(2017\)](#). Shear and gravity driven size segregation is more surprising: under the action of gravity or shear rate, the large particles are driven toward the region of higher shear stress and the small particles migrate toward the region with lower shear stress ([Guillard et al., 2016](#)). In bedload transport, vertical size segregation generally implies the ascent, against gravity, of the largest particles toward the top of the river bed while the smallest particles infiltrate downward. In order to improve the understanding and the modeling of size segregation in bedload transport, this PhD work focuses on vertical gravity driven size segregation in bedload transport using the granular physics framework. This approach is possible thanks to a long process in the study of granular physics and particularly of size segregation in granular media. In the next section, we review the main advances on the subject.

I.2 Size segregation in granular media

Granular media is generally defined as an ensemble of solid macroscopic particles with sizes larger than $100\mu\text{m}$. Sand, coal, lentil, sugar, gravels or avalanches are some of the numerous examples of granular media, which are present everywhere around us. Everyone has already experienced the strange behaviour of granular media: one can walk on a sand pile while it can flow as a fluid, showing that granular matter can behave either as a solid or as a fluid. When shaking grains in a box, they interact through binary collisions and behave like a gas. Modeling these different states has motivated numerous studies over the last decades and significant progress has been made on this topic ([Jenkins and Richman, 1985](#); [Ancey et al., 1999](#); [GDR MiDi, 2004](#); [Jop et al., 2006](#); [Forterre and Pouliquen, 2008](#); [Kamrin and Koval, 2012](#); [Andreotti et al., 2013](#); [Jop, 2015](#); [Berzi et al., 2020](#)).

Among the new challenges presented by the granular medium, size segregation is certainly one of the most important. As mentioned in the previous section, it is largely responsible for river geomorphology but is also a key issue in industrial processes. Indeed, in pharmaceutical processes or in concrete preparation, where processes rely on granular media manipulation, size segregation can lead to heterogeneous mixtures that can completely change the property of the medicine or the material. As a consequence, granular physicists performed numerous studies to better understand and predict this

phenomenon.

Shear and gravity driven size segregation have been studied experimentally and numerically in many granular flow configurations. Plane shear cells provide a uniform shear and a linear velocity profile, which induces a constant shear rate and shear stress, providing the simplest configuration to study the segregation process. Such a configuration has been investigated by [Golick and Daniels \(2009\)](#), [Guillard et al. \(2016\)](#), [Fry et al. \(2018\)](#) and [Jing et al. \(2020\)](#). More complex cases have been investigated such as dry granular avalanches ([Savage and Lun, 1988](#); [Dolgunin and Ukolov, 1995](#); [Wiederseiner et al., 2011](#); [Jones et al., 2018](#); [Thornton et al., 2006](#); [Guillard et al., 2016](#)) or annular rotating drums ([Thomas, 2000](#); [Gray and Ancey, 2011](#)). Investigations have been conducted at different scales. Investigating the macroscopic behaviour yields macroscopic models that can reproduce the phenomenon at the scale of the granular flow. Investigating the forces at the particle scale provides an accurate description of the phenomenon with a deep comprehension of the mechanisms.

I.2.1 Macroscopic description

[Savage and Lun \(1988\)](#) is one of the first milestone in the understanding of size segregation. Investigating experimental bidisperse flow down inclined planes, they predicted from dimensional analysis that the velocity shear rate $\dot{\gamma}^p$ should be the controlling parameter for size segregation. Indeed, when a granular medium is sheared, a layer of particles moves faster than the one beneath, allowing particles to find gaps in which to fall by gravity. The authors named this phenomenon “kinetic sieving” and contrasted it to the squeeze expulsion mechanism, which is supposed to counterbalance the downward motion. In more recent works, [Golick and Daniels \(2009\)](#) in shear cell experiments, and [Fry et al. \(2018\)](#) in shear cell Discrete Element Model (DEM) simulations, evidenced the effect of granular pressure, observing less efficient segregation when increasing the pressure. [Gray \(2018\)](#) gathered the shear rate and the pressure dependencies by suggesting that size segregation should depend on the inertial number I . Indeed, the dimensional analysis shows that, for granular media, the system is controlled by a single dimensionless number called inertial number I ([GDR MiDi, 2004](#); [Da Cruz et al., 2005](#))

$$I = \frac{d\dot{\gamma}^p}{\sqrt{P^p/\rho^p}}, \quad (\text{I.4})$$

where d is the particle diameter, P^p is the granular pressure, and ρ^p is the particle density. This number can be interpreted as a ratio between a microscopic timescale $t_{micro} = d/\sqrt{P^p/\rho_p}$ and a macroscopic timescale $t_{macro} = 1/\dot{\gamma}^p$. The first is the time taken by the particle to fall in a hole under the effect of the pressure P^p while the other is the time taken by a grain to move one diameter in the streamwise direction of the flow. The value of the inertial number is representative of the deformation of the granular system (see figure I.3) and thus should influence kinetic sieving. DEM simulations of dry granular flows ([Fry et al., 2018](#)) confirmed that the segregation velocity scales with the inertial number to a power about 0.85.

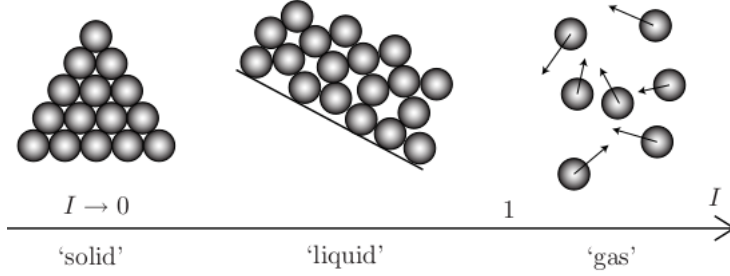


FIG. I.3: Flow regime as a function of the inertial number I (from Andreotti et al. (2013))

In the kinetic sieving regime, the downward motion of the small particles is allowed by the deformation of the granular matrix. Intuitively, for a bidisperse mixture, the larger the size ratio, the easier the small particles can seep down in the holes created by the deformation of the large particle matrix. A number of studies found that the percolation depends on the particle size ratio but the result is less intuitive. Golick and Daniels (2009), Guillard et al. (2016) and Jing et al. (2020) found that the upward segregation of particles experience a maximum efficiency for a size ratio of two, for dynamical granular regimes ($10^{-3} < I < 1$). Thomas (2000) observed in rotating drums experiments that above a size ratio $r = 5$, the large particles were mixing again with the small particles suggesting a mass effect.

Similarly to the hindrance function for the fluid drag force on a particle, size segregation has also been observed to depend on the concentration of large particles. Indeed, studies indicate that the efficiency of the segregation process is linked to the concentration in small (or large) particles in the granular sample (Fan et al., 2014a; Van der Vaart et al., 2015; Jones et al., 2018).

1.2.2 Continuum modeling

In order to model size segregation on a large amount of particles, the continuum framework is classically used by viewing segregation as an advection-diffusion phenomenon. From the different dependencies identified previously, numerous contributions empirically set the advective velocity w^s and the diffusion coefficient D of an advection-diffusion equation for the vertical macroscopic behaviour of the small particles (Dolgunin et al., 1998; Thornton et al., 2006; Gray and Chugunov, 2006; Hill and Tan, 2014; Van der Vaart et al., 2015; Ferdowsi et al., 2017; Gray, 2018; Fry et al., 2019; Cai et al., 2019; Umbanhowar et al., 2019):

$$\frac{\partial \phi^s}{\partial t} - \frac{\partial}{\partial z} (\phi^s w_s) = \frac{\partial}{\partial z} \left(D \frac{\partial \phi^s}{\partial z} \right), \quad (\text{I.5})$$

where t denotes time, z the vertical axis, while ϕ^s and ϕ^l are the small and large particle relative concentration (with $\phi^s + \phi^l = 1$). According to Dolgunin and Ukolov (1995) and Gray and Thornton (2005), the advective velocity should have a dependency on the local concentration taken as proportional to the large particle concentration, $w_s = \phi^l S_r$. S_r is the advection coefficient of small particles into large particles. This coefficient is

usually taken as an empirical constant for a given application or determined from semi-empirical analysis. The diffusion coefficient D models the diffusive remixing of small particles into large particles. It has also received attention in the literature (Bridgwater et al., 1985; Fan et al., 2015; Fry et al., 2019) and it has been suggested that it should depend on the volume fraction (Cai et al., 2019) and on the shear rate (Fry et al., 2019; Cai et al., 2019).

The advection-diffusion equation disregards the discrete contacts between particles and makes it possible to model the effect of size segregation at large scales. However, the empirical advection and diffusion coefficients are obtained for specific configurations, making these coefficients hard to generalise to all configurations. A powerful alternative consists in developing multi-phase flow models. Such a framework considers the different sizes of particles as distinct continuous phases that interact with each other. Each phase is modeled based on mass and momentum equations so as to consider the physical interaction forces between the phases. Such an approach was proposed for kinetic sieving by Thornton et al. (2006) and Gray and Chugunov (2006). They developed a three-phase flow model for gravity driven granular flows made of a bi-disperse combination of large and small particles with an interstitial passive fluid. The interaction forces were proposed in the framework of the mixture theory (Morland, 1992), which assumes that each physical variable is a partial value of the intrinsic variable of the whole mixture (the mixture is made of all the different phases and considered as an effective medium). Among the interaction forces, an interaction drag force as well as a segregation force were proposed. The idea behind the segregation force was that the small particles carry less of the overburden granular pressure than the large particles, leading to segregation. This effect was modeled by a weighted function in the pressure of the granular phase:

$$P^\mu = f^\mu P^m, \quad (\text{I.6})$$

where P^m is the overburden pressure and P^μ is the pressure for phase μ with $\mu = l$ for large particles and $\mu = s$ for small particles. f^μ was proposed as (Thornton et al., 2006):

$$\begin{cases} f^l = \phi^l + B\phi^l(1 - \phi^l) \\ f^s = \phi^s - B\phi^s(1 - \phi^s), \end{cases} \quad (\text{I.7})$$

where B quantifies the amount of overburden pressure that is carried by a phase. With this three-phase flow model, the authors were able to analytically derive the advection-diffusion model (equation I.5). This derivation represented an important step in the understanding of the physical processes at work in size segregation since the advection and diffusion coefficients were linked to the particle-scale interaction parameters.

However, the interaction forces between large and small particles were postulated without support from independent physical evidence and require coefficients to be calibrated for each configuration. The understanding of the mechanisms at the particle scale could therefore bring more robust closures as well as more general formulation.

More generally, while existing continuum models provide satisfying results when the concentrations of the phases are relatively similar, they fail when predicting results for low concentration. According to Tunuguntla, D. R. and Thornton, A. R. (2017), this is because the continuum approach is valid as long as the particle phase can be considered as a continuum (i.e. the concentration must not be too low) but also because the

segregation mechanisms at the particle scale are still poorly understood. Therefore, it is necessary to understand the segregation mechanism at the particle scale.

I.2.3 Description at the particle scale

To the best of our knowledge, the investigation of the size segregation process at the particle scale has been first investigated in vibrated systems (Rosato et al., 1987; Jullien et al., 1992; Duran et al., 1993). Observations showed that when shaken with an acceleration higher than the acceleration of gravity g , particles encounter small flight in which the small particles can seep in the hole created below the large particle, pushing the latter upward. Duran et al. (1993) performed 2D experiments with a large disk placed into small disks in a vibrated system just above the threshold of excitation, i.e. in the quasi-static limit. One result of their experiment is presented in figure I.4a. They showed that below a critical size ratio, the large intruder segregates with irregular ascents separated by horizontal displacements (bottom image of figure I.4a). However, above a critical size ratio, the intruder rises linearly and continuously toward the surface (upper image of figure I.4a). Their work highlighted the fundamental role of the vault on the continuous ascent. Indeed, using figure I.4b they showed that when small particles are located below the center of the intruder, they can support the intruder by an arching effect and the intruder has no more contact with the underlying layer, creating a hole below it. By falling into this hole, the supporting small particles push the intruder upward. The authors also found that this structure generally formed a triangle with an opening angle of 60° (see figure I.4c, corresponding to the 2D angle of repose for granular media). Using a geometrical model, they proposed a model for the ascent of the intruder with time. The model suggested that above a critical size ratio, the intruder constantly rises in this arching configuration, leading to a continuous ascent. In 3D, the critical size ratio was found to be $r_c = 2.78$. Jullien et al. (1992) proposed a 3D model for particle size segregation in a vibrated system. For a similar threshold value $r = 2.8$, they reported a radical change of behaviour for the intruder. While below this limit the intruder has a maximum upward displacement, the vertical displacement of the intruder becomes monotonous above $r_c = 2.8$.

Nevertheless, it should be noted that in these studies the segregation mechanism is also called Brazil nut effect and is supposed to be different from shear or gravity driven granular flows as the deformation of the medium is driven by agitation.

The analysis of intruders in shear or gravity-driven granular flows have been performed more recently. Particularly, thanks to the advances on the Discrete Element Method (DEM), in which normal and tangential contact forces are solved, studies have tried to measure the force distribution around an intruder in a granular media. Ding et al. (2011) experimentally and numerically studied the forces exerted on different sorts of long intruder with different cross sections pulled into a granular bed made of beads (see figure I.5). They measured the drag force (longitudinal component of the resulting force on the intruder) and the lift force (vertical component of the resulting force on the intruder) on the cylinder. The lift force they measured with depth is presented in figure I.5b. Only the circular and the square cross section, which are symmetrical cross sections, generate an upward lift force. Ding et al. (2011) showed that contrary to

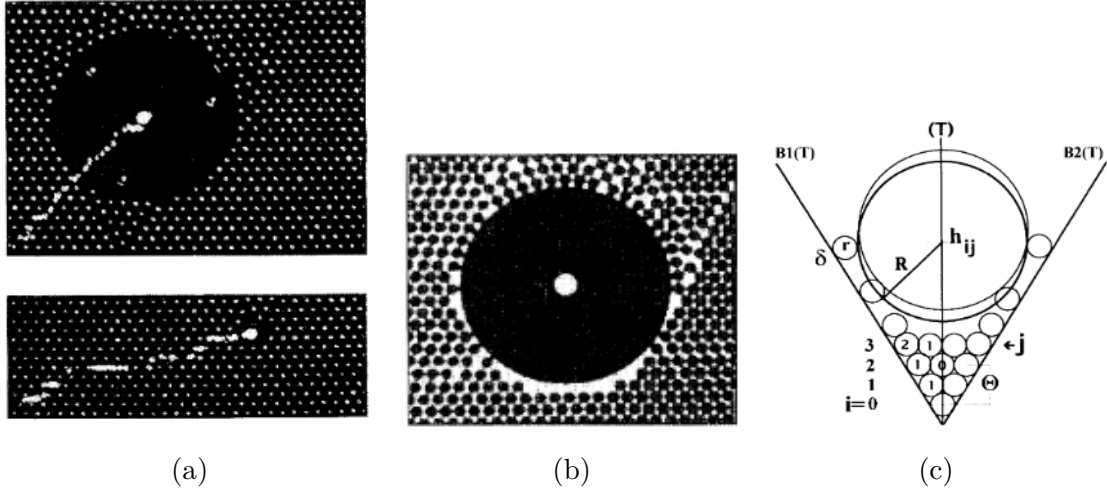


FIG. I.4: Figures adapted from Duran et al. (1993). (a) Experimental observation for large steel disks of size ratio $r = 16$ (top picture) and $r = 2$ (bottom picture). (b) Photography of the 2D experiments showing the arching effect: the intruder is supported by the small particle arrangement on its right side. (c) Schematic diagram describing the vault effect (also called arching).

Newtonian and non-Newtonian fluids, no asymmetry in the shape of the intruder was necessary to observe a lift force. They were able to measure the local forces on the differential elements of the intruder using a plate at the same depth with an angle having the same angle of attack as the differential element of the intruder (the angle varies between 0° and 180° , with 0° corresponding to the bottom of the intruder). A strong asymmetry of force was found between the upper and the lower part of the intruder suggesting that unlike fluids, the granular flow was responsible for the force asymmetry. The local vertical force was found to be maximum for an angle of 15° and a peak for the normal stress was found at an angle of 50° . Guillard et al. (2014), performed a similar

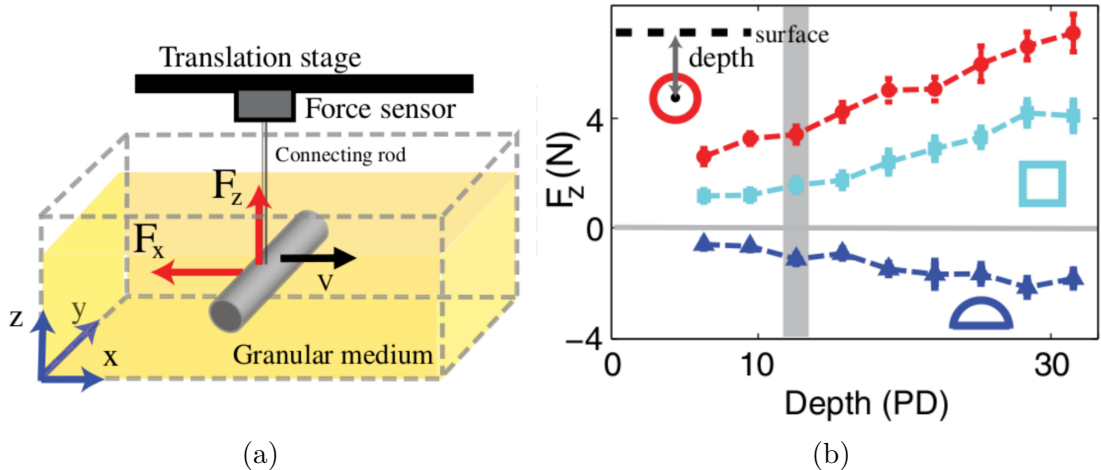


FIG. I.5: Figures adapted from Ding et al. (2011). (a) Schematic of the experimental set-up of Ding et al. (2011). (b) Lift force F_z measured by Ding et al. (2011) as a function of depth for three different cross sections of the cylinder (circular, square and half circular)

experiment as the one presented in figure I.5a by burying an intruder cylinder deep in a granular bed made of glass beads. The stress asymmetry around the intruder was recovered with a maximum normal stress at the bottom front of the intruder. It was found that the stress distribution around the intruder could be decomposed into a symmetric part proportional to the depth and an asymmetric part resulting from more complex dependencies. The authors explained: “The drag force would be the result of the depth dependency while the asymmetric stress would be the result of a more complex granular phenomenon and could not be linked to a classical drag force”. Only the asymmetric part would be responsible for the lift force. Thus, the readers should note that the lift force in the sense of [Guillard et al. \(2014\)](#) is not the same as [Ding et al. \(2011\)](#), where the “lift force” stands for the total resultant of the vertical forces. Since in granular media the flow properties are driven by the frictional rheology, which is proportional to the pressure, flow properties necessarily vary with depth. Thus, [Guillard et al. \(2014\)](#) suggested that the granular pressure gradient could be the source of the asymmetry.

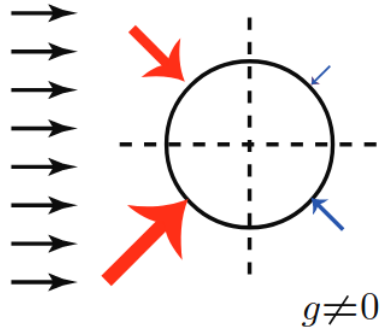


FIG. I.6: Scheme of the asymmetric force distribution around a cylindric intruder (adapted from [Guillard et al. \(2014\)](#))

In a second paper, [Guillard et al. \(2016\)](#) performed 2D DEM simulations of a large disk placed in a bed of small disks in the simple shear flow configuration. The authors attached the large particle to a virtual spring that counterbalanced the ascent of the intruder, as soon as there was an upward movement (see figure I.7). This system prevented a drag force to develop and the upward movement was directly proportional to the spring force, allowing the authors to measure only the force f_{seg} responsible for the segregation of the large particle. As proposed in [Guillard et al. \(2014\)](#), [Guillard et al. \(2016\)](#) tried to scale the vertical force by the pressure gradient. They found two contributions: one proportional to the pressure gradient $\partial P^p / \partial z$; the other proportional to the granular shear stress gradient $\partial |\tau^p| / \partial z$:

$$f_{seg} = V_l \left(\mathcal{F}(\mu, r) \frac{\partial P^p}{\partial z} + \mathcal{G}(\mu, r) \frac{\partial |\tau^p|}{\partial z} \right), \quad (\text{I.8})$$

where $V_l = \pi d_l^3 / 6$ is the volume of the intruder and \mathcal{F} and \mathcal{G} are empirical functions depending on the effective friction coefficient $\mu = |\tau^p| / p^p$ and on the size ratio $r = d_l / d_s$ between the intruder and the surrounding small particles. [Guillard et al. \(2016\)](#) studied

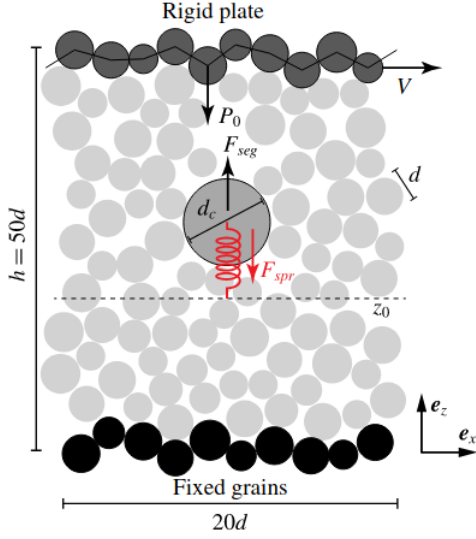


FIG. I.7: Set-up of the numerical experiment from [Guillard et al. \(2016\)](#). A disk is fixed to a virtual spring that counterbalances gravity and the segregation force (adapted from [Guillard et al. \(2016\)](#)).

the dependency on both parameters but only provided a dependency with μ as

$$\mathcal{F}(\mu) = 2.4 + 0.73 e^{-\frac{(\mu-\mu_c)}{0.051}}, \quad \text{and} \quad \mathcal{G}(\mu) = -\left(2 + 5.5 e^{-\frac{(\mu-\mu_c)}{0.076}}\right), \quad (\text{I.9})$$

where μ_c is the critical friction coefficient defining the threshold of movement. The segregation force proposed in equation (I.8) does not isolate the lift force resulting from the asymmetric stress. The authors measured both the granular buoyancy force that counterbalances the weight of the intruder and the granular lift force (responsible for the ascent of the intruder) arising from multiple inter-particle contacts with the intruder ([Guillard et al., 2014](#)).

Performing a similar experiment, [Jing et al. \(2020\)](#) proposed a size-ratio dependency for a force also based on the pressure gradient and showed that their formulation was able to model the remixing of the large particles observed by [Thomas \(2000\)](#).

[Van der Vaart et al. \(2018\)](#) used the same strategy as [Guillard et al. \(2016\)](#): a large intruder was fixed to a virtual spring in a granular flow of smaller particles and the upward force was measured. In an effort to isolate the lift force from the total segregation force, they proposed to subtract the granular buoyancy force from the total vertical force measured. The buoyancy force was based on the Voronoi volume and [Lantman et al. \(2021\)](#) showed that this formulation could be considered as accurate. [Van der Vaart et al. \(2018\)](#) found again that the lift force deviates from the hydrostatic pressure and observed that it was linked to the downward drag force. Based on this observation, they suggested that the lift force could be assimilated to a Saffman effect. The link with the force proposed by [Guillard et al. \(2016\)](#) was not determined but they mentioned that it could be done by expressing the velocity lag in term of pressure and shear stress gradients.

The work of [Van der Vaart et al. \(2018\)](#) shows the fundamental role of the drag force. To assess the drag force of a free moving particle in liquid granular flows, [Tripathi and](#)

[Khakhar \(2013\)](#) performed 3D DEM simulations of a settling heavy sphere in a bed of lighter spheres during a steady dry granular flow on an inclined plane (see figure I.8). This density segregation set-up generates a relative motion between the heavy sphere and the lighter ones, without generating segregation forces due to the size ratio. By

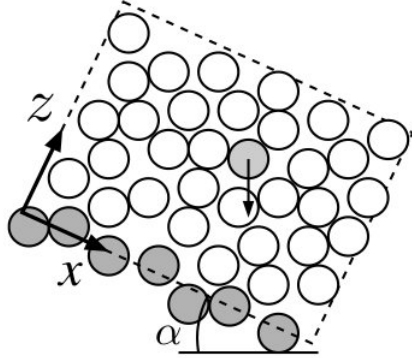


FIG. I.8: Set-up of the numerical experiment from [Tripathi and Khakhar \(2013\)](#). A heavy particle is falling by gravity through the lighter bath of particles. (adapted from [Tripathi and Khakhar \(2013\)](#))

analogy with classical hydrodynamics, light particles playing the role of an ambient fluid, the authors showed that the interaction force could be modeled with a Stokesian form of a solid drag force

$$f_d^p = c(\Phi)\pi\eta^p d_l v, \quad (\text{I.10})$$

where v is the settling velocity of the heavier particle, $c(\Phi)$ is a drag coefficient depending on the local solid volume fraction Φ , and $\eta^p = |\tau^p|/|\dot{\gamma}^p|$ is the viscosity of the granular medium considered as a non-Newtonian fluid. [Tripathi and Khakhar \(2013\)](#) suggested that $c(\Phi)$ depends on the local volume fraction Φ but still remains of the same order as the value observed for the Stokes law in a Newtonian fluid, i.e. $c \sim 3$.

This review of size segregation in granular media has shown that scientific advances were made using simple configurations, i.e. with simple shear cell where the shear rate is constant and only two sizes of particles without any fluid. Yet, some studies have also addressed size segregation in more complex configurations such as bedload transport. More generally, it is important to assess the generality of dependencies found in the simplest configurations.

I.2.4 Grain-size segregation in the framework of bedload transport

In bedload transport, the granular flow is forced by the fluid above and inside the porous bed thanks to gravity. It generates an exponential streamwise velocity profile ([Aussillous et al., 2013; Maurin et al., 2016](#)) where the region close to the top of the bed is highly sheared, creating a liquid granular flow regime (i.e. liquid regime from

figure I.3). However, deeper in the bed, the average streamwise velocity and hence the shear rate are very low and the particles move intermittently due to non-local rearrangements. This regime, close to the solid state is called creeping or quasi-static regime. The study of size segregation in this regime is challenging because the low shear rate induces low displacements that are difficult to analyse. For this reason there are only few experiments on size segregation in bedload transport.

[Ferdowsi et al. \(2017\)](#) investigated size segregation in a laminar configuration using an annular shear cell in which the sheared fluid generates bedload transport. They found that segregation occurs in both regimes but with different time-scales. In the liquid flow regime, large particles were segregating very fast compared with the quasi-static regime where large particles experienced caging effects before segregating. In addition, the authors showed that the equation for the vertical percolation of small particles (see equation I.5) could be used, suggesting that kinetic sieving is the driving mechanism.

[Chassagne et al. \(2020b\)](#) investigated kinetic sieving in turbulent bedload transport using a discrete element modeling approach. The configuration consisted in a bimodal bed, sheared by the turbulent water flow, in which a layer of small particles was initially deposited over the large particles. The downward segregation of the small particles in the liquid and the quasi-static regimes was investigated. The same inertial number dependency as [Fry et al. \(2018\)](#) was found for the segregation velocity. With the help of a travelling wave method, the authors evidenced that the small particles segregate downward as a layer and with a self-similar concentration profile because the ratio between the advection coefficient and the diffusion coefficient was always constant. As a result, the advection coefficient and the diffusion coefficient were found to have the same dependency on the inertial number. This analysis in terms of advection and diffusion highlighted once again that the advection-diffusion equation (I.5) is suitable to model grain-size segregation in bedload transport. Lastly, [Chassagne et al. \(2020b\)](#) found that, for small particles and for size ratios up to 3, the segregation velocity increases monotonically with the size ratio with no optimum in quasi-static regimes ($I < 10^{-3} - 10^{-2}$). Therefore the maximal segregation efficiency at $r = 2$ reported by [Golick and Daniels \(2009\)](#), [Guillard et al. \(2016\)](#) and [Jing et al. \(2020\)](#) was not recovered. In his PhD thesis, [Chassagne \(2020\)](#) proposed that contrary to the large particles that encounter a maximum efficiency ([Golick and Daniels, 2009; Guillard et al., 2016; Jing et al., 2020](#)), there is no reason for the small particles to have a maximum efficiency with the size ratio. Indeed, the smaller they are, the easier they can percolate into the holes of the granular matrix. Using shear box experiments [Van der Vaart et al. \(2015\)](#) found that a small particle segregates downward faster than a large particle rising upward. For [Chassagne \(2020\)](#), this asymmetry in the segregation velocity shows that the segregation process of a small particle percolating downward is not the same as that of a large particle segregating upward. While for small particles it is essentially controlled by gravity, the segregation of the large particle is also controlled by the friction.

I.3 Objectives and scope

Taking into account vertical size segregation into sediment transport models would provide better predictions of sediment rates as well as river geomorphological size patterns. Our literature review has evidenced several scales of comprehension for size segregation in shear driven flows. We address these different scales through upscaling, as illustrated by the conceptual scheme in figure I.9.

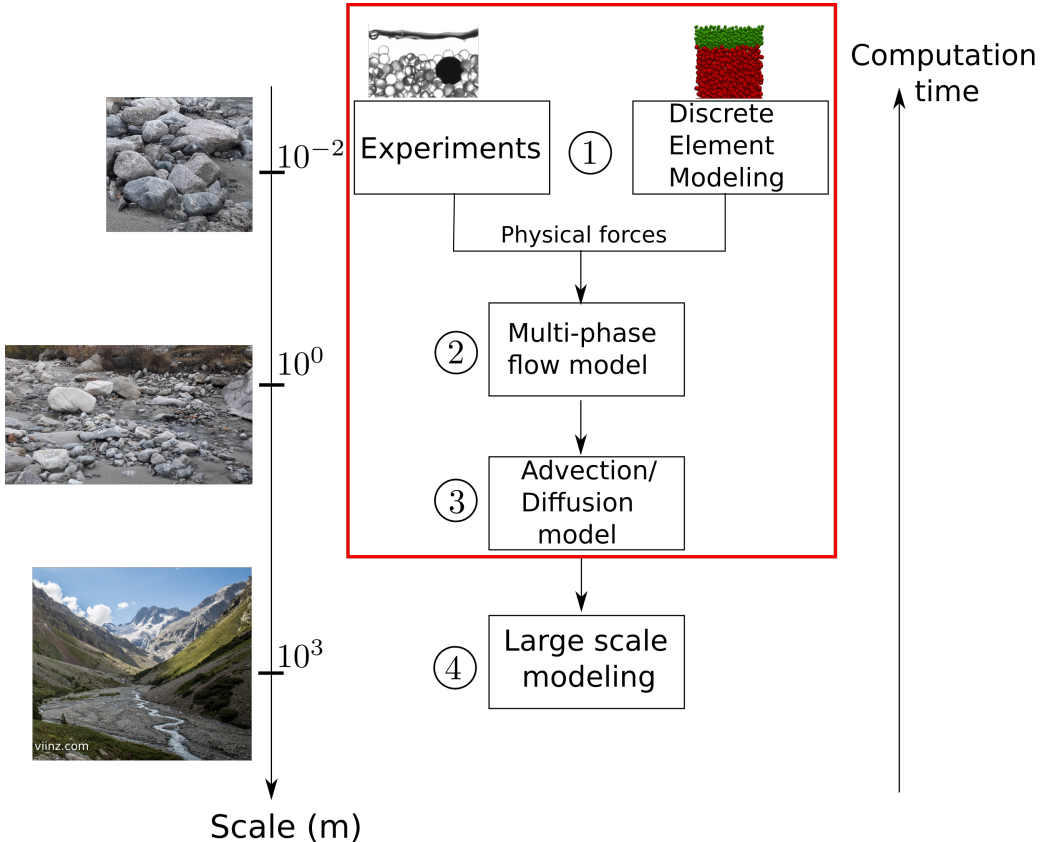


FIG. I.9: Scheme summarising the upscaling process from the understanding of the segregation forces at the granular scale (①) to the modeling at a large scale of the impact of size segregation on geomorphology. The red box represents the different scales addressed in this PhD thesis.

At the scale of the particles, corresponding to step ① in figure I.9, progress has been made thanks to recent simulations, providing formulations for the forces involved in the segregation process (Tripathi and Khakhar, 2013; Guillard et al., 2016). This PhD thesis proposes to bridge the gap between this particle scale forces and the vision of vertical size segregation as an advection-diffusion phenomenon (step ③ in figure I.9). Inspired by Thornton et al (2006), a multi-phase flow model (step ②) embedding the granular scale forces (step ①) is developed and provides a more general advection-diffusion model (step ③), which could be used in river-scale sediment transport models ($\sim 10^3$ m, ④). This last step would be the result of a long and challenging upscaling process.

The developed model relies on the particle scale segregation forces (step ①), which have never been studied experimentally in turbulent bedload transport. To refine the model

development and focus further on bedload transport applications, experiments have been carried out on the evolution of a single large intruder in a bedload configurations. This provides a new dataset for the comprehension and modelling of the squeeze expulsion mechanism, counter balancing the kinetic sieving, and allows assessing the validity of state of the art segregation forces (Tripathi and Khakhar, 2013; Guillard et al., 2016) in bedload transport.

I.4 Outline of the dissertation

This work comprises four chapters that are presented below. Chapters II and III have been published in *Journal of Fluid Mechanics* (<https://doi.org/10.1017/jfm.2021.218>).

- Chapter II presents the theoretical modeling for our upscaling process. Starting from the forces acting on a single large particle in bedload transport, we propose a new multi-phase flow model for a bidisperse configuration. Then, the numerical algorithm developed in this PhD thesis, for the computing of this multi-phase flow model, is presented. Lastly, we derive the new advection-diffusion equation obtained from the multi-phase flow model.
- In chapter III this development is assessed in comparison with the bidisperse discrete numerical simulations of size segregation in bedload transport of Chassagne et al. (2020b). The comparison with discrete simulations also bring new insights on the comprehension of vertical size sorting in granular media and in particular in bedload transport.
- Chapter IV presents the experiments we carried out for a large particle (called “intruder”) in a bedload configuration. First, we present the experimental set-up and the tools developed for analysing the results. Then, we present the results of this experimental investigation. The results are finally discussed and assessed against the forces used in II.
- Chapter V concludes this work and outlines future perspectives for the comprehension and the continuum modeling of size segregation in bedload transport.

CHAPTER I: INTRODUCTION

CHAPITRE II

THEORETICAL MODELING: FROM GRANULAR INTERACTIONS TO CONTINUUM MODELING

Les phénomènes physiques se produisent habituellement à une échelle de mesure qui leur est propre. La structure de l'Univers par exemple, se décrit au mieux à des échelles de longueur de millions d'années-lumière. La structure d'un microbe implique des échelles plus proche du micron. Je soupçonne que cette interaction entre phénomènes et échelles de mesure n'est en fait qu'un artefact dû au limites de l'esprit humain, plutôt qu'une vérité authentique de la nature [...] la nature opère sur toutes les échelles simultanément.

Dieu joue-t-il aux dés?
Ian STEWART

In chapter I, the necessity to account for vertical size sorting in bedload transport models has been addressed. Solving the discrete contact forces between all the particles on an entire river reach is not a possibility because there is no computer sufficiently efficient to solve such an amount of contact forces. A solution consists to see the particles as a continuum phase with averaged physical quantities. By doing so, the various particle sizes can be considered as different phases that interact through macroscopic forces. The main issue is then to provide the equations for each continuum phase with its interaction forces. In this section, we present a theoretical model to deal with this issue in bedload transport, in the simplest configuration made of two particle sizes. Recently, granular scale experiments have improved our general knowledge on the physics of grain-size segregation and provide pertinent forces to model the interactions without considering the contact forces ([Tripathi and Khakhar, 2013](#); [Guillard et al., 2016](#)). Taking advantage of those recent developments, a Lagrangian equation for the segregation of a single large particle in bedload transport is proposed. This equation is then used as a starting point to develop a multi-phase flow model for a bidisperse bed in bedload transport. To do so, the spatial averaging process of [Jackson \(1997, 2000\)](#) is used and a numerical algorithm is developed to solve the obtained equations. Finally, based on this multi-phase flow model and inspired by the work of [Thornton et al. \(2006\)](#), a single advection-diffusion equation for the vertical segregation of a bidisperse mixture is proposed.

II.1 A large intruder in a bed of small particles

As a first step, the force balance applied on a single large grain in an immersed granular medium made of smaller particles is presented. This Lagrangian equation of motion for the large intruder is then made dimensionless using classical scalings for granular flows, with the large particle diameter as the length scale. An order of magnitude analysis makes it possible to discriminate the most important forces for bedload transport application.

II.1.1 General equation

A large particle of diameter d_l , of volume V_l , of surface A_l and of density ρ^l is buried in a bed of height h made of immersed small particles. The small particles are of density ρ^s with a volume fraction constant and supposed equal to its maximum value Φ_{max} and the small particle velocity is \mathbf{U}^s . The fluid has a density ρ^f and a velocity \mathbf{U}^f . From a theoretical approach, when the large intruder moves, its velocity is \mathbf{U}^l and the Newton's second law gives

$$\rho^l V_l \frac{d\mathbf{U}^l}{dt} = \mathbf{P} + \int_{A_l} \mathbf{S}^f \cdot \mathbf{n} \, dA + \int_{A_l} \mathbf{S}^p \cdot \mathbf{n} \, dA, \quad (\text{II.1})$$

where $\mathbf{P} = \rho^l V_l \mathbf{g}$ is the weight of this particle and \mathbf{S}^f and \mathbf{S}^p are respectively the absolute stress tensor for the surrounding fluid and the surrounding small particles. Following Guazzelli et al. (2011), it is more convenient to express the absolute stress tensor of the fluid as

$$\mathbf{S}^f = \boldsymbol{\sigma}_d^f - p^f \mathbf{I} \cdot \mathbf{n}, \quad (\text{II.2})$$

where $\boldsymbol{\sigma}_d^f$ is the dynamic stress tensor and $p^f \mathbf{I} \cdot \mathbf{n}$ is the hydrostatic stress field. Then, expression (II.2) makes it possible to express the total surface stress applied by the fluid to the large particle as

$$\int_{A_l} \mathbf{S}^f \cdot \mathbf{n} \, dA = \int_{A_l} \boldsymbol{\sigma}_d^f \cdot \mathbf{n} \, dA - \underbrace{\int_{A_l} p^f \mathbf{I} \cdot \mathbf{n} \, dA}_{\boldsymbol{\Pi}_f}. \quad (\text{II.3})$$

Using the divergence theorem $-\int_{A_l} p^f \mathbf{I} \cdot \mathbf{n} \, dA = -\int_{V_l} \nabla p^f \, dV$, and if ∇p^f is constant, one can easily identify the well known buoyancy force $\boldsymbol{\Pi}_f = -V_l \nabla p^f$. The first term of the Right Hand Side (RHS) of equation (II.2) represents the dynamical forces which arise if the fluid is in motion.

Following this approach, we assume that the total surface stress applied by the small particles on the large particle reads

$$\int_{A_l} \mathbf{S}^p \cdot \mathbf{n} \, dA = \int_{A_l} \boldsymbol{\sigma}_d^p \cdot \mathbf{n} \, dA - \underbrace{\frac{1}{\Phi_{max}} \int_{A_l} p^s \mathbf{I} \cdot \mathbf{n} \, dA}_{\boldsymbol{\Pi}_p}, \quad (\text{II.4})$$

where Φ_{max} is the maximum volume fraction of small particles at rest and p^s the static pressure of small particles. Again, we assume that we can use the divergence

theorem in order to obtain the granular buoyancy force:

$$\Pi_p = -\frac{V_l}{\Phi_{max}} \nabla p^s. \quad (\text{II.5})$$

If the water and the particles are at rest, the momentum equations for the fluid (II.6) and the small particles (II.7) read:

$$-\rho^f(1-\Phi)\mathbf{g} + (1-\Phi)\nabla p^f = 0 \quad (\text{II.6})$$

$$\rho^s\Phi\mathbf{g} - \nabla p^s - \Phi\nabla p^f = 0. \quad (\text{II.7})$$

Combining both equations implies the static pressure p^s to satisfy

$$\nabla p^s = \Phi_{max}(\rho^s - \rho^f)\mathbf{g} \quad (\text{II.8})$$

The first term of the RHS of equation (II.4) represents other potential interaction forces, with the surrounding small particles, that arise if the media is in motion.

II.1.2 Force balance on a large intruder segregating in a bed of small particles

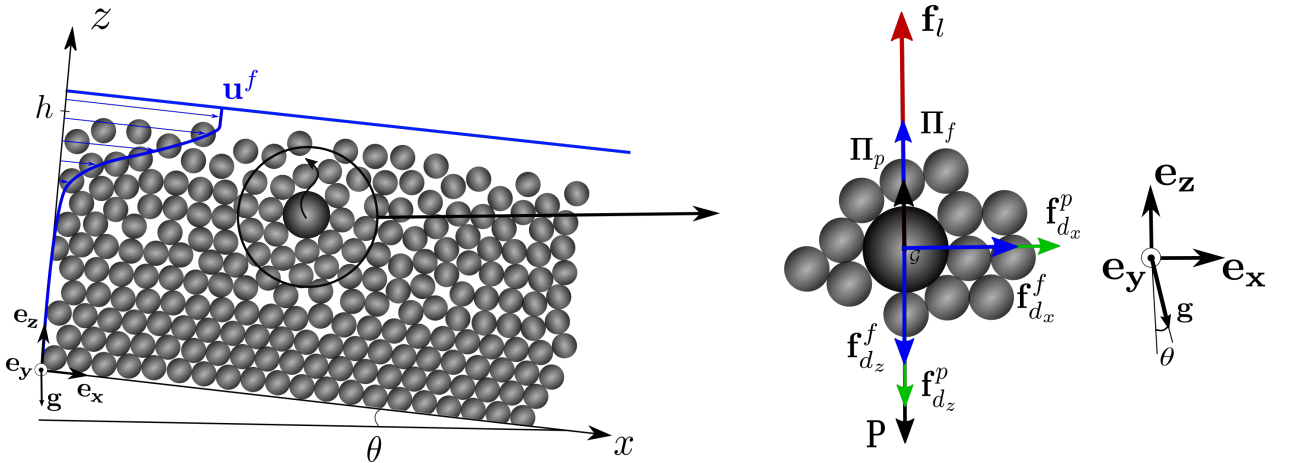


FIG. II.1: Forces acting on a large intruder. Π_f (—) is the buoyancy due to the fluid, Π_p (—) is the granular buoyancy and \mathbf{f}_l (—) is the lift force identified by Guillard et al. (2014, 2016). The particle is also submitted to the drag forces $\mathbf{f}_d^p = \mathbf{f}_{d_x}^p + \mathbf{f}_{d_z}^p$ (—) and $\mathbf{f}_d^f = \mathbf{f}_{d_x}^f + \mathbf{f}_{d_z}^f$ (—) respectively due to the interaction with small particles (Tripathi and Khakhar, 2013) and the fluid.

The configuration sketched in figure II.1 represents a steady and uniform bedload configuration: with the gravity, the water flows above and inside the small particles with a velocity $\mathbf{U}^f = u^f(z)\mathbf{e}_x$, allowing small particles to be transported along the streamwise direction. A particle shear-rate $\dot{\gamma}^p(z)$ develops and the buried large intruder is expected to segregate vertically. During the segregation process it is supposed that the displacement of the large particle in the lateral (y) direction is negligible so its velocity is $\mathbf{U}^l = u^l(z)\mathbf{e}_x + w^l(z)\mathbf{e}_z$, where u^l and w^l are respectively the streamwise and the

vertical segregating velocities.

From equations (II.1), (II.2) and (II.4), the buried intruder is submitted to its own weight \mathbf{P} , the fluid buoyancy $\mathbf{\Pi}_f$ and the granular buoyancy $\mathbf{\Pi}_p$. In addition, due to the segregation motion, the intruder is moving and is submitted to the force given by the fluid and particle dynamic stress tensors integrated over its surface

$$F = \int_{A_l} \boldsymbol{\sigma}_d^f \cdot \mathbf{n} \, dA + \int_{A_l} \boldsymbol{\sigma}_d^p \cdot \mathbf{n} \, dA \quad (\text{II.9})$$

The particulate Reynolds number based on the vertical velocity $Re_p = d_l \rho^f w^l / \eta^f$ is supposed to be very small in the bed and fluid inertial effects should be negligible at the particle length scale. Therefore, the integral of the fluid dynamic stress over the surface reduces to a drag force which can be approximated by the Stokes law (Stokes, 1851)

$$\int_{A_l} \boldsymbol{\sigma}_d^f \cdot \mathbf{n} \, dA = \mathbf{f}_d^f = 3\pi\eta^f d_l (\mathbf{U}^f - \mathbf{U}^l), \quad (\text{II.10})$$

where η^f is the fluid dynamical viscosity. Note that the assumption of negligible inertial effects at the particle length scale is debatable. Indeed, if we consider that the intruder can rise abruptly, its averaged velocity is small but its instantaneous velocity could be high. Considering the instantaneous velocity of the intruder in the particulate Reynolds number could show that the drag is in fact inertial. We suppose that frictional phenomena are more important in the bed, at least in the quasi-static regime, and thus the form of the drag force should have a low impact. As a first approximation the viscous drag force is kept.

When the granular bed is in motion, Guillard et al. (2014) and Van der Vaart et al. (2018) observed that a lift force develops around the intruder. They reported that this force emerged from a complex asymmetric stress contribution of the small particles on the intruder. In addition, when segregating among the small particles, the intruder should be submitted to a frictional drag force proportional to the depth. The second RHS term of equation (II.9) describes the interaction forces between the intruder and the surrounding small particles in motion. We suppose that both the lift force, responsible for size segregation and the frictional drag force are comprised in this term. Thus we propose that

$$\int_{A_l} \boldsymbol{\sigma}_d^p \cdot \mathbf{n} \, dA = \mathbf{f}_d^p + \mathbf{f}_l, \quad (\text{II.11})$$

where \mathbf{f}_d^p is the frictional drag force and \mathbf{f}_l is the lift force. With equations (II.11), (II.10) and (II.1) it is possible to propose a Lagrangian momentum equation for the intruder:

$$\rho^l V_l \frac{d\mathbf{U}^l}{dt} = \mathbf{P} + \mathbf{\Pi}_f + \mathbf{f}_d^f + \mathbf{f}_d^p + \mathbf{\Pi}_p + \mathbf{f}_l. \quad (\text{II.12})$$

II.1.3 Granular drag and lift forces

For a heavy particle sinking into lighter particles, Tripathi and Khakhar (2013) proposed to model the frictional drag force as a Stockesian drag force

$$\mathbf{f}_d^p = c(\Phi)\pi\eta^s d_l (\mathbf{U}^s - \mathbf{U}^l), \quad (\text{II.13})$$

where $\eta^s = |\tau^s|/\dot{\gamma}^s$ is the granular viscosity of the bed made of small particles and $c(\Phi)$ is a coefficient that could slightly depend on the local volume fraction Φ . Nevertheless, [Tripathi and Khakhar \(2013\)](#) showed that approximating $c(\Phi)$ as a constant equal to 3 was a good option at first order. In this work, it is proposed to model the frictional drag force on the large intruder using this stokesian drag force with a constant drag coefficient $c = 3$.

[Guillard et al. \(2014, 2016\)](#) were able to propose a size segregation force for an intruder (see equation (I.8) in the introduction) as

$$\mathbf{f}_{seg} = -V_l \left(\mathcal{F}(\mu) \frac{\partial p^s}{\partial z} + \mathcal{G}(\mu) \frac{\partial |\tau^s|}{\partial z} \right) \mathbf{e}_z, \quad (\text{II.14})$$

Where $\mathcal{F}(\mu)$ and $\mathcal{G}(\mu)$ are empirical functions depending on the friction coefficient $\mu = |\tau^s|/p^s$. It is demonstrated thereafter that

$$\mathbf{f}_{seg} = \mathbf{f}_l + \mathbf{\Pi}_p,$$

meaning that the segregation force proposed by [Guillard et al. \(2016\)](#) accounts for the buoyancy force and the lift force effect observed by ([Guillard et al., 2014](#)).

Considering an immobile bed where $\rho^s = \rho^l = \rho^p$, segregation should stop and therefore $w^l = 0$. Thus, the drag force vanishes and the friction coefficient should be equal to the static friction coefficient $\mu = \mu_c$. In this case, to satisfy the momentum balance of equation (II.12), the segregation force has to counterbalance the weight of the particle as

$$(\rho^p - \rho^f) g \cos \theta + \mathcal{F}(\mu_c) \frac{\partial p^s}{\partial z} = 0. \quad (\text{II.15})$$

In (II.15), the particle pressure gradient is $\partial p^s / \partial z = -\Phi_{max}(\rho^p - \rho^f)g \cos \theta$ from equation (II.8). Introducing this expression of the pressure gradient in equation (II.15), it finally imposes that

$$\mathcal{F}(\mu_c) = \frac{1}{\Phi_{max}} \quad (\text{II.16})$$

and shows that the segregation force should balance the hydrostatic particle pressure, at rest.

The empirical function $\mathcal{F}(\mu)$ proposed by [Guillard et al. \(2016\)](#) is plotted in figure II.2 with the red continuous line. One can observe that at rest, when $\mu = \mu_c$, the empirical function does not satisfy condition (II.16) and thus do not satisfy the hydrostatic. To correct it, we rewrite

$$\mathcal{F}(\mu) = \frac{1}{\Phi_{max}} + \mathcal{F}_l(\mu), \quad (\text{II.17})$$

with $\mathcal{F}_l(\mu) = (1 - e^{-70(\mu - \mu_c)})$. This new empirical function (II.17) is plotted with a blue continuous line in figure II.2. One can see that it is close to the formulation of [Guillard et al. \(2016\)](#) for $\mu \gg \mu_c$ but decreases to $1/\Phi_{max}$ in the static regime.

Finally, the lift force can be expressed from equation (II.14) by removing the buoyancy of equation (II.5) from the segregation force

$$f_l = -V_l \left(\mathcal{F}(\mu) \frac{\partial p^s}{\partial z} + \mathcal{G}(\mu) \frac{\partial |\tau^s|}{\partial z} \right) - \frac{V_l}{\Phi_{max}} \frac{\partial p^s}{\partial z} = -V_l \left(\mathcal{F}_l(\mu) \frac{\partial p^s}{\partial z} + \mathcal{G}(\mu) \frac{\partial |\tau^s|}{\partial z} \right), \quad (\text{II.18})$$

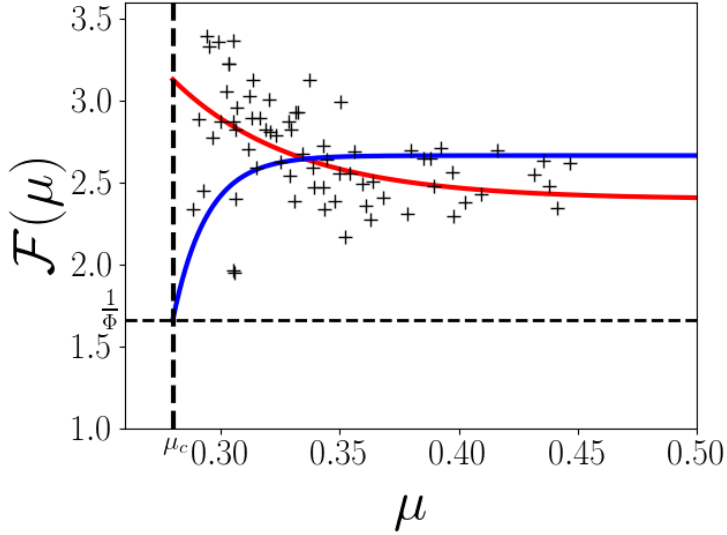


FIG. II.2: Empirical segregation function $\mathcal{F}(\mu)$ of the segregation force $f_{seg} = V_l \mathcal{F}(\mu) \partial p^s / \partial z$ found by Guillard et al. (2016) as a function of the local friction coefficient μ . + are the simulation results found by Guillard et al. (2016) using DEM. — is the function they proposed and — is $\mathcal{F}(\mu) = 1/\Phi + (1 - e^{-70(\mu - \mu_c)})$, the improved function proposed.

II.1.4 Dimensionless equation for the large intruder

In order to identify the dominant terms in the Lagrangian equation (II.12). It is made dimensionless using classical scalings for granular flows:

$$U^k = \sqrt{d_l g} \tilde{U}^k, \quad z = d_l \tilde{z}, \quad t = \sqrt{d_l/g} \tilde{t}, \quad p^k = \rho^l d_l g \tilde{p}^k \quad \text{and} \quad \tau^k = \rho^l d_l g \tilde{\tau}^k \quad (\text{II.19})$$

where $k = s, l$ or f respectively for the surrounding small particles, the large intruder and the fluid. Introducing these variables into equation (II.12), one obtains the streamwise and the vertical dimensionless equations for the large intruder

$$\frac{d\tilde{u}^l}{d\tilde{t}} = \frac{\tilde{u}^f - \tilde{u}^l}{St^f} + \frac{\tilde{u}^s - \tilde{u}^l}{St^p} \quad (\text{II.20})$$

$$\frac{d\tilde{w}^l}{d\tilde{t}} = \frac{\tilde{w}^f - \tilde{w}^l}{St^f} + \frac{\tilde{w}^s - \tilde{w}^l}{St^p} - \mathcal{F}_l(\mu) \frac{\partial \tilde{p}^s}{\partial \tilde{z}} - \mathcal{G}(\mu) \frac{\partial \tilde{\tau}^s}{\partial \tilde{z}}. \quad (\text{II.21})$$

In these equations, the weight of the intruder has vanished since it is counterbalanced by the granular buoyancy Π_p . Equations (II.20) and (II.21) contains two dimensionless numbers based on $\mathcal{W} = \sqrt{d_l g}$, the characteristic velocity of the large particle. The fluid Stokes number

$$St^f = \frac{\rho^l d_l \mathcal{W}}{18 \eta^f}, \quad (\text{II.22})$$

which compares the inertia of the large intruder with the viscous friction exerted by the fluid and the granular Stokes number

$$St^p = \frac{\rho^l d_l \mathcal{W}}{6 c \eta^s}, \quad (\text{II.23})$$

which compares the inertia of the large intruder with the granular viscosity associated with the small particles.

Assuming a classical bedload configuration, the small and large particles have the same density ($\rho^s = \rho^l = \rho^p$) and the fluid flows above and inside the porous matrix of the granular bed. At the top of the bed, particles encounter diluted and dense flow regimes. Below a certain depth, $\mu \leq \mu_c$, meaning that the grains are in the quasi-static regime. We suppose that typical values of the granular viscosity for dense granular flows are very high compared with the water viscosity. This results in a fluid Stokes number St^f much larger than the granular Stokes number St^p whatever the position in the bed. Therefore, the first term in the RHS of both equations (II.20) and (II.21), representing the fluid drag force, can be neglected. In addition, [Tripathi and Khakhar \(2011\)](#) reported that the disturbance velocity generated by the moving intruder was limited to a distance equal to $3/2 d_l$. Even if their experiment was made with an intruder of the same size and for higher shear stress, it is assumed that it is still valid in the present case. Therefore, the vertical velocity of the intruder does not disturb the vertical bulk velocity, implying that $w^s \sim 0$. Note that this assumption is debatable. Particularly in the quasi-static regime where the motion of the intruder by rearrangement affects a large part of the granular bed, meaning that the disturbance can go beyond the distance of $3/2 d_l$ proposed by [Tripathi and Khakhar \(2011\)](#) and that it is possible that the vertical bulk velocity becomes non-negligible.

Focusing on the position of the intruder in the quasi-static part of the bed, it is assumed that the total solid volume fraction is constant, $\Phi = cste$. Therefore, in our configuration, equations (II.20) and (II.21) can be written as

$$\frac{d\tilde{u}^l}{d\tilde{t}} = \frac{\tilde{u}^s - \tilde{u}^l}{St^p} \quad (\text{II.24})$$

$$\frac{d\tilde{w}^l}{d\tilde{t}} + \frac{1}{St^p} \tilde{w}^l = -\mathcal{F}_l(\mu) \frac{\partial \tilde{p}^s}{\partial \tilde{z}} - \mathcal{G}(\mu) \frac{\partial \tilde{\tau}^s}{\partial \tilde{z}}. \quad (\text{II.25})$$

In these dimensionless equations the fluid only acts through the fluid density coming from the granular pressure and shear stress gradient. Therefore the fluid can be considered as inert and equations (II.24) and (II.25) should also be valid to model the velocity of an intruder segregating in a dry granular flow (in this case the granular pressure gradient does not include the fluid density). For bedload configurations, the slope rarely exceeds $\tan \theta = 10\%$ and thus the streamwise gravity component is negligible, making the contribution of the shear stress gradient negligible. Thus, the shear stress gradient will be neglected in the rest of this work. The final equation for a bedload configuration is therefore

$$\frac{d\tilde{u}^l}{d\tilde{t}} = \frac{\tilde{u}^s - \tilde{u}^l}{St^p} \quad (\text{II.26})$$

$$\frac{d\tilde{w}^l}{d\tilde{t}} + \frac{1}{St^p} \tilde{w}^l = -\mathcal{F}_l(\mu) \frac{\partial \tilde{p}^s}{\partial \tilde{z}}. \quad (\text{II.27})$$

Equations (II.26) and (II.27) allows one to identify the main size segregation mechanisms. On the streamwise direction, the acceleration of the intruder is driven by the

drag force. On the vertical axis, it shows that the vertical segregation of a large intruder can be seen as a simple relaxation process with characteristic time St^p .

II.2 Volume averaged multi-phase flow model for vertical-size segregation in bedload transport

In the previous section, it was shown that the segregation force proposed by [Guillard et al. \(2016\)](#) for a large particle, accounted for both the buoyancy and the lift force. A new formulation of this force has been proposed in order to strictly separate the lift and the buoyancy force. Based on this new formulation and also on the granular drag force proposed by [Tripathi and Khakhar \(2013\)](#), a Lagrangian equation for the segregation of a single large particle in a bed of immersed small particles has been proposed. In this section, the goal is to make the link between this discrete picture with one large particle and a continuum model for the vertical size segregation of an ensemble of large particles. As mentioned in the introduction, this change of scale is necessary to model size segregation at larger scales. This is done in the framework of the volume averaged equations of [Jackson \(1997, 2000\)](#) which in this case will provide Euler equations. The reader has to imagine that the problem is observed from a macroscopic perspective in which grains are not discernible anymore and one can only see three continuum phases that interact together: small particles, large particles and the fluid. The forces proposed in the Lagrangian equation will provide the closures for the interaction forces in the momentum balance of each phase.

II.2.1 3D general governing equations

Following [Jackson \(1997, 2000\)](#), the mass and momentum balance equations for the three phases are given by

$$\frac{\partial \epsilon \rho^f \langle \mathbf{u}^f \rangle}{\partial t} + \nabla \cdot (\epsilon \rho^f \langle \mathbf{u}^f \rangle) = 0, \quad (\text{II.28})$$

$$\frac{\partial \Phi^i \rho^p \langle \mathbf{u}^i \rangle}{\partial t} + \nabla \cdot (\Phi^i \rho^p \langle \mathbf{u}^i \rangle) = 0, \quad (\text{II.29})$$

$$\frac{\partial \epsilon \rho^f \langle \mathbf{u}^f \rangle}{\partial t} + \nabla \cdot (\epsilon \rho^f \langle \mathbf{u}^f \rangle \otimes \langle \mathbf{u}^f \rangle) = \nabla \cdot \mathbf{S}^f - \epsilon \rho^f \mathbf{g} - n_l \mathbf{f}^{f \rightarrow l} - n_s \mathbf{f}^{f \rightarrow s} \quad (\text{II.30})$$

$$\frac{\partial \Phi^i \rho^p \langle \mathbf{u}^i \rangle}{\partial t} + \nabla \cdot (\Phi^i \rho^p \langle \mathbf{u}^i \rangle \otimes \langle \mathbf{u}^i \rangle) = \nabla \cdot \mathbf{S}^i - \Phi^i \rho^p \mathbf{g} + n_i \mathbf{f}^{f \rightarrow i} \pm n_l \mathbf{f}^{s \rightarrow l}, \quad (\text{II.31})$$

where \otimes is the dyadic product, f denotes the fluid phase and indices $i = l, s$ denote the large particle phase and the small particle phase respectively. Φ^l and Φ^s are the volume fractions for the large and small grains and verify $\Phi^s + \Phi^l = \Phi$ where Φ is the volume fraction of the mixture, i.e. the total solid volume fraction. Consequently, the fluid volume fraction is $\epsilon = 1 - \Phi^l - \Phi^s$. \mathbf{S}^k is the stress tensor associated with phase k with $k = l, s$ or f . They can be separated into pressure and shear stress contribution

$$\mathbf{S}^k = -p^k \mathbf{I} + \tau^k, \quad (\text{II.32})$$

where τ^k is the shear stress tensor and p^k is the pressure of phase k .

The momentum equations (II.30) and (II.31) contain two terms coming from the momentum exchange between the different phases: $n_i \mathbf{f}^{f \rightarrow i}$ and $n_i \mathbf{f}^{s \rightarrow l}$. In these terms, n_i is the number of particles of phase i per unit volume and is defined as $n_i = \Phi^i / V^i$ (Jackson, 2000), with V^i the volume of a single particle of phase i .

The term $n_i \mathbf{f}^{f \rightarrow i}$ is the averaged value of the resultant forces exerted by the fluid on the particles of phase i . Jackson (2000) showed that for a collection of immersed particles, this interaction force can be written as

$$n_i \mathbf{f}^{f \rightarrow i} = -\Phi^i \nabla p^f + n_i \mathbf{f}_d^{f \rightarrow i}, \quad (\text{II.33})$$

where $\Phi^i \nabla p^f$ is the buoyancy force exerted by the fluid phase on the particles and $n_i \mathbf{f}_d^{f \rightarrow i}$ is the particle averaged drag force between the particles and the fluid phase. Note that other solid/fluid interaction forces such as the lift force or the added mass force could be considered. From Jha and Bombardelli (2010), the lift force represents 4% of the solid/fluid interaction forces and it could reach 10% for the added mass force. However, these forces are supposed to be significant in the dilute regime which is not notable in our case.

The term $n_i \mathbf{f}^{s \rightarrow l}$ is the averaged value of all interacting forces between large and small particle phases. It can be directly expressed in 3D from the local segregation force of Tripathi and Khakhar (2013) and Guillard et al. (2016).

The developed model is general and can be applied to 3D configurations. To make the model more comprehensible for the reader and for the purpose of the present study, the model will be only developed for a 1D uniform flow.

II.2.2 Simplified 1D vertical multi-phase flow model

The multi-phase flow model (equations II.28 to II.31) is simplified by considering a uniform flow in the streamwise direction. From now, all the variables only depend on the vertical position z . The spatially averaged velocity of the phase k can be written as $\langle \mathbf{u}^k \rangle = \langle u^k \rangle(z) \mathbf{e}_x + \langle w^k \rangle(z) \mathbf{e}_z$. The mass conservation equations simplify to

$$\frac{\partial \epsilon}{\partial t} + \frac{\partial \epsilon \langle w^f \rangle}{\partial z} = 0 \quad \text{and} \quad \frac{\partial \Phi^i}{\partial t} + \frac{\partial \Phi^i \langle w^i \rangle}{\partial z} = 0, \quad (\text{II.34})$$

and the momentum balance equations in the vertical direction are:

$$\rho^f \left[\frac{\partial \epsilon \langle w^f \rangle}{\partial t} + \frac{\partial \epsilon \langle w^f \rangle \langle w^f \rangle}{\partial z} \right] = -\epsilon \frac{\partial p^f}{\partial z} - \epsilon \rho^f g \cos \theta - n_l \langle f_d^{f \rightarrow l} \rangle - n_s \langle f_d^{f \rightarrow s} \rangle, \quad (\text{II.35})$$

$$\begin{aligned} \rho^p \left[\frac{\partial \Phi^l \langle w^l \rangle}{\partial t} + \frac{\partial \Phi^l \langle w^l \rangle \langle w^l \rangle}{\partial z} \right] &= -\frac{\partial p^l}{\partial z} - \Phi^l \frac{\partial p^f}{\partial z} - \Phi^l \rho^p g \cos \theta \\ &\quad + n_l \langle f_d^{f \rightarrow l} \rangle + n_l \langle f^{s \rightarrow l} \rangle, \end{aligned} \quad (\text{II.36})$$

$$\begin{aligned} \rho^p \left[\frac{\partial \Phi^s \langle w^s \rangle}{\partial t} + \frac{\partial \Phi^s \langle w^s \rangle \langle w^s \rangle}{\partial z} \right] &= -\frac{\partial p^s}{\partial z} - \Phi^s \frac{\partial p^f}{\partial z} - \Phi^s \rho^p g \cos \theta \\ &\quad + n_s \langle f_d^{f \rightarrow s} \rangle - n_l \langle f^{s \rightarrow l} \rangle, \end{aligned} \quad (\text{II.37})$$

where θ is the angle of inclination (see figure II.1).

To solve these equations, it is necessary to prescribe closures for the spatially averaged fluid/grain interaction and grain-grain interactions, and for the granular and fluid pressures.

Considering the fluid-grain interaction, both small and large granular phases interact with the fluid phase through $\Phi^i \partial p^f / \partial z$ and the drag force $n_i \mathbf{f}_d^{f \rightarrow i}$. As described in section II.1.2, it is assumed that the drag force is viscous. This hypothesis has been made to keep the model simple. Indeed, since the drag is linear, the spatial averaging is simply the drag force applied on one particle (given in (II.10)) of phase i multiplied by the number of particles per unit volume $n_i = \Phi^i / V^i$ (Jackson, 2000). Therefore, for an assembly of particles, the spatial averaging of the vertical total drag force applied by the fluid gives

$$n_i \langle f_d^{f \rightarrow i} \rangle = \frac{\Phi^i \rho^p}{t_i} (\langle w^f \rangle - \langle w^i \rangle), \quad (\text{II.38})$$

where $t_i = \rho^p d_i^2 (1 - \Phi)^3 / 18\eta^f$ is the particle response time and d_i is the particle diameter of phase i . The factor $(1 - \Phi)^3$ is a correction proposed by Richardson and Zaki (1954) to take into account hindrance effects.

The granular phases also interact with each other and the grain-grain interaction closure should be prescribed in the model. For a single large grain in a bed of small particles, it has been shown in section II.1.2 that small particles exert two forces on a large intruder,

$$f^{s \rightarrow l} = f_d^p + f_{seg}. \quad (\text{II.39})$$

To extend these forces to a collection of large particles, the interaction force $f^{s \rightarrow l}$ is spatially averaged. Since this force is linear, it amounts to multiply $f^{s \rightarrow l}$ by the number of large particles per unit volume $n_l = 6\Phi^l / \pi d_l^3$. In addition, in the case of spatially averaged equations, the force balancing the weight Π_p already appears in the term $-\partial p^i / \partial z$. Hence, the averaged segregation force reduces to the granular lift force. Therefore, the total solid interaction force exerted by the small particles on the large particles is given by

$$n_l \langle f^{s \rightarrow l} \rangle = \frac{\Phi^l \rho^p}{t_{ls}} (\langle w^s \rangle - \langle w^l \rangle) - \Phi^l \mathcal{F}_l(\mu) \frac{\partial p^m}{\partial z}, \quad (\text{II.40})$$

where $t_{ls} = \rho^p d_l^2 / 6c\eta^p$ is the particle response time for the drag force between small and large particles and $\mathcal{F}_l(\mu) = (1 - e^{-70(\mu - \mu_c)})$. The pressure p^m is the mixture pressure and represents the total pressure arising from both solid phases. The solid mixture phase is made of both particle phases and is noted with $i = m$. Its momentum balance is obtained by summing (II.36) and (II.37). Since the mixture does not distinguish between small and large particles, the solid interaction forces, contained in $n_l \langle f^{s \rightarrow l} \rangle$, should cancel out in this equation. This is ensured by the fact that the term $n_l \langle f^{s \rightarrow l} \rangle$ is positive in the momentum conservation equation for the large particles (II.36) and negative in the momentum conservation equation for the small particles (II.37).

II.2.3 Closures for the granular stress

In the case of dense granular flows, for a granular phase i , the normal component of the granular stress p^i mostly comes from the static part of the granular stress and normal contact force from binary collisions can be neglected. The static stress is the result of enduring contact forces within a given particle phase. Also, in an average sense, it represents the resistance to compression of the granular media. In this way, once all the particles have settled, the bed is supposed at rest and it is expected that the mixture particle pressure supports the weight of the particles such that :

$$p^m = \Phi (\rho^p - \rho^f) g \cos \theta (h - z) \quad (\text{II.41})$$

This terms should vanish when there is no contact between the particles and appears when chain forces between the particles starts to develop. It is well known in granular media that such a network of contacts develop when the volume fraction exceeds the random loose packing fraction ($\Phi_{rlp} = 0.55$ for spheres).

However, formula (II.41) cannot be used to model the settling of particles because, in this case, the system is not stationary. In addition, the Eulerian description does not make it possible to access the particle-particle interaction forces explicitly. For these reasons, it is more convenient to use an empirical model that only depends on the local volume fraction or the velocities. Such a model has been proposed by (Johnson and Jackson, 1987) as

$$p^m = \begin{cases} P_0 \frac{(\Phi - \Phi_{min}^{Fric})^3}{(\Phi_{max} - \Phi)^5} & \text{for } \Phi \geq \Phi_{min}^{Fric} \\ 0 & \text{Otherwise,} \end{cases} \quad (\text{II.42})$$

where P_0 is a constant depending on the material. From Chauchat et al. (2017), for spheres, $P_0 = 0.05$ Pa, $\Phi_{min}^{Fric} = 0.57$ and $\phi_{max} = 0.635$. In this model, the particle pressure is a diverging function of ϕ at the random close packing fraction ϕ_{max} . This model is not very satisfactory as it is purely empirical. Therefore another alternative could be to use the formula proposed by Lee and Huang (2018):

$$p^m = K [max(\Phi - \Phi_0, 0)]^\chi \left\{ 1 + \sin \left[max\left(\frac{\Phi - \Phi_0}{\Phi_{max} - \Phi_0}, 0\right) \pi - \frac{\pi}{2} \right] \right\}, \quad (\text{II.43})$$

where K is the Young modulus and Φ_0 and χ depend on the material deformation. Contrary to equation (II.42), this formula has a finite value at random close packing Φ_{max} which is numerically more stable. However it requires more parameters to calibrate contrary to the formulation (II.42) which only depends on the local volume fraction. In this way, equation (II.42) will be used.

The particle pressure for phase i is also needed in equation (II.62). Thanks to the mixture model approach (Morland, 1992), it can be assumed that each particle phase carries the total overburden pressure p^m according to their local volume fraction as

$$p^i = \frac{\Phi^i}{\Phi} p^m, \quad (\text{II.44})$$

To solve the 1D vertical governing equations (II.35) to (II.37), one can see that there is no need to determine a shear stress on either phases. The shearing force exerted by the fluid on the grains only comes out through the presence of the granular viscosity η^p and the friction coefficient μ in the granular drag and the lift forces (see equation II.40). The estimation of both parameters requires a granular rheology. The difficulty is that there is, at this time, no consensus regarding a simple granular rheological law that could describe accurately both the dense flow regime and the quasi-static regime encountered in the bed. To my knowledge, only the model of [Baumgarten and Kamrin \(2019\)](#) could do it for the entire bed by modeling the quasi-static regime with a DEM model coupled with a Material Point Method model for the dense flow regime. The implementation of such a model is far from easy and the purpose here is to focus on the effect of the segregation model while putting aside potential discrepancies linked to a non-accurate description of the granular rheology. A more adapted solution consists in importing the granular viscosity and friction coefficient profiles from corresponding discrete numerical simulations. It will be done using the discrete numerical simulations of [Chassagne et al. \(2020b\)](#). Therefore, the configurations modeled to validate the 1D model will be the same as [Chassagne et al. \(2020b\)](#) and simulations will be compared to their discrete data. The grain scale numerical simulation of [Chassagne et al. \(2020b\)](#) as well as the process to extract the granular viscosity and friction coefficient profiles will be described in details in the next chapter dedicated to the validation of the multi-phase flow model(see chapter [III](#)).

II.2.4 Numerical implementation

Equations (II.34) to (II.37) model the three distinct phases that need to be solved: the fluid phase, the large particle phase and the small particle phase. The momentum equations (II.35) to (II.37) are coupled together by the fluid pressure term p^f , the mixture pressure p^m and their velocities (see the inter-phases forces II.38 and II.40). Since there is no analytical solutions for such coupled non-linear partial differential equations this section aims to present the numerical algorithm that has been developped. The fluid phase is incompressible and thus, there is no equation of state that provides the fluid pressure. Therefore, a pressure-velocity algorithm is required. Such an algorithm usually splits the equations by removing the fluid pressure for which there is no closure. A first step consists in computing the velocity of each phase without this pressure. Since the fluid pressure was not taken into account, the velocities obtained does not satisfy the continuity equation but they can be used to find the fluid pressure that satisfies the continuity equation. Once the pressure is found, the velocities can be corrected. This algorithms are semi-implicit, meaning that the velocity in the advection term is solved for the new time step while the velocity in the source term is defined by the previous time step.

A common method for unstationary flows is the PISO (Pressure Implicit with Splitting Operators) algorithm. If appropriate, it provides stable results with a low iteration number. Using a PISO algorithm implemented in the *openFOAM* toolbox, [Chauchat et al. \(2017\)](#) successfully developed a 3D two-phase flow model for sediment transport called *sedFoam*. Based on it, a simpler one dimensional two-phase flow model for unidirectional sheet-flows was also proposed by [Chauchat \(2018\)](#). The numerical algorithm

described in this section is developed using the same PISO algorithm as [Chauchat et al. \(2017\)](#). The main contribution consists in adapting it to model the presence of a second solid phase. The discretisation is performed using a finite volume method even if, for 1D cases, it gives the same discretization as a finite difference method. For more simplicity, the full algorithm has been written in *Python*.

The coupling between the equations imposes stability constraint in the numerical scheme and it appeared that the most stable way to compute these equations was rather to solve the fluid phase, one solid phase and the mixture phase, which is defined as the sum of both solid phases. In this section, the solid mixture equation is first presented and the final equations before being discretized are obtained. Finally, the discretisation and the PISO algorithm developed to solve these equations are presented in more details with the successive loops.

Note that the procedure presented thereafter is written for 1D vertical equations in order to highlight the key closures for the continuum modelling of vertical size-segregation while keeping the model simple. Nevertheless, it should be noted that it remains valid for the full 3D system of equations. The 3D implementation could be done on the basis of existing 3D two-phase flow model for sediment transport, like *sedFoam* and represents a future step.

Solid mixture equation

The mass conservation equation for the mixture phase is defined by adding the mass equation of both solid phases together:

$$\frac{\partial}{\partial t} (\Phi^s + \Phi^l) + \frac{\partial}{\partial z} (\Phi^s w^s + \Phi^l w^l) = 0. \quad (\text{II.45})$$

Since

$$\Phi = \Phi^s + \Phi^l, \quad (\text{II.46})$$

and

$$\Phi w^m = \Phi^s w^s + \Phi^l w^l, \quad (\text{II.47})$$

The mixture mass equation finally reads

$$\frac{\partial \Phi}{\partial t} + \frac{\partial \Phi w^m}{\partial z} = 0. \quad (\text{II.48})$$

In the same way, the one dimensional mixture momentum conservation equation is obtained by summing equations [\(II.36\)](#) and [\(II.37\)](#) together and using equations [\(II.46\)](#), [\(II.47\)](#) and [\(II.44\)](#):

$$\begin{aligned} \rho^p \left[\frac{\partial}{\partial t} (\Phi w^m) + \frac{\partial}{\partial z} (\Phi^s w^s w^s + \Phi^l w^l w^l) \right] &= -\frac{\partial p^m}{\partial z} - \Phi \frac{\partial p^f}{\partial z} - \Phi \rho^p g \cos \theta \\ &\quad + \frac{\Phi^l \rho^p}{t_l} (w^f - w^l) + \frac{\Phi^s \rho^p}{t_s} (w^f - w^s). \end{aligned} \quad (\text{II.49})$$

In equation [\(II.49\)](#), the second LHS term cannot be linked directly to the advection of the mixture. Below, it is shown how to recover equation [\(II.54\)](#).

We need to define the drift velocity as:

$$w^{dl} = w^m - w^l \quad \text{and} \quad w^{ds} = w^m - w^s \quad (\text{II.50})$$

So the second LHS term of equation (II.49) can be written:

$$\Phi^s w^s w^s + \Phi^l w^l w^l = \Phi^s w^s (w^m - w^{ds}) + \Phi^l w^l (w^m - w^{dl}) \quad (\text{II.51})$$

$$= w^m (\Phi^s w^s + \Phi^l w^l) - \Phi^s w^s w^{ds} - \Phi^l w^l w^{dl} \quad (\text{II.52})$$

$$= \Phi w^m w^m - \Phi^s w^s w^{ds} - \Phi^l w^l w^{dl} \quad (\text{II.53})$$

However, w^{dl} and w^{ds} are supposed very small and therefore only the first RHS term of equation (II.53) remains.

With equations (II.53) and (II.49), the mixture momentum equation is

$$\begin{aligned} \rho^p \left[\frac{\partial \Phi w^m}{\partial t} + \frac{\partial \Phi w^m w^m}{\partial z} \right] &= - \frac{\partial p^m}{\partial z} - \Phi \frac{\partial p^f}{\partial z} - \Phi \rho^p g \cos \theta \\ &\quad + \frac{\Phi^l \rho^p}{t_l} (w^f - w^l) + \frac{\Phi^s \rho^p}{t_s} (w^f - w^s). \end{aligned} \quad (\text{II.54})$$

System of equations solved

The total continuity equation is defined as the sum of the continuity equations of the fluid and the mixture phases:

$$\frac{\partial \epsilon + \Phi}{\partial t} + \frac{\partial \epsilon w^f + \Phi w^m}{\partial z} = 0 \quad (\text{II.55})$$

$$\Leftrightarrow \frac{\partial \epsilon w^f + \Phi w^m}{\partial z} = 0. \quad (\text{II.56})$$

Because $\epsilon + \Phi = 1$ and by defining the volume averaged velocity: $w = \epsilon w^f + \Phi w^m$, equation (II.56) becomes

$$\frac{\partial w}{\partial z} = 0, \quad (\text{II.57})$$

i.e. the sum of all the different phases is incompressible. This is done in order to use classical algorithm for incompressible Navier-Stokes equations and therefore, the reduced fluid pressure: $\bar{p}^f = p^f - \rho^f g z$ is introduced. The set of equations that are obtained are presented below in their final form before being discretised.

$$\frac{\partial w}{\partial z} = 0 \quad (\text{II.58})$$

$$\frac{\partial \Phi}{\partial t} + \frac{\partial \Phi w^m}{\partial z} = 0, \quad (\text{II.59})$$

$$\frac{\partial \Phi^s}{\partial t} + \frac{\partial \Phi^s w^s}{\partial z} = 0. \quad (\text{II.60})$$

In order to solve the momentum conservation equations with a semi-implicit algorithm, the momentum equations need to be solved under their non-conservative form (the concentration is not in the derivatives)

$$\begin{aligned} \frac{\partial w^m}{\partial t} + w^m \frac{\partial w^m}{\partial z} + \frac{1}{t_l} w^m = & -\frac{1}{\rho^p \Phi} \frac{\partial p^m}{\partial z} - \frac{1}{\rho^p} \frac{\partial \bar{p}^f}{\partial z} - \left(1 - \frac{\rho^f}{\rho^p}\right) g \cos \theta \\ & + \frac{1}{\Phi} \left(\frac{\Phi^l}{t_l} + \frac{\Phi^s}{t_s} \right) w^f + \frac{\Phi^s}{\Phi} \left(\frac{1}{t_l} - \frac{1}{t_s} \right) w^s \quad (\text{II.61}) \end{aligned}$$

$$\begin{aligned} \frac{\partial w^s}{\partial t} + w^s \frac{\partial w^s}{\partial z} + \left(\frac{1}{t_s} + \frac{\Phi}{t_{ls}} \right) w^s = & -\frac{1}{\rho^p \Phi^s} \frac{\partial p^s}{\partial z} - \frac{1}{\rho^p} \frac{\partial \bar{p}^f}{\partial z} - \left(1 - \frac{\rho^f}{\rho^p}\right) g \cos \theta \\ & + \frac{1}{t_{ls}} w^f + \frac{\Phi}{t_{ls}} w^m + \frac{\Phi^l}{\Phi^s \rho^p} \mathcal{F}(\mu) \frac{\partial p^m}{\partial z} \quad (\text{II.62}) \end{aligned}$$

$$\begin{aligned} \frac{\partial \epsilon w^f}{\partial t} + w^f \frac{\partial \epsilon w^f}{\partial z} + \left(\frac{\rho^p \Phi^s}{\rho^f \epsilon t_s} + \frac{\rho^p \Phi^l}{\rho^f \epsilon t_l} \right) w^f = & -\frac{1}{\rho^p} \frac{\partial \bar{p}^f}{\partial z} \\ & - \frac{\rho^p \Phi^s}{\rho^f \epsilon} \left(\frac{1}{t_s} - \frac{1}{t_l} \right) w^s + \frac{\rho^p \Phi}{\rho^f \epsilon t_l} w^m \quad (\text{II.63}) \end{aligned}$$

Once these equations are solved, the large particle phase is easily solved using relations (II.46) and (II.47).

The next paragraph is dedicated to the numerical implementation of these equations, using the PISO algorithm.

Numerical implementation

The velocity-pressure algorithm implemented to solve equations (II.58) to (II.63) is presented in this paragraph. To do so, the equations are discretised in time and space. This is done using the finite volume method on a regular mesh made of N volumes. This mesh is represented in figure II.3.

Because the system is one dimensional, these volumes reduce to cells of size Δz . The velocities, the pressures and the volume fractions are solved for each cells j of the mesh. The velocities $\{w^f\}_j$, $\{w^m\}_j$ and $\{w^s\}_j$ are located at the cell faces while the scalar quantities such as volume fractions $\{\phi\}_j$, $\{\phi^s\}_j$ and pressures $\{p^f\}_j$, $\{p^m\}_j$ are located at the cell centers. Knowing the quantities $\{\Phi\}_j^n$, $\{\Phi^s\}_j^n$, $\{\Phi^l\}_j^n$, $\{\epsilon\}_j^n$, $\{w^m\}_j^n$, $\{w^s\}_j^n$, $\{w^f\}_j^n$ and $\{w^l\}_j^n$ at cell j , at time n , these values are used to solve to solve the same quantities at time $n+1$.

The PISO loop (Rusche, 2003; Chauchat et al., 2017) consists in splitting the velocities into an implicit part and an explicit part: the velocities linked to the transport terms are solved for the timestep $n+1$ while the velocities linked to the interaction forces are given by the previous timestep n . When solving at timestep $n+1$, two steps are required. A predictive step where equations are solved without the reduced fluid pressure gradient

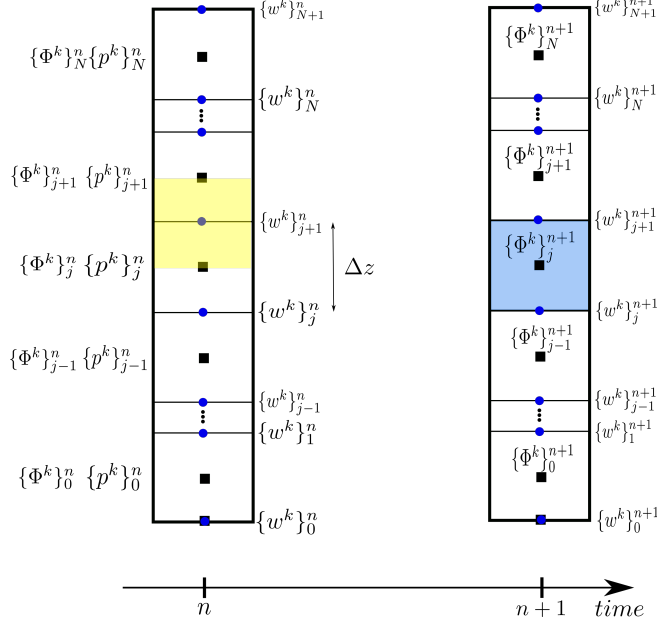


FIG. II.3: The whole domain is meshed in N cells of size Δz for each timestep n . The scalar values such as the volume fractions Φ^k and the pressures p^k are defined at the center of the cells. The velocity vectors w^k are defined at the faces of the cells. The yellow surface represents the j^{th} control volume on which the scalar values are integrated. The blue surface represents the j^{th} control volume on which the velocity fluxes are integrated.

$\partial \bar{p}^f / \partial z$. This gives intermediate velocities w^{k*} that do not satisfy the divergence free of the continuity equation.

On the contrary, with the fluid pressure, the corrected velocities w^{k**} should satisfy the continuity equation $\partial w^{k**} / \partial z = 0$. Therefore, based on the predicted velocities, the divergence free of the total velocity $\partial w^{k**} / \partial z = 0$ is used to express the fluid pressure \bar{p}^f .

The second step consists in correcting the predicted velocities w^{k*} accounting for this fluid pressure to find the velocities w^{k**} .

This gives the following successive steps:

1. Solve for $\{\Phi\}_j^{n+1}$ using $\frac{\partial \Phi}{\partial t} + \frac{\partial \Phi w^m}{\partial z} = 0$
2. Solve for $\{\Phi^s\}_j^{n+1}$ using $\frac{\partial \Phi^s}{\partial t} + \frac{\partial \Phi^s w^s}{\partial z} = 0$
3. Solve for $\{\Phi^l\}_j^{n+1}$ using $\Phi^l = \Phi - \Phi^s$
4. Solve for $\{\epsilon\}_j^{n+1}$ using $\epsilon = 1 - \Phi$
5. Solve for intermediate velocities $\{w^m\}_j^*$, $\{w^s\}_j^*$ and $\{w^f\}_j^*$ using equations (II.61) to (II.63)
6. Solve for the pressure $\{p^f\}_j^*$ using $\frac{\partial w^{**}}{\partial z} = 0$
7. Correct the velocities $\{w^m\}_j^{n+1}$, $\{w^s\}_j^{n+1}$ and $\{w^f\}_j^{n+1}$ using the new pressure

8. Calculate $\{w^l\}_j^{n+1}$ using $\{w^l\}_j^{n+1} = \frac{\{\Phi\}_j^{n+1} \{w^m\}_j^{n+1} - \{\Phi^s\}_j^{n+1} \{w^s\}_j^{n+1}}{\{\Phi^l\}_j^{n+1}}$ from equation (II.47)

In this algorithm, the only boundary conditions to apply are for the velocities. For each phase, a zero vertical velocity is applied at the bottom of cell $j = 0$. At the top of the mesh (face $N + 1$), a zero gradient condition is applied.

The full discretization of the equations are provided in the appendix. The developed *Python* solver is publicly available on gitlab:

<https://gricad-gitlab.univ-grenoble-alpes.fr/rousseau2h/3phase1d.git>.

The proposed volume-averaged multi-phase flow model describes size segregation of a bi-disperse mixture immersed in a fluid. At first sight, this model is very close from the one proposed by Thornton et al. (2006). However, it represents a significant improvement. Indeed, the volume-averaged approach allowed us to implement the particle scale segregation forces, found with physical DEM experiments, into a continuum model. More generally, our approach shows that from the investigation of the behaviour of a single particle, it is then possible, through this volume averaged method, to incorporate the underlying physics of the granular scale into the macroscopic scale. This important result will be used in the next section II.3 for the last step of our upscaling process. Based on multi-phase flow model, a more simple advection-diffusion model for size segregation will be derived, showing that the segregation process could be summarised as a simple advection-diffusion problem.

II.3 Advection-diffusion model

As mentioned previously, Thornton et al. (2006) and Gray and Ancey (2011) showed that by substituting the percolation velocity of one particle-size into the mass conservation equation, an advection-diffusion equation for the segregation of one particle phase into the other phases could be obtained. From a practical aspect, this equation is supposed to provide the same results as the multi-phase model but with a lower computational time. From a physical point of view, it shows that the segregation process can be seen as an advection and a diffusion process where the advection and the diffusion coefficients are directly defined by the underlying segregation dependencies. With their approach, Thornton et al. (2006) made the link between the multi-phase continuum model and these coefficients. Yet, the lack of physical dependencies in their interaction forces still imposes to calibrate some of the parameters appearing in the advection and diffusion coefficients. Previous studies have used advection-diffusion models for the investigation of vertical size segregation. In these studies, the idea was mainly to determine the physical dependencies in the advection and diffusion coefficients using experiments (Dolgunin et al., 1998; Van der Vaart et al., 2015; Ferdowsi et al., 2017; Cai et al., 2019). Yet the dependencies found with experiments do not give information on the particle scale processes and could still depend on the experimental configurations. The multi-phase model developed in the previous section (equations II.35 to II.37) is based on interaction forces at the particle scale, determined in independant configurations. Setting an

advection-diffusion equation from our multi-phase model would directly bring the dependencies at the particle scale into the advection and diffusion coefficients and allows one to assess the dependencies found in previous studies. In the present section, the approach of Thornton et al. (2006) and Gray and Chugunov (2006) is used to derive the advection-diffusion model.

Combining equations (II.37), (II.38), (II.40), the momentum balance of small particles can be written as:

$$\rho^p \left[\frac{\partial \Phi^s w^s}{\partial t} + \frac{\partial \Phi^s w^s w^s}{\partial z} \right] = -\frac{\partial p^s}{\partial z} - \Phi^s \frac{\partial p^f}{\partial z} - \Phi^s \rho^p g \cos \theta + \frac{\rho^p \Phi^s}{t_s} (w^f - w^s) - \frac{\rho^p \Phi}{t_{ls}} (w^s - w^m) + \Phi^l \mathcal{F}_l(\mu) \frac{\partial p^m}{\partial z}. \quad (\text{II.64})$$

The total volume fraction $\Phi = \Phi^s + \Phi^l$ is assumed to be constant since particle velocity fluctuations are small. Once all the particles have settled and the bed is at rest, the mixture momentum balance reduces to the hydrostatic pressure distribution for both the fluid and the particle phases (Chauchat, 2018):

$$\frac{\partial p^f}{\partial z} = -\rho^f g \cos \theta \quad \text{and} \quad \frac{\partial p^m}{\partial z} = -\Phi (\rho^p - \rho^f) g \cos \theta. \quad (\text{II.65})$$

Following Thornton et al. (2006), the volume fraction per unit granular volume is introduced as $\phi^i = \Phi^i / \Phi$ and ensures $\phi^s + \phi^l = 1$. To be in the same framework as Thornton et al. (2006), this notation is employed in the following. Using equation (II.44) and (II.65), the momentum equation (II.64) for small particles is rewritten as follows:

$$\Phi \rho^p \left[\frac{\partial \phi^s w^s}{\partial t} + \frac{\partial \phi^s w^s w^s}{\partial z} \right] = -p^m \frac{\partial \phi^s}{\partial z} + \frac{\rho^p \phi^s \Phi}{t_s} (w^f - w^s) - \frac{\rho^p \Phi}{t_{ls}} (w^s - w^m) + \phi^l \Phi \mathcal{F}_l(\mu) \frac{\partial p^m}{\partial z}. \quad (\text{II.66})$$

Equation (II.66) is made dimensionless using the same scaling as in section II.1.4:

$$\mathbf{U}^k = \sqrt{d_l g} \tilde{\mathbf{U}}^k, \quad z = d_l \tilde{z}, \quad t = \sqrt{d_l/g} \tilde{t}, \quad p^k = \rho^l d_l g \tilde{p}^k \quad \text{and} \quad \tau^k = \rho^l d_l g \tilde{\tau}^k. \quad (\text{II.67})$$

Which gives

$$\frac{\partial \phi^s \tilde{w}^s}{\partial \tilde{t}} + \frac{\partial \phi^s \tilde{w}^s \tilde{w}^s}{\partial \tilde{z}} = -\frac{\tilde{p}^m}{\Phi} \frac{\partial \phi^s}{\partial \tilde{z}} + \phi^s (1 - \Phi)^3 \frac{\sqrt{r}}{St^f} (\tilde{w}^f - \tilde{w}^s) - \frac{(\tilde{w}^s - \tilde{w}^m)}{St^p} + \phi^l \mathcal{F}_l(\mu) \frac{\partial \tilde{p}^m}{\partial \tilde{z}}, \quad (\text{II.68})$$

As shown in section II.1.4, $St^f \gg St^p$ in the bed and the fluid drag force can be neglected. Furthermore, assuming a quasi-steady state and neglecting inertial terms, equation (II.68) can be rewritten as

$$-\frac{\tilde{p}^m}{\Phi} \frac{\partial \phi^s}{\partial \tilde{z}} - \frac{(\tilde{w}^s - \tilde{w}^m)}{St^p} + \phi^l \mathcal{F}_l(\mu) \frac{\partial \tilde{p}^m}{\partial \tilde{z}} = 0, \quad (\text{II.69})$$

Assuming that the vertical flux of small particles compensate the vertical flux of large particles, the vertical velocity of the mixture is $w^m = 0$. Thus, equation (II.69) gives the flux of small particles as

$$\phi^s \tilde{w}^s = -\frac{\phi^s}{\Phi} \tilde{p}^m St^p \frac{\partial \phi^s}{\partial \tilde{z}} + \phi^l \phi^s \mathcal{F}_l(\mu) St^p \frac{\partial \tilde{p}^m}{\partial \tilde{z}}. \quad (\text{II.70})$$

Equation (II.70) is then substituted in the mass conservation equation (II.34) to obtain the following advection-diffusion equation for the percolation of small particles:

$$\frac{\partial \phi^s}{\partial \tilde{t}} + \frac{\partial}{\partial \tilde{z}} (\phi^l \phi^s S_r) = \frac{\partial}{\partial \tilde{z}} (D \frac{\partial \phi^s}{\partial \tilde{z}}), \quad (\text{II.71})$$

with

$$S_r = \mathcal{F}_l(\mu) St^p \frac{\partial \tilde{p}^m}{\partial \tilde{z}} \quad \text{and} \quad D = \frac{\phi^s \tilde{p}^m St^p}{\Phi}, \quad (\text{II.72})$$

Since the pressure gradient is negative, S_r is negative which ensures a downward flux for the small particle phase.

In equation (II.71), S_r is the segregation number or advection coefficient and D is the diffusion coefficient. Here, equation (II.72) provides physical closures, which are directly obtained from volume-averaging of the particle scale segregation forces. The advection coefficient S_r is therefore expressed as a product between the segregation term $\mathcal{F}(\mu) \partial \tilde{p}^m / \partial \tilde{z}$, which quantifies the ability for the small particles to fall downward, and the solid Stokes number which quantifies the drag force exerted by the other grains counteracting this downward movement. It is interesting to note that the granular Stokes number is present in both coefficients which indicates that it is a key parameter for the advection and the diffusive remixing. Equation (II.72) shows that the mixture pressure is also an important parameter for diffusion.

The resolution strategy is based on a conservative Godunov schemes proposed by Chassagne (2020) where a no flux condition is applied at the bottom and on top of the vertical domain. A vertical discretisation of $d\tilde{z} = h/80$ is taken. The time step is computed in order to satisfy the CFL condition, a stability condition ensuring that the fastest wave of the system solved, travel less than the distance $d\tilde{z}$ during the time step. The full details of the algorithm are available in Chassagne (2020).

These results improve upon the original model from Thornton et al. (2006) and Gray and Chugunov (2006) since the advection and the diffusion coefficients are linked to the local physical parameters of the segregation mechanisms. The multi-phase flow model has provided the framework to link the experimentally-based closures (Guillard et al., 2016; Tripathi and Khakhar, 2013) to the more classical advection-diffusion equation. It must be noted that this result not only provides closures for the advection-diffusion model based on local granular forces but also highlights the key local physical mechanisms controlling segregation and diffusion. Finally, it has been shown above that since the fluid does not play an important role in the segregation process, the present results hold for dry granular flows.

In the next section, the proposed multi-phase flow model and advection-diffusion model will be tested against existing discrete numerical simulations that will provide local quantities to assess the predictions of our models.

CHAPITRE III

COMPARISON WITH EXISTING DISCRETE NUMERICAL SIMULATIONS

*It' s just one world, this spine of rock and streams
And snow, and the wash of gravels, silts
Sands, bunchgrasses, saltbrush, bee-fields,
Twenty million human people, downstream, here below.*

Snyder, Gary. ' At Tower Peak.' *Poetry Soup*

In chapter II, a theoretical approach to upscale the granular scale forces into continuum models for vertical size segregation in bedload transport has been presented. The first step consisted in the development of a bidisperse multi-phase flow model that contains the segregation force proposed by Guillard et al. (2016) and the granular drag force proposed by Tripathi and Khakhar (2013). Then, starting from this multi-phase flow model and inspired by Thornton et al. (2006), a vertical advection-diffusion equation for the segregation of small particles into large particles has been developed. This step provided new formulations for the advection coefficient Sr and for the diffusion coefficient D by bridging the gap between the advection-diffusion processes and the underlying granular scale forces at play during segregation.

In chapter II, the approach was purely theoretical and we presented the numerical algorithms to solve the multi-phase flow model and the advection-diffusion equation. As a consequence, in this chapter, it is proposed to assess the numerical results of both models. The models will be evaluated against the discrete numerical simulations of Chassagne et al. (2020b) and thus, the same configuration will be explored. This discrete numerical study focused on the segregation of small particles initially resting on top of large particles in the context of turbulent bedload transport. It provides a comprehensive dataset to evaluate local granular parameters such as the volume fraction and the segregation velocities. In addition, since it is not the purpose of this work to develop a granular rheology, the shear stress and shear rate profiles obtained from this Discrete Element Modeling (DEM) will be used as input parameters for the continuum models.

The 3D DEM configuration and the main results from Chassagne et al. (2020b) are first summarised in section III.1. Then, section III.2 presents the comparison between

the results of the multi-phase flow model and the data from the DEM. In section III.3 the consistency of the advection-diffusion model with the multi-phase flow model is verified. Lastly, the results of both continuum models are discussed and contrasted with the results of Chassagne et al. (2020b).

III.1 DEM investigation of Chassagne et al. (2020b)

The multi-phase flow model will be compared to the discrete simulations of Chassagne et al. (2020b). The configuration explored and the main results of Chassagne et al. (2020b) are briefly presented in this section.

The authors investigated grain-size segregation in turbulent bedload transport using a coupled fluid-Discrete Element Model (DEM) originally developed by Maurin et al. (2015) and used to study bedload rheology (Maurin et al., 2016) and the slope influence (Maurin et al., 2018). For further details, the interested reader is referred to Chassagne et al. (2020b). The 3D bi-periodic DEM set-up consisted in depositing a layer of small particles over large ones, and letting the particles entrained by the fluid flow at a fixed Shields number (see figure III.1d). The latter is the dimensionless fluid bed shear stress $\tau^* = \tau^f / [(\rho^p - \rho^f)gd_l]$ and was taken equal to 0.1. The bed slope was fixed to 10%, which is representative of mountain streams. The size ratio was taken as $r = 1.5$ with small particles of diameter $d_s = 4\text{mm}$ and large particles of diameter $d_l = 6\text{mm}$. The amounts of large and small particles were assimilated to a number of layers, N_l and N_s . The number of layers of a given class represents the height, in terms of particle diameter of this class, occupied by particles if the concentration was equal to the random close packing ($\Phi_{max} = 0.61$). In this way, the bed height at rest was defined as $h = N_l d_l + N_s d_s$ and was fixed to $h = 10d_l$. In the study of Chassagne et al. (2020b), different simulations have been performed with N_s varying from 0.01 (a few isolated particles) to $N_s = 2$. In this section the comparison will be made with $N_s = 1.5$ since it represents the best fit for the dependencies proposed in their work. The bulk response of the granular mixture to this fluid forcing is represented by the dimensionless mixture streamwise velocity profile in figure III.1a. The inset is a semilog plot of the dimensionless velocity profile and shows that it is exponentially decreasing in the bed. As shown in figure III.1b the linearity of the curve in the semilog plot confirms that the shear rate is exponentially decreasing in the quasi-static part of the bed (delimited by the two horizontal black dashed lines). As expected for a uniform flow, the mixture shear stress $\tilde{\tau}_{xz}^m$ shown in figure III.1c is linear with depth. For both quantities, the following fits were proposed and plotted as a red dotted line in figure III.1.

$$\tilde{\gamma}^m = \gamma_0 e^{\tilde{z}/s_0} \quad \text{and} \quad \tilde{\tau}_{xz}^m = a_0 \tilde{z} + \tau_0 \quad (\text{III.1})$$

The simulations performed by Chassagne et al. (2020b) on this configuration focused on the downward segregation of small particles. It was observed that the layer of small particles percolates rapidly for $\tilde{z} > 8.5$ (flowing layer) and then slows down below (see figures III.1b and III.1c). Chassagne et al. (2020b) showed that the small particles are advected downward like a travelling wave into the bed made of large particle with a layer of constant thickness. As figure III.1e shows, the small particle concentration has a Gaussian-like shape and remains self-similar in time while segregating. The center

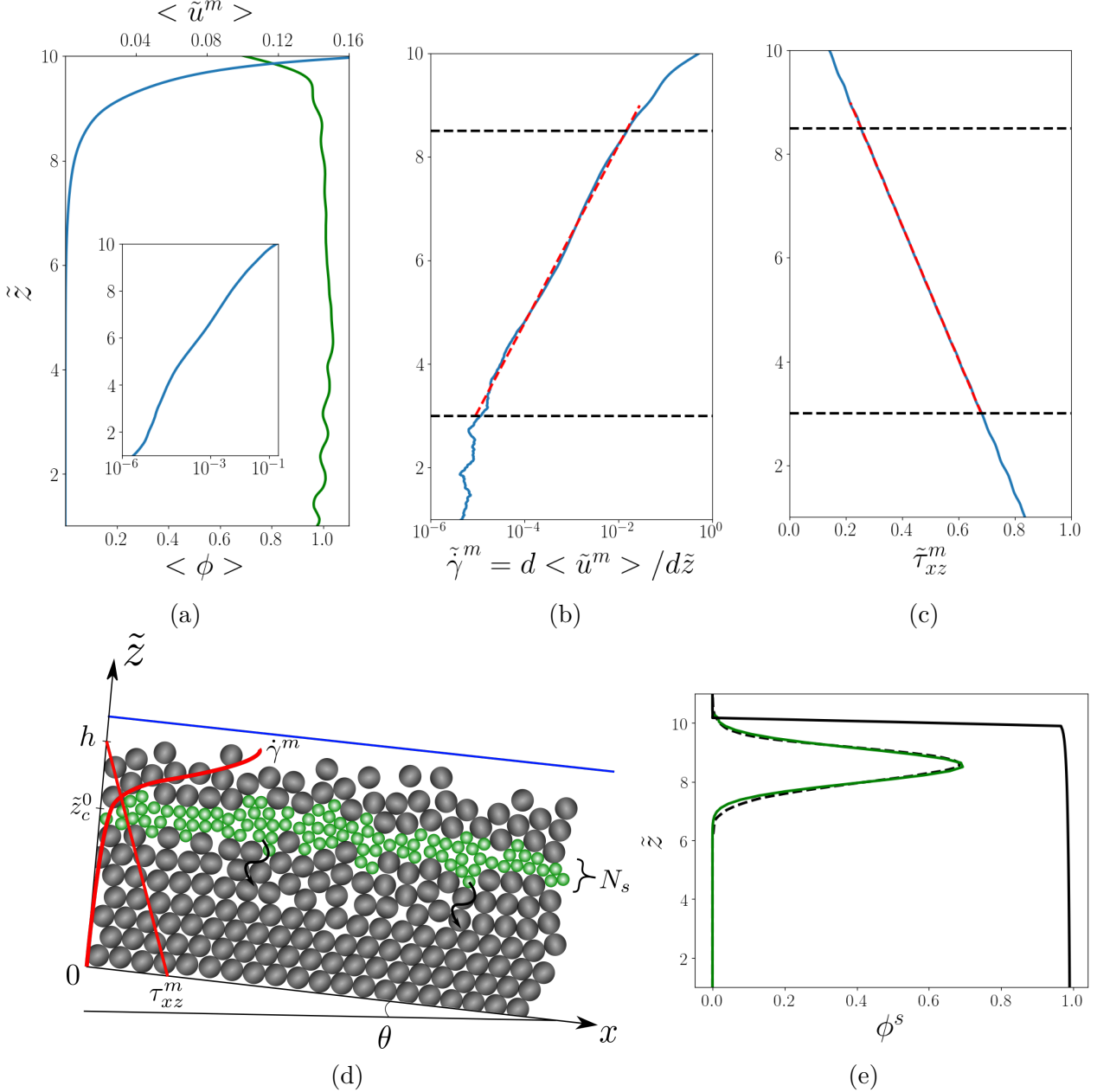


FIG. III.1: Dimensionless profiles and configuration from the DEM simulations. (a) Streamwise mixture velocity profile in the bed (—) and mixture volume fraction (—). The inset is the semilog plot of the velocity profile. (b) Solid shear rate (—) and the corresponding fit ($\tilde{\gamma}^m = \gamma_0 e^{\tilde{z}/s_0}$) with $\gamma_0 = 1.64 \times 10^{-7}$ and $s_0 = 0.74$. (c) Solid shear stress and the corresponding fit ($\tilde{\tau}_{xz}^m = a_0 \tilde{z} + \tau_0$) with $a_0 = -0.078$ and $\tau_0 = 0.91$. The top and lower boundary of the quasi-static bed are represented by -----. (d) Sketch of the numerical experiment with the input profiles for the rheology. (e) Concentration profile of small particles at the initial state for the DEM (----) and its Gaussian fit (—), taken as an input for the multi-phase flow model. The concentration profile, ϕ , of the mixture (—) is also represented.

of mass of small particles, \tilde{z}_c , is therefore representative of the dynamics of the entire layer. Chassagne et al. (2020b) observed that the small particle layer travels down as a logarithmic function of time:

$$\tilde{z}_c(t) = -a_1 \ln \tilde{t} + b, \quad (\text{III.2})$$

where a_1 is a constant characterising the segregation velocity ($d\tilde{z}_c(t)/d\tilde{t} = -a_1/\tilde{t}$). The authors demonstrated that this logarithmic descent of small particles is a consequence of the dependency of the segregation velocity on the inertial number as

$$\frac{d\tilde{z}_c}{dt} \propto I^{0.85}(\tilde{z}_c). \quad (\text{III.3})$$

Using equation (III.3) in the framework of the advection-diffusion model of Thornton et al. (2006) and Gray and Chugunov (2006) (see equation I.5) it was shown that the advection coefficient could be written as

$$S_r = S_{r0} I^{0.85}, \quad (\text{III.4})$$

where $S_{r0} = 0.049$, extending the inertial number dependency found by Fry et al. (2018) to bi-disperse size segregation in the quasi static regime. Then, with the help of a travelling wave method, they evidenced that the small particles percolate as a layer and with a self-similar concentration profile because the ratio between the advection coefficient and the diffusion coefficient is constant. They therefore showed that the Péclet number:

$$Pe = \frac{S_r}{D}, \quad (\text{III.5})$$

is constant with \tilde{z} so that the diffusion coefficient has to have the same dependency on the inertial number as the segregation coefficient:

$$D = D_0 I^{0.85}, \quad (\text{III.6})$$

where D_0 is taken as $D_0 = 0.01$ and should be pressure independent (Fry et al., 2019).

This work also demonstrated that the dynamics of the fine particle layer is controlled by its bottom position, which acts as a lower bound for the segregation velocity. In this way, the particles in the layer cannot segregate faster.

As mentioned in section II.2.3, the rheological parameters for our simulations are imported from the DEM results. The friction coefficient is therefore computed using the definition:

$$\mu = \frac{|\tau_{xz}^m|}{p^m}. \quad (\text{III.7})$$

Similarly, the granular viscosity is computed using the definition:

$$\eta^p = \frac{|\tau_{xz}^m|}{|\dot{\gamma}_{xz}^m|}. \quad (\text{III.8})$$

As shown by the red dashed lines in figures III.1b and III.1c, the fits presented in equation III.1 match the DEM results in the region $8.5 > \tilde{z} > 3$. Thus, using these expressions in eq (III.8) provides an accurate estimate of the granular viscosity for

the particle-particle drag closure. For this reason, the validation of the multi-phase flow model will only be carried out in this part of the bed. Therefore, the initial state consists in placing the small particles in the upper limit of the quasi-static part with the center of mass $\tilde{z}_c^0 = 8.5$. The sketch of this configuration is shown in figure III.1d. Figure III.1e shows the small particle concentration profile of this numerical set-up at the initial state. The initial concentration is taken with a gaussian fit on the DEM initial concentration (figure III.1e), and ensures that the mass of particles is the same in the DEM and in the continuum simulations.

III.2 Validation of the multi-phase flow model

In this section, the theoretical multi-phase flow model proposed in section II.2 is assessed against the discrete simulations of Chassagne et al. (2020b) presented in the previous section. In order to do so, the same configuration as Chassagne et al. (2020b) has to be solved. A continuum layer of width N_s (width of the layer in term of small particle diameter), representing the small particle phase, is deposited as depicted in figure III.1e, among the large particle and the fluid phases. The whole mixture is sheared and segregation should occur.

The system of partial differential equations (II.34)-(II.37) is solved numerically (see section II.2.4). The configuration is shown in figure III.1d with the initial concentration profile of figure III.1e. In these equations, the empirical segregation function is $\mathcal{F}_l(\mu) = 1 - \exp(-70(\mu - \mu_c))$ (see equation (II.13)) and the drag coefficient c is equal to 3 as suggested by Tripathi and Khakhar (2013).

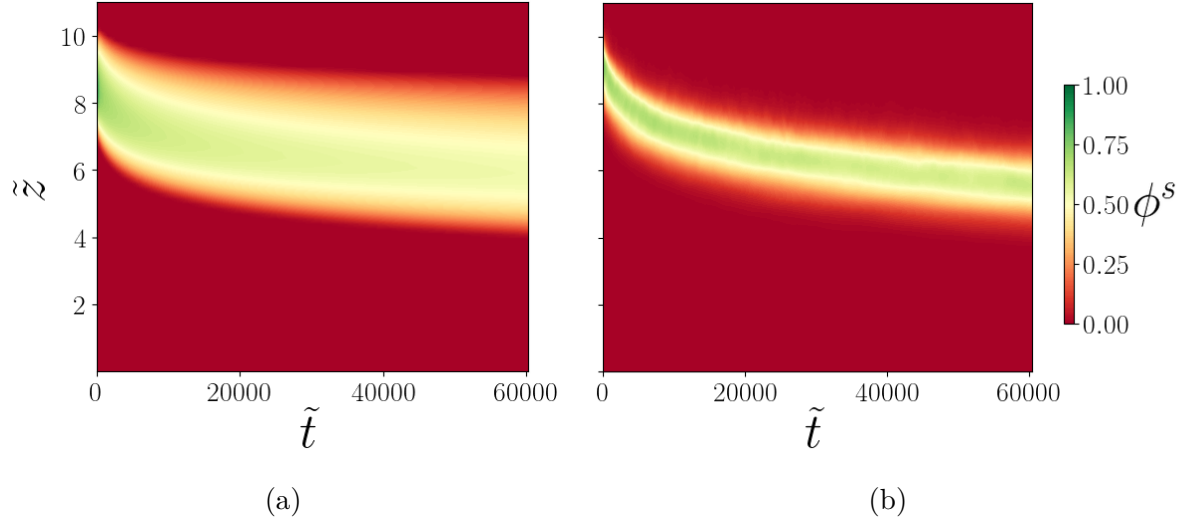


FIG. III.2: Spatio-temporal plot of the small particle concentration in the bed obtained with (a) the multi phase model, (b) the DEM simulation.

Figure III.2 shows the results of the spatio-temporal evolution of the small particle concentration for the multi-phase flow model (figure III.2a) and for the DEM (figure III.2b). This means that for each time step in the x axis, the concentration of small

particles ϕ^s with depth is represented. The red color means that $\phi^s = 0$, i.e. there is only large particles, and the greener it appears, the more ϕ^s tends to one, i.e. there is no large particles. First, it can be seen that the dynamics predicted by the multi-phase flow model is similar to the DEM. The position of the bottom of the layer is about the same in both cases. More quantitatively, the center of mass \tilde{z}_c of the small particle layer as a function of time is compared with the DEM in figure III.3a.

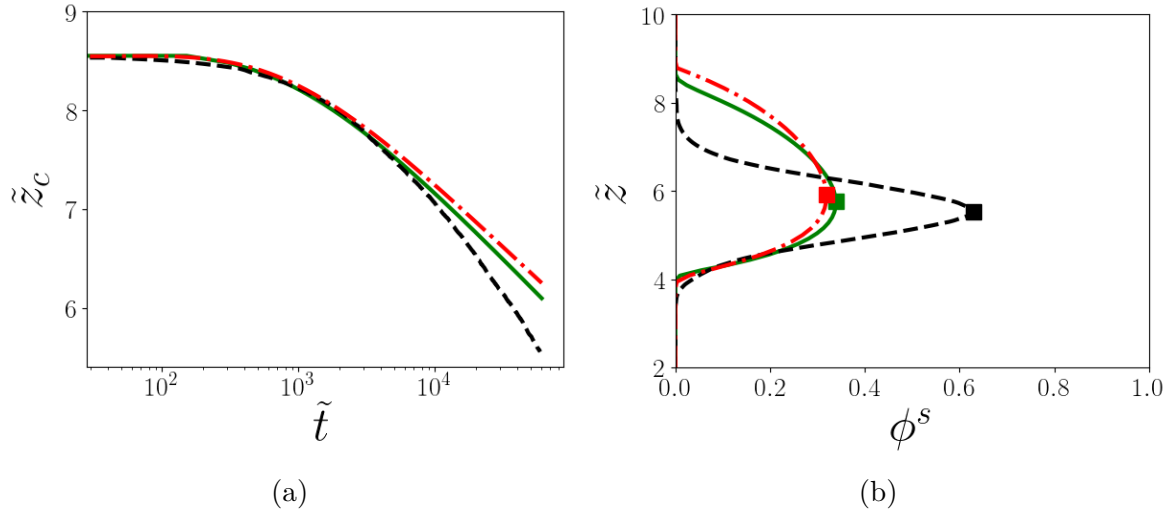


FIG. III.3: Results of the simulation for the multi-phase flow model (---), the advection-diffusion model of (II.71) (—) and the DEM (----). (a) Temporal evolution of the center of mass. (b) Concentration profiles of small particles at the end of the simulation ($\tilde{t} \simeq 60000$). ■ represents the maximum concentration of the profiles.

After a first transient phase ($\tilde{t} > 1 \times 10^3$), the center of mass position is linear in the semilog plot, indicating that the logarithmic descent observed in the DEM simulation is well reproduced by the multi-phase flow model. The slope of the curve, representing coefficient a_1 of equation (III.2) is 0.68 in the DEM simulation and 0.49 for the multi-phase flow model, corresponding to an error of 28%. In addition, figure III.3b shows that in both models, the bottom of the layer is positioned at the same depth indicating that the multi-phase model reproduces well the bottom controlled behaviour observed by Chassagne et al. (2020b) with DEM simulations. However the Gaussian-like profile is not reproduced by the multi-phase flow model and a wider profile is obtained. In figure III.2a the maximum concentration $\max(\phi^s)$ (indicated by ■ in figure III.3b) is almost two times smaller than the one predicted by the DEM simulation, while the extent of the small particle layer is much larger. These results indicate that, with the current parametrisation, the multi-phase flow model is relevant to qualitatively predict segregation dynamics but the error on the segregation velocity and the discrepancies on the concentration profile clearly show that the model needs to be improved.

III.3 Evaluation of the advection-diffusion model

The advection-diffusion equation (II.71) for the segregation of small particles has been derived based upon the multi-phase flow model. In this section, we are interested to see if this model is consistent with the multi-phase flow model. If both models are consistent, the first conclusion is that the advection-diffusion model can be used instead of the multi-phase flow model. Secondly, this also means that the discrepancies observed for the multi-phase flow model are not linked to the numerical scheme but to missing dependencies in the forces used to develop the multi-phase flow model.

The numerical solution at time $\tilde{t} = 60000$ is plotted in figure III.3. Both the center of mass (figure III.3a) and the concentration profile (figure III.3b) are almost superimposed with the multi-phase flow model solution, only slightly differing by numerical diffusion. Therefore, both models can be considered as equivalent, meaning that the physical behaviour of the segregation forces added in the momentum equation of the small particles is accurately predicted by the single advection and diffusion coefficients of equation (II.71). Moreover, when deriving the advection-diffusion equation, it was assumed that the mixture volume fraction $\Phi = \text{cste}$, that the vertical acceleration of the small particles, the vertical mixture velocity and that the fluid drag were negligible. The segregation problem can thus be simply viewed as a competition between the advection coefficient S_r and the diffusion coefficient D of small particles. It should be noted that the interplay between both coefficients has been explored in more details by [Fan et al. \(2014b\)](#).

When comparing the computation time between the multi-phase flow model and the advection-diffusion model derived in section II.3, the obtained speed-up is of one thousand. This represents an important step in the upscaling since the behaviour of small particles can be predicted by a simpler advection-diffusion equation compared with the entire multi-phase flow model. From a numerical perspectives this represents a significant change of scale in the resolution time.

III.4 Discussion

The multi-phase flow model and the associated advection-diffusion model are able to reproduce qualitatively the DEM simulations and the main properties of segregation in turbulent bedload transport obtained by [Chassagne et al. \(2020b\)](#) (bottom controlled segregation, logarithmic descent of the small particles). However, the segregation velocity is lower than predicted by the DEM simulations and the concentration of small particles among large particles is lower than obtained with the DEM.

From the advection-diffusion equation, segregation can be seen as a phenomenon driven by a vertical advection coefficient and a diffusion coefficient. From this analysis, it is necessary to investigate the potential sources of discrepancies in these coefficients.

The vertical advection coefficient S_r and the diffusion coefficient D have been expressed as:

$$S_r = \mathcal{F}_l(\mu) St^p \frac{\partial \tilde{p}^m}{\partial \tilde{z}} \quad \text{and} \quad D = \frac{\phi^s \tilde{p}^m St^p}{\Phi}. \quad (\text{III.9})$$

where $\mathcal{F}_l(\mu)$ comes from the segregation force of Guillard et al. (2016) and the granular Stokes number $St^p = \rho^p d_l \mathcal{W} / 6c\eta^p$ arises from the granular drag force. Guillard et al. (2016) measured numerically the segregation force for a single intruder in a 2D configuration and Tripathi and Khakhar (2013) developed their study in the context of density driven segregation. These configurations are not general and the drag coefficient c as well as the empirical segregation function $\mathcal{F}_l(\mu)$ could vary in our bedload configuration with spheres. In addition, when considering more than one large particle, it could exist some collaborative effects between the large particles (on the model of the hindrance effect for the suspension of particles into a fluid) that are not taken into account in the forces we used. Therefore, in section III.4.1, a sensitivity analysis to the empirical segregation function is presented. Then, in section III.4.2, new formulations of the empirical segregation function $\mathcal{F}_l(\mu)$ and of the drag coefficient c will be proposed based on the DEM results.

As the advection-diffusion equation results are similar to the multi-phase flow model results, the discussion and the associated simulations will only be performed with the advection-diffusion model.

III.4.1 Investigation of the empirical segregation function \mathcal{F}_l

Numerical data from Guillard et al. (2016) for the empirical segregation function $\mathcal{F}_l(\mu)$ exhibit a significant scatter and on figure II.2 one could suggest that a constant function could also fit the data. In addition, this function appears in the advection coefficient $S_r = \mathcal{F}_l(\mu) St^p \partial \tilde{p}^m / \partial z$ and varying its magnitude could highlight its impact on the advection coefficient and thus on the discrepancies observed when compared with the DEM. In this section, an analysis of the sensitivity to the empirical segregation function, taken as constant and varying from $\mathcal{F}_l = 1$ to $\mathcal{F}_l = 15$, is presented.

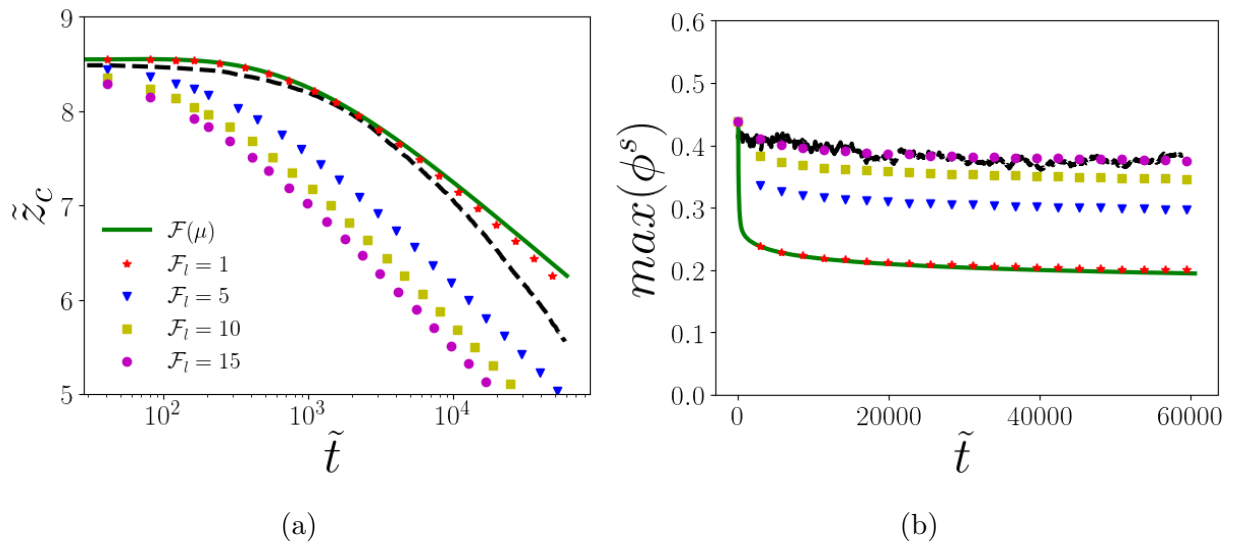


FIG. III.4: Comparison with the DEM (----) for various values of $\mathcal{F}_l = cste$ for the temporal evolution of (a) the center of mass and (b) the maximum concentration of ϕ^s .

Figure III.4a shows the temporal evolution of the small particle center of mass for the different values of the empirical segregation function \mathcal{F}_l . The linear evolution in

the semi-logarithmic plot is conserved with the same slope (coefficient a_1 in equation III.2), whatever the value of the empirical segregation function, meaning that the segregation velocity $d\tilde{z}_c/d\tilde{t}$ is not modified when changing the intensity of the empirical segregation function. Increasing \mathcal{F}_l only makes the curves shift vertically which means that at the beginning of the experiment, in the upper layers of the bed, the center of mass sink more or less rapidly following the value of \mathcal{F}_l . Figure III.4b shows that the maximum concentration is better predicted when increasing the empirical segregation function. When reaching $\mathcal{F}_l = 15$, agreement with DEM results is perfect. The previous simulation, where the empirical segregation function \mathcal{F}_l is a function of the friction coefficient μ , is also plotted in these figures. It is interesting to note that simulation with $\mathcal{F}_l = 1$ is almost superimposed with the one obtained with $\mathcal{F}_l(\mu)$. These observations tend to show that the friction coefficient dependency has a small influence on the size segregation configuration investigated. Therefore, taking \mathcal{F}_l as constant is a good approximation, at first order.

[Chassagne et al. \(2020b\)](#) showed that the advection coefficient S_r is a function of the inertial number I (see equation III.4) and linked the logarithmic descent to the exponential form of I in S_r . In the proposed model, the advection coefficient reads

$$S_r = \mathcal{F}_l St^p \frac{\partial \tilde{p}^m}{\partial \tilde{z}} \quad (\text{III.10})$$

In this coefficient, since the solid pressure gradient is constant in the bed (equation II.65) and $\mathcal{F}_l = cste$, there is only one non-constant variable which is the inverse of the granular viscosity $1/\eta^p$ appearing in the granular Stokes number (equation II.23). As figure III.4a shows that the logarithmic descent is still preserved with this parametrisation, it demonstrates that the viscosity profile is mainly responsible for the logarithmic descent. Therefore, in the proposed advection coefficient S_r , the empirical segregation function \mathcal{F}_l controls the strength of the segregation force and can be seen as a forcing parameter. In contrast, the velocity at which the small grains are descending is controlled by the granular viscosity in the granular Stokes number St^p . In this way, the segregation problem can simply be seen as the settling of small particles under a force proportional to the empirical segregation function \mathcal{F}_l , into a complex fluid having a variable granular viscosity.

It should be noted that there is a direct relation between the dimensionless granular viscosity and the inertial number. Indeed, the inertial number of large particles is

$$I = \frac{\dot{\gamma}^m d_l}{\sqrt{p^m / \rho^p}}. \quad (\text{III.11})$$

Considering that

$$\eta^p = \frac{|\tau_{xz}^m|}{|\dot{\gamma}^m|} \quad \text{and} \quad \tau_{xz}^m = \mu p^m, \quad (\text{III.12})$$

the inertial number can be written as

$$I = \frac{\mu d_l \sqrt{p^m \rho^p}}{\eta^p}. \quad (\text{III.13})$$

Then, making η^p dimensionless with the scaling $\rho^p d_l \mathcal{W}$, one can obtain

$$I = \frac{\mu \sqrt{\tilde{p}^m}}{\tilde{\eta}^p}, \quad (\text{III.14})$$

where $\tilde{\eta}^p = \eta^p / \rho^p d_l \mathcal{W}$ is the dimensionless granular viscosity and $\mu = |\tilde{\tau}_{xz}^m| / \tilde{p}^m$ is the friction coefficient. Since the variation of μ and $\sqrt{\tilde{p}^m}$ is small compared with the exponential profile of $\tilde{\eta}^p$, the inversely proportional relation between the granular viscosity and the inertial number shows that the inertial number dependency found by Chassagne et al. (2020b) could be an effect of the granular viscosity.

Figure III.4b showed that a better maximum concentration was predicted with $\mathcal{F}_l = 15$. The Péclet number is defined as the ratio between the advection coefficient and the diffusion coefficient as $Pe = S_r/D$. Since the function \mathcal{F}_l is in the advection coefficient S_r , increasing \mathcal{F}_l increases the Péclet number and as a result soften the effect of diffusion. This explain the origin of the better concentration profile with the increase of \mathcal{F}_l . However, when increasing \mathcal{F}_l , we get away from the accurate advection (see figure III.4a). The conclusion is that with $\mathcal{F}_l = 1$, which in terms of magnitude corresponds to $\mathcal{F}_l(\mu)$, the advection coefficient is correct but the Péclet number is not. The discrepancies have to come from the diffusion coefficient.

The advection coefficient S_r and the diffusion coefficient D have been plotted in figures III.5a and III.5b with $\mathcal{F}_l = 1$, for $\phi^s = \max(\phi^s)$. For $\tilde{z} > 7$, S_r is close to the values predicted by the DEM. Under this limit, both curves are exponentially decreasing into the bed but with a different slope leading to discrepancies. Another dependency with depth is thus probably missing in the empirical segregation function or in the drag coefficient c to find again a similar slope to the DEM. The proposed diffusion coefficient has the same slope as the one predicted by the DEM, which means that it contains the correct depth dependency and the accurate tendencies. However, its value is too high by a factor ten, explaining why the advection-diffusion results are too diffusive.

III.4.2 Missing dependencies in the particle-scale forces

The analysis on the advection and diffusion coefficients has shown that dependencies were missing in these coefficients obtained from granular scale forces. The segregation and solid drag forces of Guillard et al. (2016) and Tripathi and Khakhar (2013) have been established in idealised granular segregation configurations (e.g. unique intruder, simple forcing, 2D DEM) so that one can expect the two formulations to miss some dependencies when considering more general cases (mixture of small and large particles, 3D modelling or complex forcing). Such dependencies probably lie in the drag coefficient c and the empirical segregation function \mathcal{F}_l contained in the advection and diffusion coefficients. While the drag coefficient c was taken constant in their study, Tripathi and Khakhar (2013) and Duan et al. (2020) suggested that it could depend on the local concentration of particles. Similarly to an hindrance function in a fluid flow, one indeed expects an increase of the effective solid drag force on a particle with increasing concentration. This dependency of the drag coefficient in the local particle concentration should also impact the diffusion coefficient profile (see figure III.5b) and makes it possible to match the DEM. In addition, to correct the slope of the advection coefficient S_r (see figure III.5a), only the empirical segregation function \mathcal{F}_l should vary

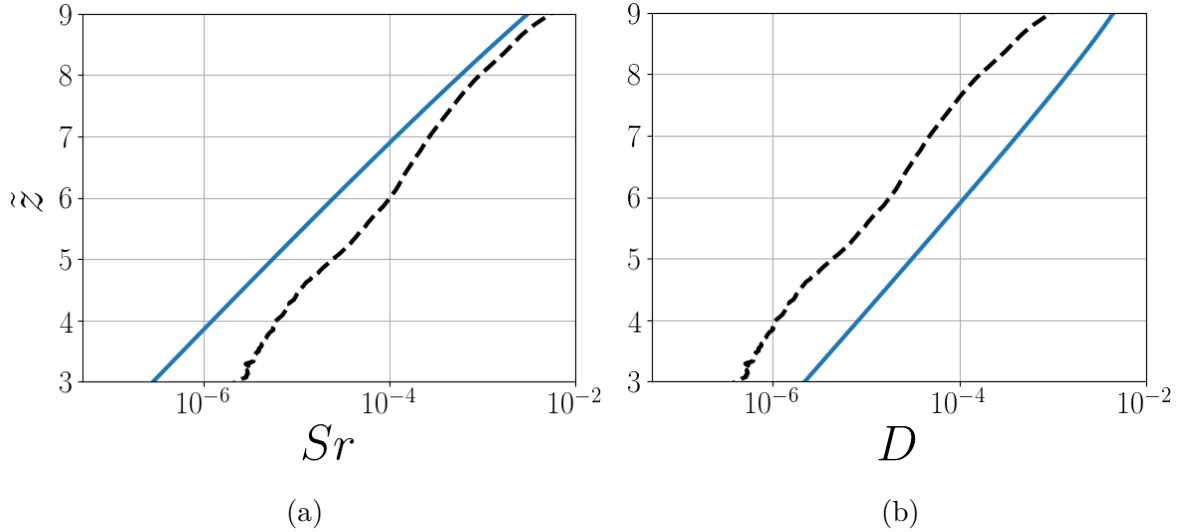


FIG. III.5: (a) Advection coefficient in the bed (equation II.71) with $\mathcal{F}_l = 1$, for $N_s = 1.5$ (—) and $S_{r0}I^{0.85}$ proposed by Chassagne et al. (2020b) (---). (b) Diffusion coefficient in the bed from equation (II.71) for $\phi^s = \max(\phi^s)$ for the case $N_s = 1.5$ (—) and $D_0I^{0.85}$ proposed by Chassagne et al. (2020b) (---).

with depth.

As detailed in section III.1, Chassagne et al. (2020b) have been able to express the advection and diffusion coefficients dependencies on the inertial number I (see equations III.4 and III.6). In the following, both DEM and advection-diffusion coefficients are compared so as to extract the potential missing dependencies of \mathcal{F}_l and c from the DEM coefficients and to propose new formulations of these parameters. Then, it is verified that the results from the advection-diffusion model are consistent when using these proposed closures.

Inertial number dependency in the advection and diffusion coefficients

In order to compare the advection and diffusion coefficients with the one of the DEM and to find the missing dependencies, it is first shown that the coefficients of equation (II.72) can be expressed with an inertial number dependency, like it was found with the DEM results. Indeed, as already shown in equation (III.14), the granular Stokes number can be rewritten as a function of the inertial number I :

$$St^p = \frac{I}{6c\mu\sqrt{\tilde{p}^m}}. \quad (\text{III.15})$$

With this alternative definition, the advection and diffusion coefficients obtained in equation (II.72) can be rewritten as a function of the inertial number I :

$$S_r = \frac{I\mathcal{F}_l}{6c\mu\sqrt{\tilde{p}^m}} \frac{\partial\tilde{p}^m}{\partial\tilde{z}} \quad \text{and} \quad D = \frac{\phi^s\sqrt{\tilde{p}^m}I}{\Phi 6c\mu}. \quad (\text{III.16})$$

One can notice that $\sqrt{\tilde{p}^m}I = \tilde{\gamma}$, which makes the diffusion coefficient directly proportional to the shear rate. Such a dependency for the diffusion coefficient was found with

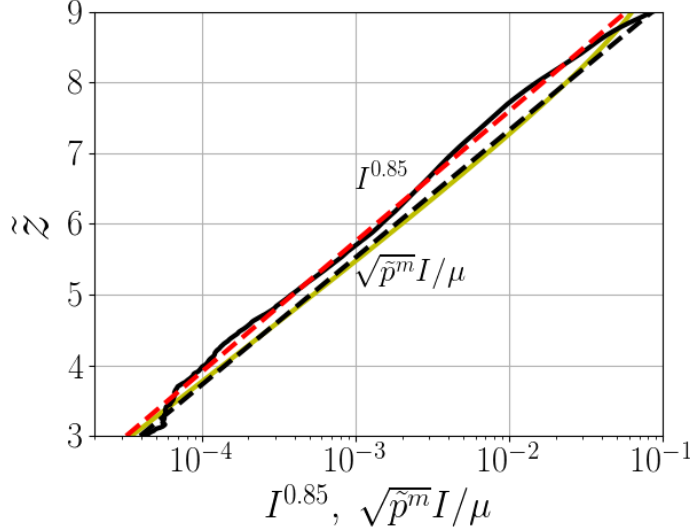


FIG. III.6: $I^{0.85}$ computed from DEM results (—) and its exponential fit $I'_0 e^{\tilde{z}/s_2}$ (---) compared with $\sqrt{\tilde{p}^m}I/\mu$ (—) and its exponential fit $D'_0 e^{\tilde{z}/s_3}$ (----). $I'_0 = 7.52 \times 10^{-7}$, $s_2 = 0.8$, $D'_0 = 8.46 \times 10^{-7}$ and $s_3 = 0.78$.

a dry bidisperse configuration by Cai et al. (2019) and Fry et al. (2019) with DEM simulations. This shows that the particle-particle force based model is able to explain a dependency found in different experiments. It represents a strong argument to show the robustness of the proposed model. Yet, the power 0.85 highlighted by the DEM does not seem to appear. In figure III.6 the data from the DEM of Chassagne et al. (2020b) have been used to plot the profiles of $\sqrt{\tilde{p}^m}I/\mu$ and $I^{0.85}$. In the same figure, the fit on each of these profiles is also proposed. These fits are of the form

$$I^{0.85} = I'_0 e^{\tilde{z}/s_2} \quad \text{and} \quad \sqrt{\tilde{p}^m}I/\mu = D'_0 e^{\tilde{z}/s_3}. \quad (\text{III.17})$$

One can observe that values only differ by a factor $D'_0/I'_0 = 1.13$ and that the exponential evolution with depth is the same, which proves that in this case

$$\frac{\sqrt{\tilde{p}^m}I}{\mu} \propto I^{0.85}. \quad (\text{III.18})$$

Such a result shows that the diffusion coefficient of the proposed model (equation III.16) has the same dependency with $I^{0.85}$ as the diffusion coefficient proposed by Chassagne et al. (2020b). This explains the identical evolution with depth between both coefficients in figure III.5b, and shows that the advection equation and the multi-phase flow model are physically consistent.

New formulation of the drag coefficient

Assuming that the drag coefficient includes the accurate dependencies, the following equality should be obtained between the diffusion coefficients of the DEM and the one proposed in equation (III.16):

$$\frac{\phi^s \sqrt{\tilde{p}^m}I}{\Phi 6c\mu} = D_0 I^{0.85} \quad (\text{III.19})$$

which means that the drag coefficient verifies

$$c = \frac{\phi^s \sqrt{\tilde{p}^m} I}{\Phi 6\mu D_0 I^{0.85}} \quad (\text{III.20})$$

From the figure III.6, the following fits are obtained

$$\frac{\sqrt{\tilde{p}^m} I}{\mu} = D'_0 e^{\tilde{z}/s_3} \quad \text{with} \quad D'_0 = 8.46 \times 10^{-7} \quad s_3 = 0.78 \quad (\text{III.21})$$

$$I^{0.85} = I'_0 e^{\tilde{z}/s_2} \quad \text{with} \quad I'_0 = 7.52 \times 10^{-7} \quad s_2 = 0.8. \quad (\text{III.22})$$

Dividing (III.21) by (III.22) one obtains

$$\frac{\sqrt{\tilde{p}^m} I}{\mu I^{0.85}} = \frac{D'_0}{I'_0} = C_0, \quad (\text{III.23})$$

where $C_0 = 1.13$ is a constant. In this way, equation (III.20) becomes

$$c(\phi^s) = \frac{C_0}{6\Phi D_0} \phi^s = 31\phi^s. \quad (\text{III.24})$$

As a consequence of this linear scaling with concentration, the dependency on the small particle volume fraction vanishes in the diffusion coefficient (equation II.72). This modification will tend to smooth out the small particle concentration profile. In this drag coefficient, when $\phi^s \rightarrow 0$ (i.e. one small particle in a bath of large particles), the drag coefficient vanishes while it should reach a constant value, $c = 3$ as shown by Tripathi and Khakhar (2013). To ensure a consistent formulation, it is therefore proposed $c(\phi^s)$ to read

$$c(\phi^s) = 3 \left(1 + \frac{28}{3} \phi^s \right), \quad (\text{III.25})$$

which tends to 3 when $\phi^s \rightarrow 0$ and to 31 when $\phi^s \rightarrow 1$.

New formulation of the empirical segregation function \mathcal{F}_l

As mentioned in the last section, the empirical segregation function \mathcal{F}_l is expected to depend on depth (see figure III.5a). In this way, the advection coefficient should correspond to the DEM and it follows

$$\frac{I\mathcal{F}_l}{6c(\phi^s)\mu\sqrt{\tilde{p}^m}} \left| \frac{\partial \tilde{p}^m}{\partial \tilde{z}} \right| = S_{r0} I^{0.85}. \quad (\text{III.26})$$

From this equation and using (III.18), one can express the empirical segregation function, for $\rho^p \neq \rho^f$, as

$$\mathcal{F}_l(\tilde{p}^m, \phi^s) = \mathcal{F}_0 c(\phi^s) \tilde{p}^m, \quad (\text{III.27})$$

where $\mathcal{F}_0 = 6S_{r0}\rho^p / (C_0\Phi(\rho^p - \rho^f))$. This result is the consequence of the scaling obtained for the advection coefficient in the DEM simulation. In the latter, only the local solid volume fraction ϕ^s and the pressure \tilde{p}^m are varying. Other dependencies can therefore be contained in S_{r0} and should not be interpreted. Focusing on the meaningful

terms, the empirical segregation function is logically found to depend on the small particle concentration, as expected when considering a mixture of particles. The pressure dependency suggests that the segregation function could depend on the stress state and that the local pressure could drive the lift force. [Guillard et al. \(2014\)](#) found the lift force to increase with depth until a saturation depth where this force becomes constant. The pressure dependency found in equation (III.27) could explain the increasing lift force with depth and imply that in the studied configuration the saturation depth is not reached.

III.4.3 Consistency of the model with the new formulations

With the new formulations of the solid drag coefficient $c(\phi^s)$ and the empirical segregation function $\mathcal{F}_l(\tilde{p}^m, \phi^s)$, it is verified that the DEM results can be reproduced. This is done with simulations accounting for different initial quantities of small particles ($N_s = 0.5, 1, 1.5, 2$).

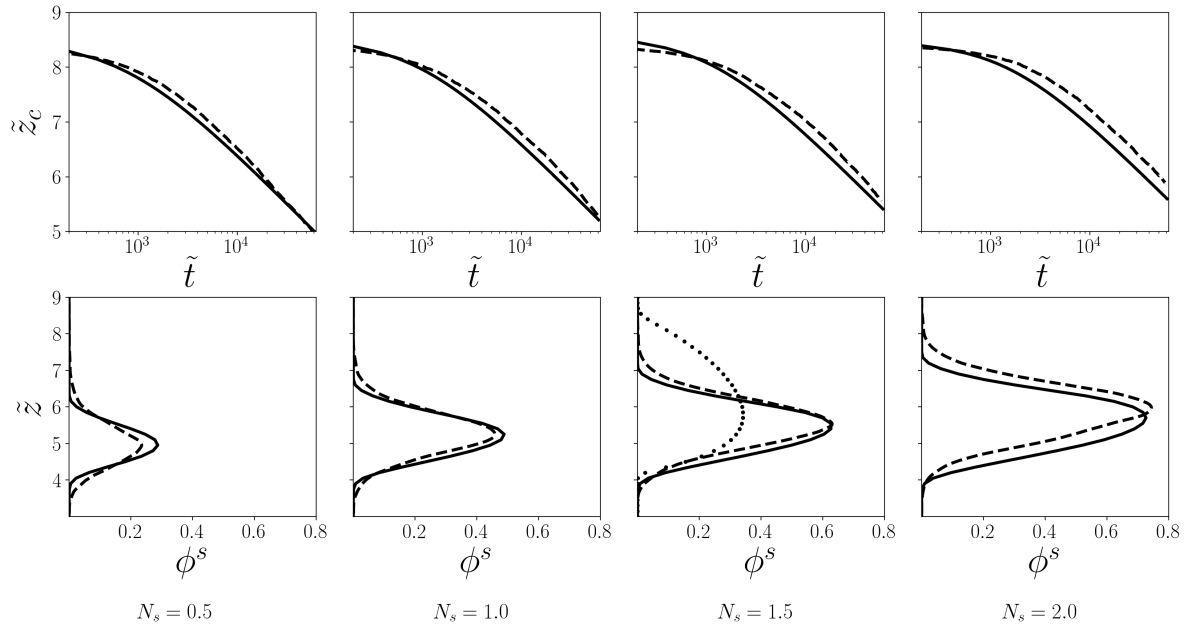


FIG. III.7: Upper part of the panel: temporal evolution of the center of mass for $N_s = 0.5, 1, 1.5, 2$. Lower part of the panel: final small particle concentration profile for $N_s = 0.5, 1, 1.5, 2$. ----- are the DEM results from [Chassagne et al. \(2020b\)](#). The concentration profile obtained without any parametrisation, in the case $N_s = 1.5$ (from figure III.3b), has also been plotted (.....).

Figure III.7 shows the results for the time evolution of the center of mass and the final concentration profile. Both the mass centers and the final concentration profiles are fairly well superimposed with the DEM results. Therefore, the new parametrisation is consistent with the DEM simulations. The concentration profile with the original parametrisations of c and $\mathcal{F}_l(\mu)$ (see figure III.3b) has also been plotted in figure III.7 ($N_s = 1.5$). The shape of the final concentration profile has drastically changed, from a bell-shape to the expected Gaussian-like shape. This is attributed to the small particle

concentration dependency in the drag coefficient, which cancels the original concentration dependency in the diffusion coefficient.

Lastly, note that changing the parametrisation of the forces still yields physical solutions which proves that the advection-diffusion model and the corresponding multi-phase flow model are physically consistent and robust.

III.4.4 Influence of the size ratio

[Guillard et al. \(2016\)](#) and [Jing et al. \(2020\)](#) showed that the segregation force depends on the size ratio $r = d_l/d_s$ and exhibits a maximum for a size ratio of $r = 2$. [Schlick et al. \(2015\)](#) found the segregation velocity of an ensemble of small particles to be dependent with the logarithm of the size ratio for $r < 3$ and also found the segregation velocity to reach its maximum for $r \sim 2$. Based on DEM simulations, [Chassagne et al. \(2020b\)](#) also studied the size-ratio dependency. Surprisingly, it was found that the segregation velocity of the percolating small particles was a monotonic increasing function of r . Best fit of the DEM results suggested the following dependency $f(r) = 0.45(e^{(r-1)/1.59} - 1)$ for the advection coefficient S_r . Further studies on the effect of the size ratio on segregation is needed to explain the differences with the studies of [Golick and Daniels \(2009\)](#), [Schlick et al. \(2015\)](#) and [Guillard et al. \(2016\)](#). A potential reason could lie in the difference of configuration. For example, it could shift the value of the maximum segregation efficiency to higher values of r that have not been investigated by [Chassagne et al. \(2020b\)](#).

This dependency is introduced into the empirical segregation function \mathcal{F}_l as

$$\mathcal{F}_l(\tilde{p}^m, \phi^s, r) = \mathcal{F}_0 f(r) c(\phi^s) \tilde{p}^m. \quad (\text{III.28})$$

Using this parametrisation, simulations have been performed for $r = 1.25, 1.5, 1.75, 2, 2.25$. The results are plotted in figure [III.8](#) and compared with DEM simulations.

For each case, the center of mass position is in very good agreement with the DEM simulations. For the lower size ratio, the concentration profiles are superimposed with the DEM results while for the higher size ratios ($r = 2$ and $r = 2.25$) the maximum concentrations are slightly higher than the DEM. This indicates that the model is not diffusive enough. Indeed, the size ratio dependency has only been introduced in the advection coefficient. As shown in section [III.4.1](#), the shape of the concentration profile results from a subtle balance between advection and diffusion through the Péclet number Pe . For the highest size ratio, this balance is not perfectly reproduced by the proposed model, which indicates that the diffusion coefficient should also depend on the size ratio. This would imply that the granular Stokes number also depends on the size ratio. It could explain why [Guillard et al. \(2016\)](#) found a maximum segregation force for a size ratio $r = 2$, while [Chassagne et al. \(2020b\)](#) found the advection coefficient S_r to increase exponentially with the size ratio. Further research is needed to elucidate this point through a detailed investigation of the granular Stokes number dependency to the size ratio.

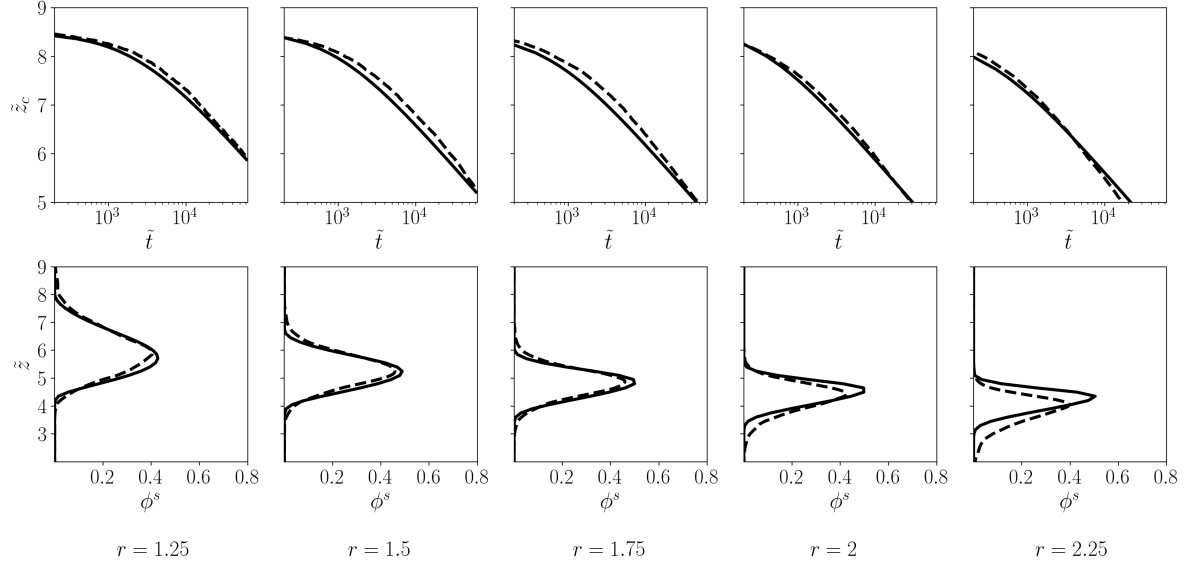


FIG. III.8: Upper part of the panel: temporal evolution of the center of mass for $N_s = 1$ and $r = 1.25, 1.5, 1.75, 2, 2.25$. Lower part of the panel: final small particle concentration profile for $N_s = 1$ and $r = 1.25, 1.5, 1.75, 2, 2.25$. In these figures, — corresponds to the advection-diffusion model and - - - are the DEM results from [Chassagne et al. \(2020b\)](#).

III.5 Conclusion

The analysis of the simulation results through the advection and diffusion coefficients made it possible to identify the origins of the discrepancies with the DEM and to propose new formulation for the parameters of the particle scale forces proposed by [Guillard et al. \(2016\)](#) and [Tripathi and Khakhar \(2013\)](#).

From this development, it appears that the comprehension and the modeling of the segregation forces at the particle scale is essential to derive larger scale models. Then, multi-phase flow models provide the key step for the upscaling process as they allow one to bridge the gap between the comprehension at the particle scale and the advection and diffusion framework acting at larger scale. As our analysis showed, the forces proposed by [Tripathi and Khakhar \(2013\)](#) and [Guillard et al. \(2016\)](#) could miss some dependencies when considering more general configuration or a collection of particles. Supplementary experiments should be carried out to improve this formulation and provide dependencies that are more physically based than the one we proposed by fitting the DEM results. In this idea, [Jing et al. \(2020\)](#) proposed a force depending on the pressure gradient, like [Guillard et al. \(2016\)](#), and proposed an empirical function that depends on the size ratio. However, this empirical function has no dependency on the concentration, the pressure and the shear rate. It would be of great interest to propose a formulation that includes all the rheological and size dependencies.

Lastly, [Van der Vaart et al. \(2018\)](#) proposed a lift force for an intruder in a bed of small particles, having the same form as a Saffman force. It would be interesting to replace the lift force of [Guillard et al. \(2016\)](#) in our model by this Saffman force. First this lift force could be assessed against the DEM results. Secondly, it would allow one to see if this force provides the $I^{0.85}$ dependency found by [Chassagne et al. \(2020b\)](#) in order to

recover the constant Péclet property.

CHAPTER III: VALIDATION AND DISCUSSION

CHAPITRE IV

EXPERIMENTAL INVESTIGATION OF A SINGLE LARGE PARTICLE SEGREGATING IN BEDLOAD TRANSPORT

*Après il y eut des traînées désertes et des vallons
bruissants d'aulnes, encore quelques maigres gazons,
enfin l'empire des pierres. L'ombre tâta la pointe
extrême d'une première moraine qui parut se rétracter
comme une antenne. Et elle avala des pierres, et
encore des pierres [...].*

L'amateur d'abîmes
SAMIVEL

Our literature review in chapter I has evidenced the lack of experiments on size segregation in bedload configuration. Particularly, while there are a few experiments on kinetic sieving in bedload transport (Frey and Church, 2011; Dudill et al., 2018; Ferdowsi et al., 2017), the counter balancing mechanism called squeeze expulsion, responsible for the ascent of the large particles, has been poorly studied experimentally. In this chapter we propose to investigate the behaviour of a single large particle segregating in bedload transport at various Shields numbers and size ratios. In addition, analysing such experiments at a low Shields number is very challenging and could provide unusual results. With these experiments we have two objectives. First, providing a new dataset to better understand the segregation mechanism of a large intruder in bedload transport. Secondly, evaluating the Lagrangian model presented in chapter II, which is the starting point of our upscaling modeling.

IV.1 Experimental setup

The set-up is presented in figure IV.1. A 2 meter long flume is used with a width $W = 15\text{mm}$. An obstacle of 60mm height is fixed at the output of the flume to cause bed formation. In this condition, the flume contains a 60 mm deep granular bed made of glass beads with diameter d_s . The slope is $\tan \theta = 10 \pm 0.01\%$. The flume is fed with water using a constant head reservoir and the water flow rate Q_w is measured with an electromagnetic flow meter. A bead distributor K-Tron[®] Bulk Solids Pump[™] loss in weight feeder provides a constant sediment rate. To avoid effects due to the random shape of the grains and simplify the problem, spherical transparent glass beads of density 2500 kg/m^3 (Type M glass beads from Sigmund Lindner[®]), are used to model sediments. This setup has been shown to reproduce sediment transport parameters in good agreement with classical semi-empirical bedload formulae (Hergault et al., 2010).

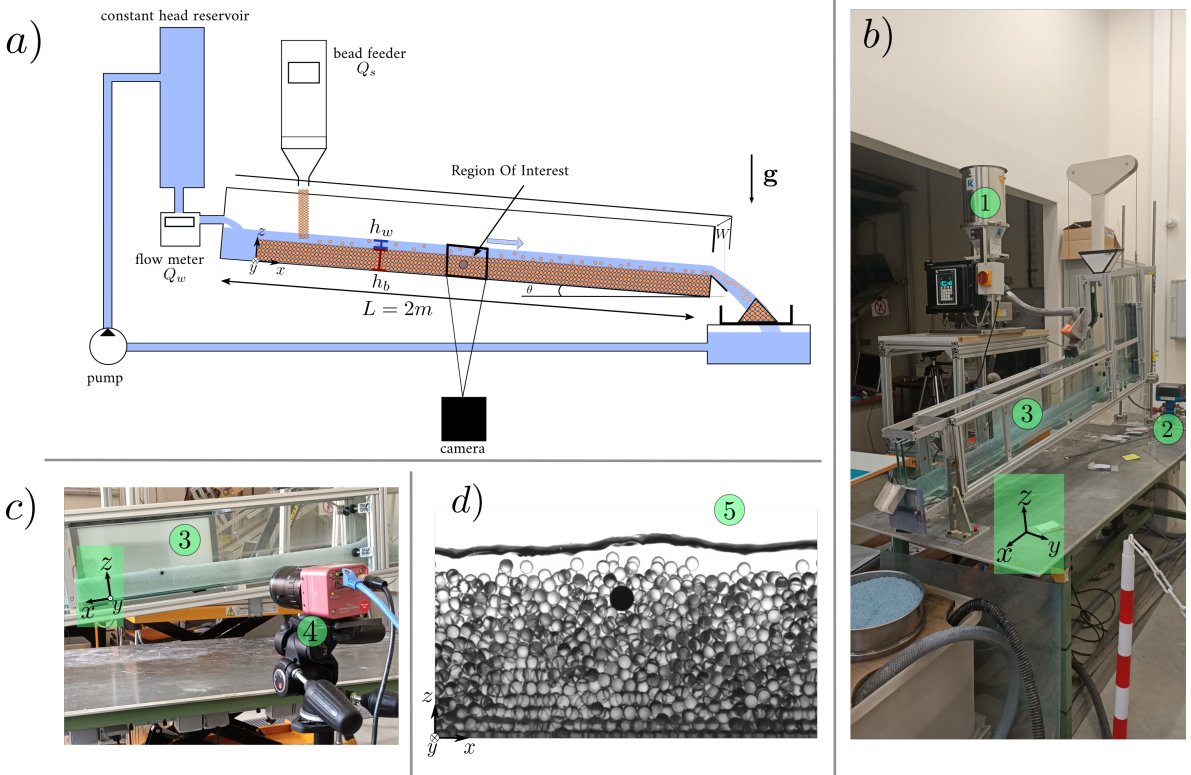


FIG. IV.1: a) Experimental set-up. b) Picture of the set-up at INRAE Grenoble laboratory . ① is the bead feeder, ② is the flow meter, ③ is the LED backlight. c) Granular bed with the intruder in the flume, ④ is the camera used for recording. d) ⑤ is the Region Of Interest (ROI).

In order to investigate steep slope size segregation of a large intruder in bedload transport, a large opaque glass bead of diameter d_l of the same density 2500 kg/m^3 , is introduced in the granular bed and monitored by image analysis.

IV.2 Procedure

The experimental procedure consists in recording the ascent of a large intruder in the granular bed of the flume. Various diameters of intruder are investigated and for each diameter, 5 to 8 repetitions were performed. For each repetition, we proceeded with the following steps:

1. The sediment rate Q_s was fixed and the water flow rate Q_w was adjusted to find transport equilibrium where the bedline (top of the granular bed) was parallel to the bottom of the flume. In order to check equilibrium, it was verified after a few minutes that the sediment rate downstream of the flume was equal to the constant rate at the bead feeder. Once this equilibrium was ascertained, the granular flux and the water flow were stopped.
2. In this step, the large intruder was manually deposited in order to have its center z_I satisfying $1.5d_s < h_b - z_I < 4d_s$, where h_b is the bed depth. We consider the bottom of the flume as the origin $z = 0$.
3. The water and the granular flow were turned on again and 1 minute was waited in order to reach the stationary state.
4. Then, the experiment was recorded until the intruder reached the surface of the granular bed or went out of the field of view, also called Region Of Interest (ROI), being advected by the granular flow.

The set-up and the tools employed imposed constraints that determined the configurations which can be investigated. The next section is dedicated to the presentation of these constraints.

IV.3 Experimental constraints

IV.3.1 Constraint linked to the detection of the intruder

The experimental set-up was originally used to study bedload transport in a 2D configuration, with an aspect ratio equal to one ($W/d_s \sim 1$). In the one hand, this narrow configuration was convenient to track each particle individually and understand the mechanisms involved in bedload transport. In the other hand, this narrow configuration increased the sidewall effects and thus generated strong dissipation of the fluid energy, making it difficult to study size segregation under large deformation of the granular bed. In order to diminish the sidewall effects, the flume has been widened to a fixed value of $W = 15\text{mm}$. Varying the diameter of the bed particles, $W/d_s = 7.5$ was reached. Yet, using such a 3D configuration, it is harder to track a particle in the granular flow because it can be hidden by surrounding particles. Two solutions were identified:

- When $W - d_l < d_s$ (which can be written $W/d_s - r < 1$), as in the left panel of figure IV.2, there is no sufficient space for a particle to move between the wall and the intruder. The intruder can be tracked all along the experiment.
- If $W - d_l > d_s$ (which can be written $W/d_s - r > 1$), a small particle can move between the wall of the flume and the intruder. In this case, the small particle hides the intruder and the tracking algorithm fails to track the intruder by transparency. Our solution consisted in placing carefully the intruder directly against the wall

as it is schemed in the right of figure IV.2. However, it was observed that for $W/d_s \geq 4$, the intruder was likely to move in the transverse direction away from the wall. While this phenomenon is negligible for size ratios higher than 2, it is not the case when r becomes close to unity. Thus, in the case $W - d_l > d_s$, for $W/d_s \geq 4$, it is not possible to study size ratios lower than 2.

The different manners of placing an intruder depending on the size ratio and the value of W/d_s are summarised in figure IV.3. The green area shows the configurations that we could access.

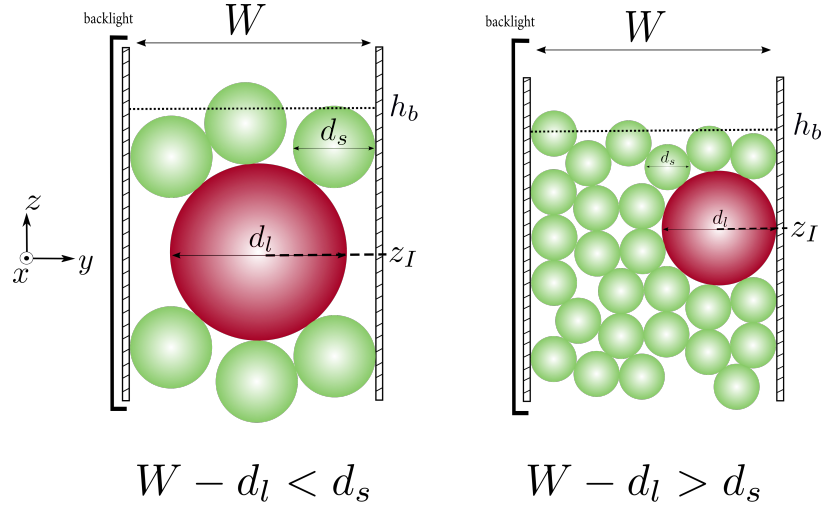


FIG. IV.2: Initial position of the large particle in the granular bed. The surface of the granular bed is at a position h_b and the depth of the center of the intruder is z_I . The scheme on the left represents the case where the intruder is sufficiently large to avoid being hidden. On the right scheme, $W - d_l > d_s$ so the particle has to be plunged against the wall to avoid a small particle to slide ahead of it.

IV.3.2 Constraint linked to the bedload configuration

Performing experiments in a bedload configuration is very challenging because of the exponential velocity, shear rate and inertial number I profiles (Maurin et al., 2016). Indeed, as the segregation velocity was shown to depend on I (Chassagne et al., 2020b), the deeper the intruder, the longer it will take to reach the bed surface and the longer the experiment. In order to limitate the experiments to a maximum of one hour, the intruder was never positioned deeper than $4d_s$ below the bed surface. At this depth, the intruder begins to segregate in the quasi-static regime and finish its ascent in the liquid flow regime. With a single experiment it is possible to investigate granular segregation in a large range of inertial numbers, from the quasi-static regime to the liquid regime. However, performing experiments spanning these two regimes is difficult. In the liquid regime, displacement of the intruder is supposed to be relatively fast, large and regular. Studying the dynamics of the intruder in this regime should be reproducible and requires small timestep to detect all the movement. On the contrary, in the quasi-static

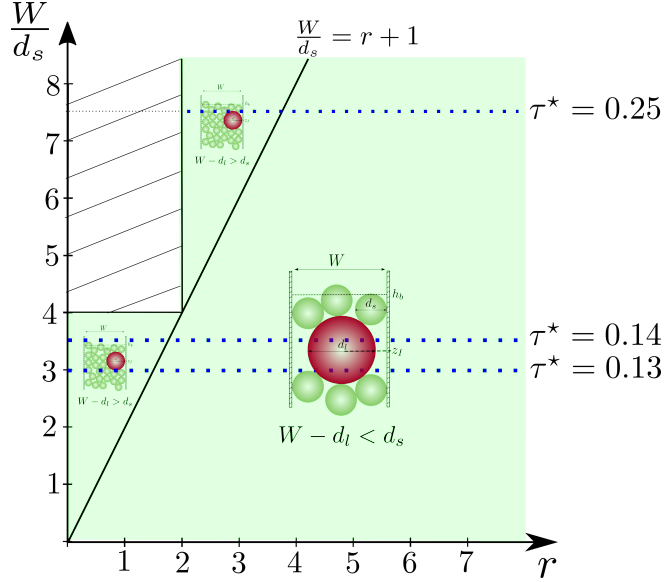


FIG. IV.3: Diagram showing the manner of placing the intruder in the bed depending on the number of particles in the width of the flume (W/d_s) and the size ratio investigated. The green area represents the configuration where it is possible to find a manner of placing the intruder. Above the line $W/d_s = r + 1$, the intruder has to be placed against the sidewall. Below this line, the intruder can be tracked without a bed particle hiding it. The blue dotted lines represent the value of W/d_s for both Shields numbers investigated and the size ratio that can be investigated.

regime, displacements are small and irregular. It is expected the displacement to be less identifiable and more difficult to interpret. Displaying the intruder position with a timestep of 0.5 second allowed us to detect sufficient information on the intruder in both the quasi-static and the liquid regimes.

IV.4 Hydraulic and granular parameters of studied configurations

In this section, the hydraulic and granular parameters of the experiments are presented. In free surface flows, the Reynolds number is classically defined as

$$Re = \frac{4U_w R_h}{\nu}, \quad (\text{IV.1})$$

where $U_w = Q_w/h_w W$ is the mean velocity of the running water, ν the kinematic viscosity and h_w is the water depth (see figure IV.1). R_h is the hydraulic radius defined as $R_h = h_w W / (2h_w + W)$. The Froude number is

$$Fr = \frac{U_w}{\sqrt{gh_w}} \quad (\text{IV.2})$$

and the Rouse number is

$$Ro = \frac{w^s}{\kappa u_*}, \quad (\text{IV.3})$$

where $w^s = (s - 1)gd_s/(18\nu + \sqrt{0.3(s - 1)gd_s^3})$ is the settling velocity of particles in suspension (Ferguson and Church, 2004), with $s = \rho^p/\rho^f$. $\kappa = 0.41$ is the Von Karman constant and u_* is the shear velocity defined as $u_* = \sqrt{gR_{hb}\theta}$. R_{hb} is the bottom hydraulic radius. Indeed, sidewalls generate fluid dissipation which is taken into account by a sidewall correction proposed by Vanoni and Brooks and Einstein (see appendix C):

$$R_{hb} = \frac{R_h}{f} \left(f + \frac{2h}{W}(f - f_w) \right), \quad (\text{IV.4})$$

where f and f_w are respectively the global and smooth wall Darcy Weisbach coefficients (see appendix C for their definition). This modified hydraulic radius is used to express the dimensionless bed fluid shear stress also called Shields number. This number, that controls the granular flux, is defined as the ratio between the shear stress at the surface of the bed and the buoyancy weight of the particles. In steady and uniform flows it reads:

$$\tau^* = \frac{R_{hb}S}{(s - 1)d_s}, \quad (\text{IV.5})$$

where $S = \sin \theta \sim \tan \theta$ since the angle of inclination θ (see figure IV.1) is small.

Our experimental campaign explored several size ratios with numerous repetitions (64 in totals). In order to limitate the total number of repetitions, the study has been restricted to two Shields numbers for different size ratios. First, a low Shields number of $\tau^* = 0.13$ was investigated with values of W/d_s around 3. Then, a higher Shields number of $\tau^* = 0.25$ was investigated with $W/d_s = 7.5$. For both Shields numbers, horizontal dotted lines have been plotted in figure IV.3 giving the size ratios that can be explored. Table IV.1 gives the different configurations we performed. A configuration is defined by Sh (1 for the lowest Shiels number or 2 for the highest), W (1 for $W/d_s \sim 3$ and 2 for $W/d_s = 7.5$) and the size ratio r.

The hydraulic parameters of the different configurations are summarised in table IV.2. Except for the case Sh1W2r2.5, the Reynolds number is always above 4000, ensuring turbulent bedload transport. For the case Sh1W2r2.5, the Reynolds number is equal to 3833. This value being close from the limit $Re = 4000$, one can expect that the regime is sufficiently far from the laminar regime ($Re < 2000$) to be almost turbulent. The Froude number is always higher than unity, meaning that the regime is supercritical. Finally, the Rouse number is always higher than 2.5 meaning that there is no turbulent suspension of the particles but only bedload transport.

Table IV.3 presents uncertainties on parameters linked to the granular material. Diameter uncertainties are given by the bead provider and used to compute the uncertainty on the size ratio Δr . One can see that the latter is never higher than 15% ensuring no overlap between the size ratios of the different configurations. For the configurations with the same value of W/d_s , Q_s and Q_w at the transport equilibrium, the water depth h_w should be the same. Yet, from one repetition to another with the same Q_s and Q_w , small perturbations can exist in the equilibrium slope of the bed. This can lead to slightly different values of the bedline h_b . In addition, h_b derived from image analysis can be slightly sensitive to local bead configurations (see section IV.5). Both of these facts should impact the water depth h_w . In order to evaluate an uncertainty on h_w , it is proposed to estimate the variations of the water depth by measuring its

Configuration	d_s (mm)	W/d_s	d_l (mm)	r	$Q_s(Kg.h^{-1})$	$Q_w(L.s^{-1})$	Nb of rep.
Sh1W1r1	5	3	5	1.0	16	0.075	7
Sh1W1r1.2	5	3	6	1.2	16	0.075	6
Sh1W1r1.7	5	3	8.6	1.7	16	0.075	6
Sh1W1r1.8	5	3	9.2	1.8	16	0.075	8
Sh1W1r2.5	5	3	12.7	2.5	16	0.075	5
Sh1W1r3.2	4	3.75	12.7	3.2	16	0.054	5
Sh1W2r2.5	2	7.5	5	2.5	8	0.023	5
Sh2W2r2.5	2	7.5	5	2.5	30	0.065	6
Sh2W2r3	2	7.5	6	3.0	30	0.065	6
Sh2W2r4.3	2	7.5	8.6	4.3	30	0.065	5
Sh2W2r5.3	2	7.5	10.6	5.3	30	0.065	5

TAB. IV.1: Summary of the configurations explored with their associated parameters. A configuration is defined by Sh (1 for the lowest Shiels number or 2 for the highest Shields number), W(1 for $W/d_s \sim 3$ and 2 for $W/d_s = 7.5$) and the size ratio r. d_s and d_l are respectively the sizes of the particle in the bed and of the intruder. Q_s is the sediment rate and Q_w is the water flow rate. The last column gives the number of repetitions for each configuration.

Configuration	h_w (mm)	R_{hb} (mm)	$U_w(m.s^{-1})$	Sh	Re	Fr	Ro
Sh1W1r1→Sh1W1r2.5	11.0	9.6	0.45	0.13	8108	1.38	5.0
Sh1W1r3.2	9.5	8.5	0.38	0.14	6353	1.24	4.7
Sh1W2r2.5	4.8	4.1	0.34	0.15	3833	1.62	4.5
Sh2W2r2.5→Sh2W2r5.3	8.9	7.6	0.49	0.25	7927	1.65	3.3

TAB. IV.2: Dimensionless numbers for the configurations. h_w is the mean depth on the configurations and repetitions.

standard deviation $\sigma(h)$. These variations on the water depth also result in a variation on the Shields number also assessed by its standard deviation. Both standard deviations are presented in the table IV.3.

Cases Sh1W1r3.2 and Sh1W2r2.5 were performed so that the Shields number should be of $\tau^* = 0.13$. For Sh1W1r3.2, the different diameter used for the bed particles and the different aspect ratio for Sh1W2r2.5 did not allow us to recover exactly the same Shields number. Indeed, Sh1W1r3.2 has a value of $\tau^* = 0.14$ and Sh1W2r2.5 has a value of $\tau^* = 0.15$. However, the standard deviations being respectively 0.02 and 0.03, it suggests that the Shields numbers are of the same order of magnitude as cases Sh1W1r1 to Sh1W1r2.5. For this reason, in the following, it will be admitted that cases Sh1W1r3.2 and Sh1W2r2.5 have a Shields number $\tau^* = 0.13$.

Configuration	Δd_l (mm)	Δr	h(mm)	Sh	$\sigma(h)$ (mm)	$\sigma(Sh)$
Sh1W1r1	± 0.3	± 0.06	11.0	0.13	1.3	0.02
Sh1W1r1.2	± 0.3	± 0.06	11.0	0.13	1.3	0.02
Sh1W1r1.7	± 0.3	± 0.06	11.0	0.13	1.3	0.02
Sh1W1r1.8	± 0.3	± 0.06	11.0	0.13	1.3	0.02
Sh1W1r2.5	± 0.05	± 0.01	11.0	0.13	1.3	0.02
Sh1W1r3.2	± 0.05	± 0.01	9.5	0.14	0.2	0.03
Sh1W2r2.5	± 0.3	± 0.15	4.8	0.15	0.5	0.02
Sh2W2r2.5	± 0.3	± 0.15	8.9	0.25	0.3	0.01
Sh2W2r3	± 0.3	± 0.15	8.9	0.25	0.3	0.01
Sh2W2r4.3	± 0.3	± 0.15	8.9	0.25	0.3	0.01
Sh2W2r5.3	± 0.3	± 0.15	8.9	0.25	0.3	0.01

TAB. IV.3: Uncertainties Δ for the parameters linked to the granular material and standard deviation σ associated to the water depth and the Shields number.

IV.5 Image processing

Image acquisition The experiment was recorded at 130 frames per second for $d_s = 5\text{mm}$ or $d_s = 4\text{mm}$ and 260 frames per second for $d_s = 2\text{mm}$, with a Photon Focus \circledcirc camera provided by Alliance Vision \circledcirc . The observation window, called Region Of Interest (ROI), has a size 1024×500 pixels. A LED backlight panel is placed behind the ROI in order to provide constant and uniform light.

Tracking of the large intruder with time The opacity of the intruder among transparent beads combined with the high frequency recording allowed us to follow the position of the large particle frame by frame. A Particle Tracking Velocimetry (PTV) algorithm developped by [Lafaye de Micheaux et al. \(2018\)](#) was used. This algorithm relies on two steps. First, with a given pattern, the center of gravity of the intruder is detected. Then the second tracking step consists in associating the detected particle on each frame to create a trajectory over time. Details and validation of these algorithms are given in [Lafaye de Micheaux et al. \(2018\)](#) and [Frey et al. \(2020\)](#). The *MATLAB* scripts are available on <https://github.com/hugolafaye/BeadTracking>.

Water line and bed line detection The water surface and the bed surface position (top of the granular bed) were estimated with the same algorithm as [Lafaye de Micheaux et al. \(2018\)](#). First, the frames are thresholded at a given grey level in order to highlight the water surface or the bed surface. Then, a gradient calculation is finally used to determine the surface line thanks to a watershed calculation on each frame. The surface lines obtained are then averaged over one thousand frames. More details can be found in [Lafaye de Micheaux et al. \(2015\)](#). The average bed and free surface lines obtained are visible in figure IV.4.

The water surface is clearly identifiable since gray level gradients are large. In addition, the fluctuations of the water surface are generally well smoothed out by averaging

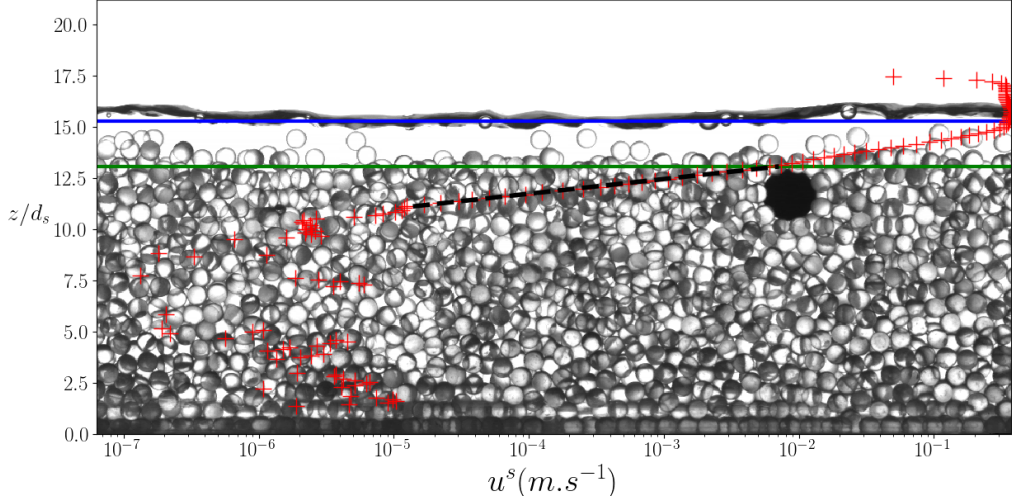


FIG. IV.4: Image of the Region Of Interest (ROI). The black particle is the large intruder of diameter d_l . The horizontal blue line is the average free surface line and the green horizontal line is the average bedline. Red crosses correspond to the average velocity profile measured with the *opyflow* toolbox. The black dashed line is the linear fit.

the waterline over one thousand frames. As a consequence, the waterline is well detected. The bedline detection is more sensitive as it exists many definitions. In this work, the bedline was chosen to be the limit between beads with enduring contacts and the particle layer above, made of saltating beads. This region is found by determining, with the eye, a grey level below which beads are always in enduring contact.

Image velocimetry processing The velocity profile of the granular bed allows one to compute the granular shear rate. This profile is essential to link the segregation dynamics to the parameters of the granular flows. Particle tracking of the beads in the bed is not feasible since the small particles overlap and are rarely identifiable. A difficulty is that in the studied configuration, the granular velocity profile decays exponentially in the bed (Maurin et al., 2016; Chassagne et al., 2020a; Frey et al., 2020) and this aspect make it difficult to use classical Particle Image Velocimetry (PIV) techniques. The *opyflow* toolbox (<https://github.com/groussea/opyflow>) developed by Rousseau and Ancey (2020) and based on the *openCV* library written in *Python*, provides an efficient solution to tackle our configurations.

This toolbox is based on the measuring of the *Optical Flow*, a method classically used in the computer science community, which provides the displacement field between two frames by minimizing the square of the *Displaced Frame Difference*. It can be done using different kinds of algorithm but the *openCV* library used in *opyflow* proposes a pyramidal implementation of the *Lukas Kanade* method (Bouguet, 2000). This toolbox has been successfully tested in the case of turbulent flow over granular beds (Rousseau and Ancey, 2020). Also, it has been calibrated and validated in the context of our flume using the data of Frey et al. (2020) (see appendix B).

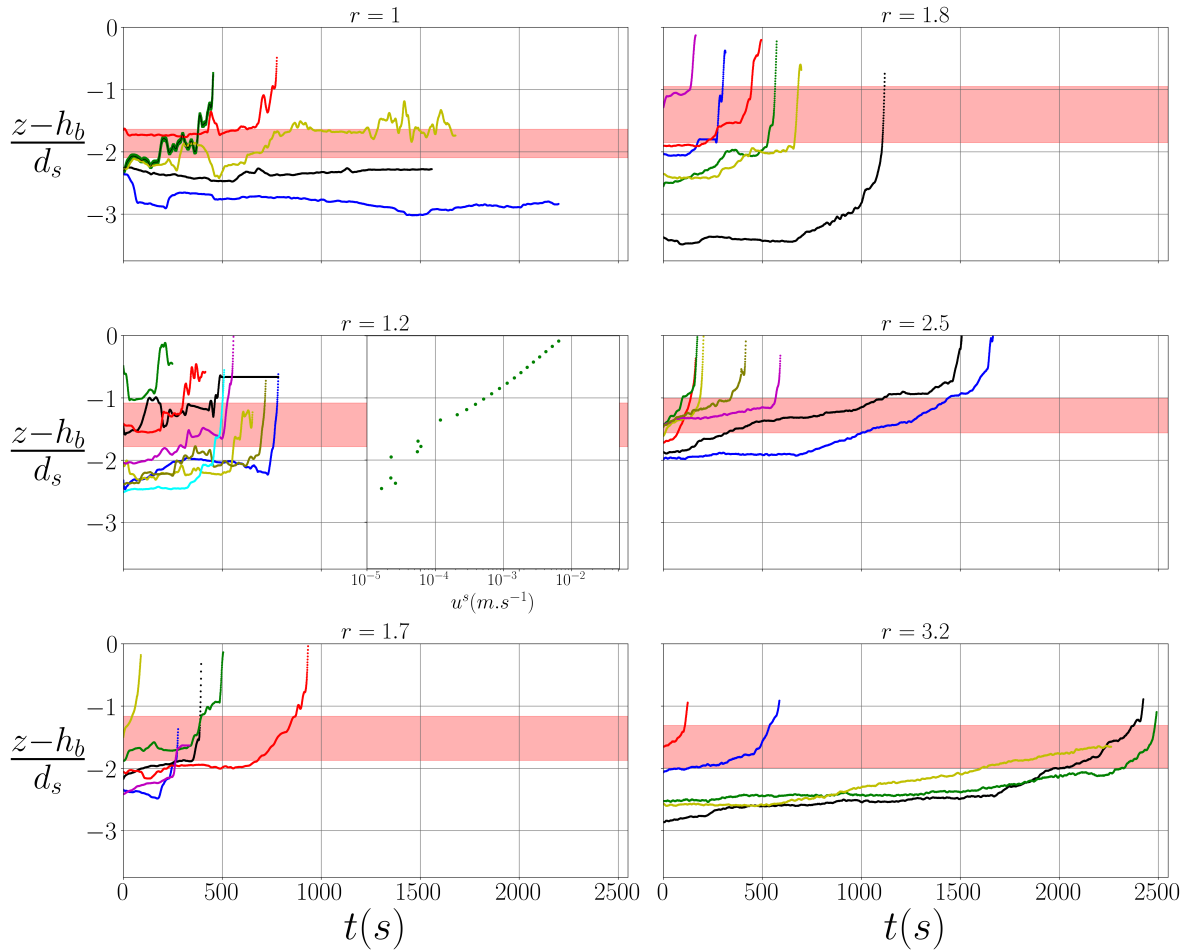
In order for this algorithm to provide relevant results, the maximum displacement of a given particle between two successive images must be less than its diameter. Our acquisition frequency has been chosen to satisfy this criteria (130 fps for 5mm and 4mm particles with $\tau^* = 0.13$ and 260 fps for 2mm particles with $\tau^* = 0.25$). The obtained average velocity field provides the velocity profile (red cross) shown in figure IV.4. One can observe that the exponential velocity profile (linear in semilog plot) is recovered above $10^{-5} m.s^{-1}$. Deeper, the profile is not recovered since the grain displacements are not large enough over the experimental period. The dashed black line of figure IV.4 represents the linear fit of the granular streamwise velocity profile near the bed surface.

IV.6 Results

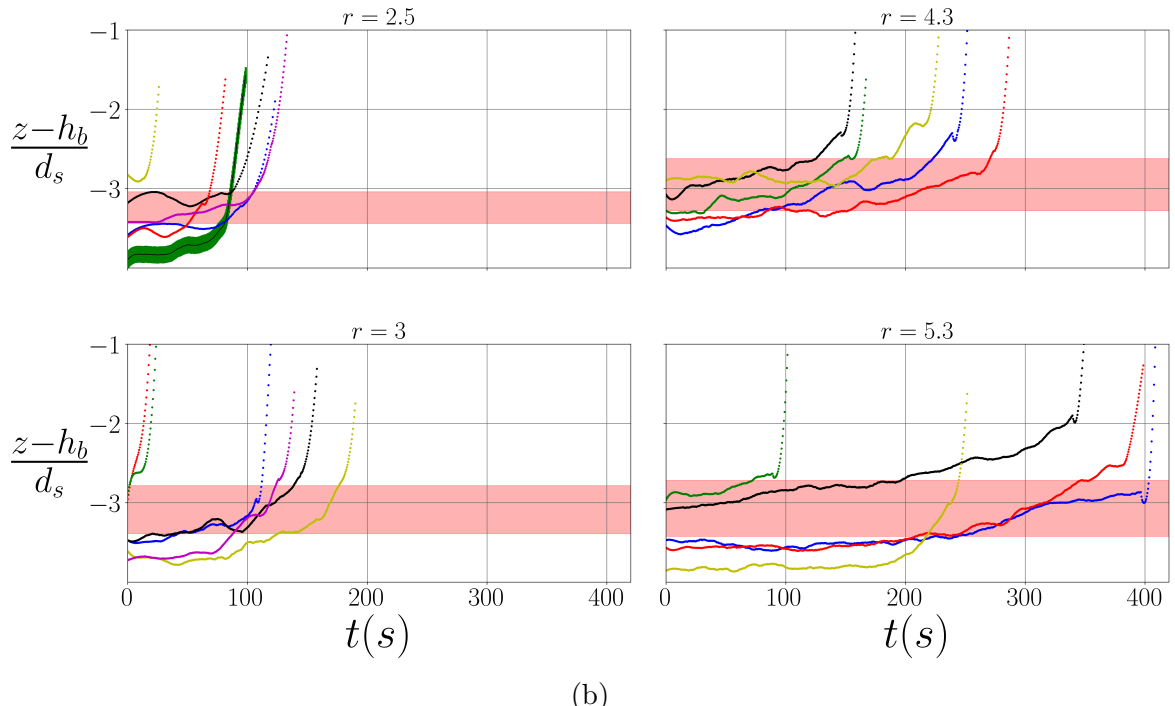
In figure IV.5a the depth of the center of the intruder is plotted against time for $\tau^* = 0.13$ (configurations Sh1W1r1 to SH1W1r3.2). As an example, for the size ratio $r = 1.2$, the semilog inset shows the exponential behaviour of the velocity profile. It is observed that for size ratios higher than $r = 1.2$, the intruders always segregate toward the top of the bed (axis $z = 0$). The last position of each repetition corresponds to the last timestep before the intruder reaches the bedline. It will be considered to be the final segregation time called t_{end} . This last vertical position of the intruder is sometimes far from the bedline due to the display timestep of 0.5 second between each position.

Two different stages are observed in the segregating intruder dynamics. At first, the intruder has a slow ascent characterised by a low vertical displacement. At this stage, the intruder can stay at the same depth for a long duration before rising again, leading to an intermittent behaviour. The deeper the initial depth, the longer the slow ascent. The deepest intruders can even stay at their initial vertical position for a very long time before beginning to rise slowly. Also, for repetitions having the same initial depth, the duration of the slow ascent regime vary from one repetition to another and the time for the intruder to segregate can differ for example by a factor up to five for the case $r = 2.5$. Based on these raw data, it is hard to conclude on the repeatability of these experiments with the first stage being inherently stochastic.

In the second stage, the intruder kinematics drastically changes. It is characterised by a curvature corresponding to a sudden increasing of the vertical acceleration of the intruder. The curvature is defined as the convexity that breaks the slow ascent regime. It is observed that after this point, the curves become linear and almost vertical, showing that the velocity can be considered constant before the intruder leaves the bed. It is interesting to see that for a given size ratio, the convexity does not appear always at the same depth. For example, in the case $r = 1.8$, for the green curve, it appears two diameters below the bedline, while it appears 3 diameters below the bedline for the black curve. It suggests that the acceleration could be independant on the depth of the intruder. The red horizontal envelope for each size ratio represents the transition between the quasi-static regime (characterized by random non-local rearrangements) and the liquid flow regime (rearrangement linked to the local shear rate). The upper boundary corresponds to $I = 0.01$ while the lower limit is $I = 0.001$. The curvature



(a)



(b)

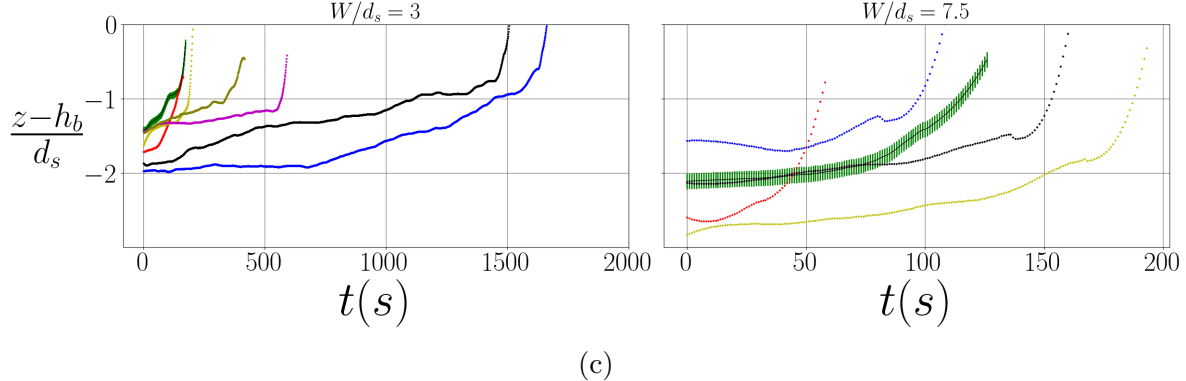


FIG. IV.5: Vertical position of the center of the intruder with time for the different size ratios. (a) is the case $\tau^* = 0.13$, (b) is the case $\tau^* = 0.25$ and (c) is the comparison between $W/d_s = 3$ (left column) and $W/d_s = 7.5$ (right column) for a size ratio $r = 2.5$ with $\tau^* = 0.13$. The green envelope only given for clarity on each first configuration, corresponds to the potential error on the detection of the particle center. The red horizontal envelope for each size ratio represents the transition between the quasi-static regime and the liquid flow regime. The upper boundary corresponds to $I = 0.01$ while the lower limit is $I = 0.001$. In (a), for the size ratio $r = 1.2$, the averaged streamwise velocity profile of the particle bed is represented in the inset.

is not always in the red envelope, showing that there is no evident link between the acceleration of the intruder and the transition between the quasi-static part of the bed and the liquid flow regime. For a given size ratio, in most repetitions, the deeper the initial position, the longer it takes to reach the surface.

In order to investigate the influence of the Shields number, the same experiments have been carried out at a Shields number nearly twice higher ($\tau^* = 0.25$). For this value, experimental constraints impose to investigate only size ratios higher than $r = 2$ (see figure IV.3). The results can be seen in figure IV.5b for configurations Sh2W2r2.5 to Sh2W2r5.3. For this highest Shields number, it is observed that the transition between the quasi-static and the granular liquid flow regime is located 3 diameters below the surface of the bed while for a lower Shields number it was located only 1.5 diameter below. Doubling the Shields number has doubled the depth of the liquid flow regime, allowing us to study the behaviour of the intruder in the liquid regime on a deeper distance.

For all repetitions, the intruder segregates. Compared with the case $\tau^* = 0.13$, the same patterns are observed. First one can see, a region where the intruder rises slowly with small vertical fluctuations. Then the abrupt acceleration of the intruder is observed again. As in the case $\tau^* = 0.13$, the convexity is not always correlated with the transition between the quasi-static and the liquid flow regions and still appears at various depths. The difference between both Shields numbers lies in the segregation duration. For size ratios $r = 2.5$ and $r \sim 3$, one can see that the intruder segregates faster at the highest Shields number. As an example, for $r = 2.5$ in the case $\tau^* = 0.13$, two diameters below the surface, it can take approximately 1500s to segregate while at $\tau^* = 0.25$, 3 diameters below the bedline, it only takes about a hundred second to segregate. For $r = 2.5$ and an initial depth of 1.5 d_s below the bedline, the duration can vary by a factor five for

$\tau^* = 0.13$ (between 100s and 500s). For the case $\tau^* = 0.25$ the segregation duration is more likely to vary by a factor two (except for the case $r = 5.3$ where for an initial depth of $3 d_s$ below the surface, the duration varies by a factor 3.5), suggesting that with a higher Shields number, the segregation duration is less dispersed.

At the lowest Shields number, it was possible to investigate smaller size ratios. For configurations $r = 1$ and $r = 1.2$, the phenomenology is quite different from our higher size ratios. For $r = 1.2$, the intruders rise toward the bed surface but the ascent is much more intermittent than for higher size ratios due to larger vertical fluctuations. For this reason, the curvature is less remarkable and thus, the two stage dynamics is less evident. In configurations $r = 1$, the red and the green curve present the same phenomenology as for $r = 1.2$. In the other repetitions, the intruder position fluctuates around its initial position but it does not segregate within the observation time of the experiment.

In granular flows, it is well known that the presence of sidewalls may strongly influence the dynamics of the particles (Jop et al., 2005). Configurations Sh1W1r1 to Sh1W1r3.2 have been performed for aspect ratios equal to 3 and 3.75. In order to study the effect of this ratio, configuration Sh1W2r2.5 has been performed at the same Shields number $\tau^* \sim 0.13$ (see section IV.4) but with a value of W/d_s equal to 7.5 (see figure IV.5c). It is observed that the shape of the curves does not change with the geometry. However, the segregation duration differs significantly with W/d_s for the same Shields and the same size ratio. For initial depths around 2 diameters below the surface, it takes about 1500 and 1600 seconds for the intruder to segregate in the configuration $W/d_s = 3$ while it takes 125 and 150 seconds for $W/d_s = 7.5$, showing that the segregation duration may vary by a factor ten between both aspect ratios.

The depth of the center of the intruder with time gives information on its segregation kinematics but we are also interested in investigating its spatial behaviour. This analysis gives new results on the mechanism of vertical size segregation in bedload transport.

In order to do so, we now focus on the trajectory $z(x)$ of the intruder. Figures IV.6a to IV.6b represents the vertical displacement $z(t)$ against the streamwise displacement $x(t)$ for both Shields numbers. For all size ratios higher or equal to $r = 1.7$ it is striking that the trajectories $z(x)$ are linear for both values of the Shields number. In some repetitions, the intruder can be advected in the streamwise direction without any vertical displacement. It forms a horizontal plateau which is mainly observed at the beginning of the trajectories, before the intruder rises. In most of the repetitions with a size ratio above $r = 1.7$, this plateau gives the floor to the ascent with a linear trajectory. This linearity shows that once the intruder has begun to move vertically, the streamwise movement of the particle is systematically associated with an upward vertical movement.

Most surprisingly, the Shields number does not modify the linear behaviour of the trajectory. For a given configuration, whatever the initial position of the intruder, linear trajectories tend to collapse meaning that the linear ascent is somehow universal. A fit on trajectories allowed us to determine the mean slope. The order of magnitude is the same for both Shields number with a mean value around 0.3. Surprisingly, there is no obvious variation of this slope with the size ratio. This suggests that whatever the

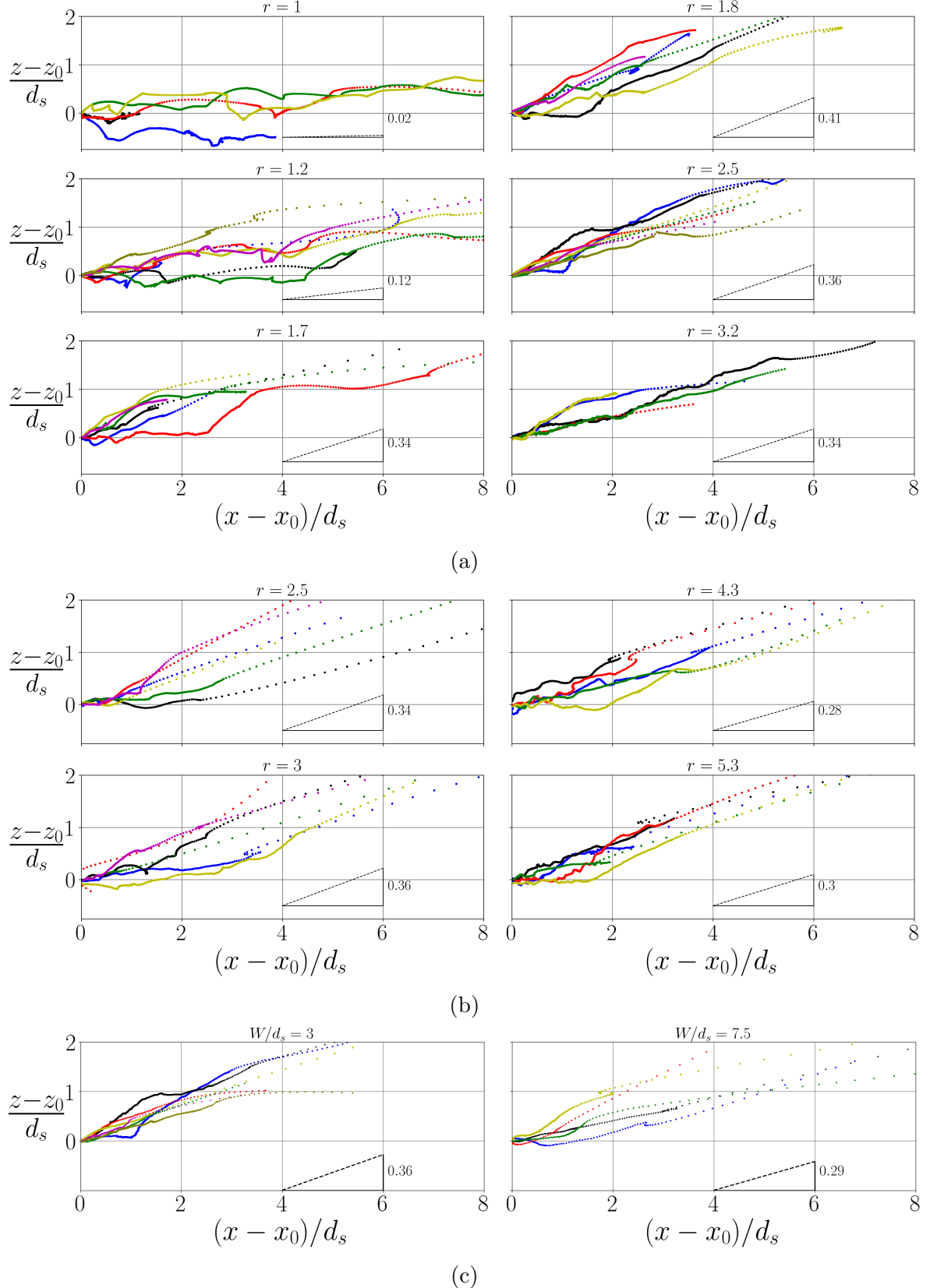


FIG. IV.6: Vertical displacement of the center of the intruder as a function of the streamwise displacement. The dashed line (----) corresponds to the averaged slope on all repetitions. (a) $\tau^* = 0.13$, (b) $\tau^* = 0.25$ and (c) compares the case $W/d_s = 3$ and $W/d_s = 7.5$ for $\tau^* = 0.13$. x_0 and z_0 are for the initial position.

depth, the size ratio or the Shields number, the slope of the linear trajectory is the same. Lastly, figure IV.6c represents the trajectory for $\tau^* = 0.13$ but with two aspect ratios W/d_s . Here again a different W/d_s does not significantly change the mean slope. For $W/d_s = 7.5$ the slope is 0.29 compared to 0.36 in the case $W/d_s = 3$, which is within the variability for a given configuration.

By contrast, for size ratios $r = 1$ and $r = 1.2$, in figure IV.6a, the spatial behaviour of the intruder is very different. The intruder moves spatially with successive ascents and falls resulting in a spatial random behaviour with an intermittent ascent. For the case $r = 1.2$ the intruders have a tendency to rise higher than for the case $r = 1$, but the linear trajectory is broken by the descent of the intruder. In these configurations, the streamwise displacement is generally larger than for configurations with a linear trajectory. It indicates that the intruder has a higher capacity to be transported along the streamwise direction by advection and a lower probability to segregate vertically. This result is intuitively physically sound as the particles having $r \sim 1$ are tracers for the granular flow. As the size ratio increases, the streamwise advection is reduced and the spatial dynamics changes to the linear trajectory observed for larger size ratios. Our experimental results suggests that a regime transition occurs for $r \in [1.2; 1.7]$.

IV.7 Discussion

In the last section we have shown that the time taken by an intruder to segregate varies significantly with the size ratio, the initial depth, the Shields number and the aspect ratio W/d_s of the flume. In this section, we try to identify the potential origins of this stochastic behaviour. In addition, we try to understand the origin of the linear trajectory observed for size ratios above $r = 1.7$. Finally, we wonder if the lift force formulation proposed by [Guillard et al. \(2016\)](#) is sufficient to model this mechanism.

IV.7.1 Segregation dynamics

In section IV.6, visual observations of the segregation of the large intruder with time suggested an exponential behaviour for all experiments with size ratio $r = 1.7$ and for some repetitions with size ratio $r = 1.2$. In figure IV.7 these repetitions have been rescaled by the time t_{end} and the final position $z(t_{end})$. In order to focus on the convexity and the final part of the curves, where the ascent is rapid, only the 60 last seconds are shown. The semi-logarithmic plot shows that beyond the appearance, the vertical position does not rise exponentially with time. Nevertheless, it shows that the vertical velocity increases very rapidly as the intruder becomes closer to the surface. This is in line with the measured exponential streamwise velocity profile. In addition it suggests that the segregation velocity could indeed increase with the inertial number as found by [Fry et al. \(2019\)](#) and [Chassagne et al. \(2020b\)](#). For a given size ratio, the curves have a tendency to be superimposed, meaning that the kinematics of the ascent is nearly the same for all configurations and suggesting that the the large variations of segregation duration are due to the first stage of segregation with strong intermittent motions.

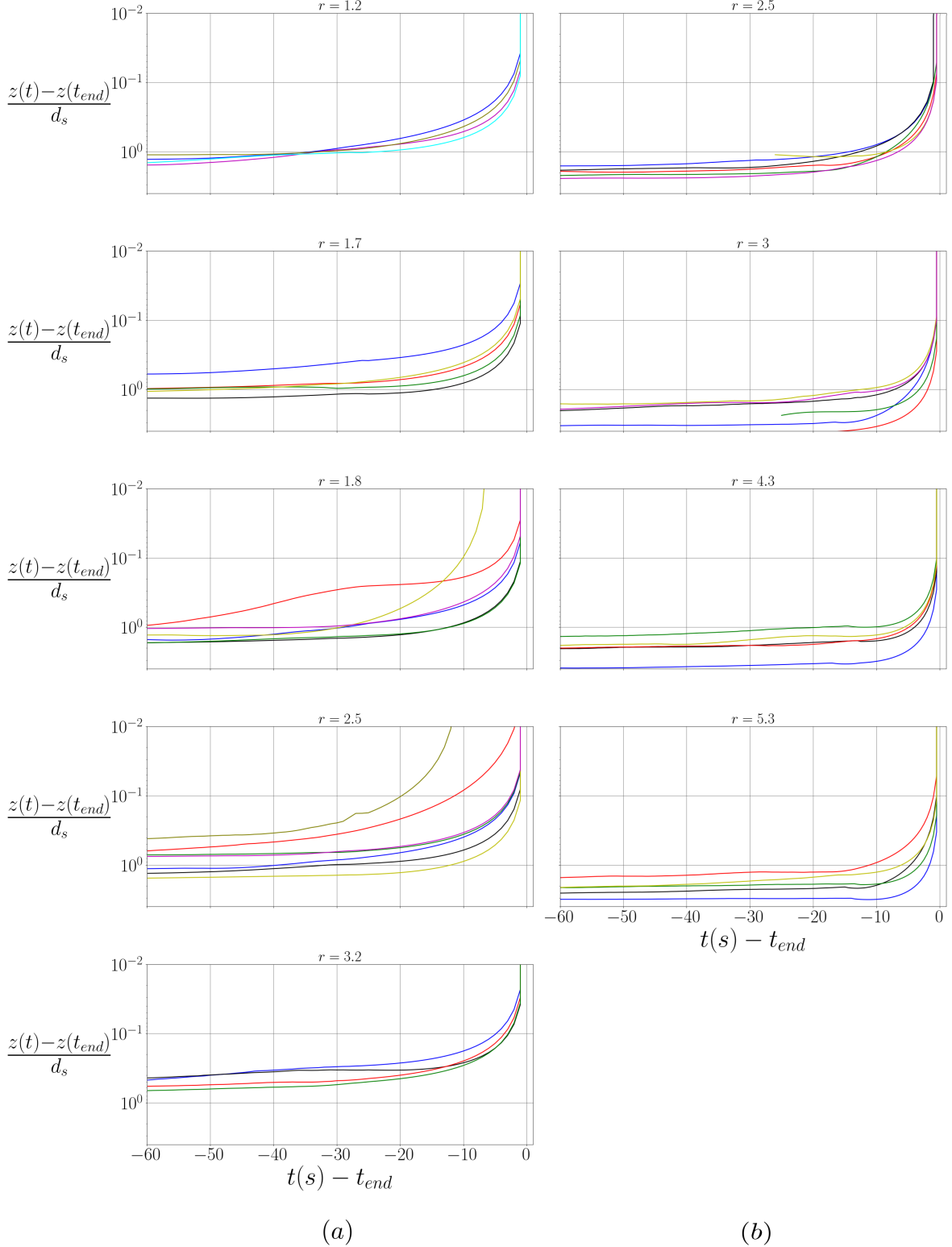


FIG. IV.7: Semi-log plot of the intruder center elevation as a function of time, rescaled by the final time t_{end} , $z(t) - z(t_{end})$. The 0 value on the horizontal axis represents the last time. (a) $\tau^* = 0.13$. (b) $\tau^* = 0.25$. Colors correspond to the same repetitions as in figure IV.5.

Ferdowsi et al. (2017) investigated size segregation in bedload transport with a laminar configuration using large particles having a size ratio $r = 2$. By tracking individually the large particles, they were able to compute the vertical Mean-Square Displacement (MSD) for different initial depths. The authors identified two time scales. In the liquid flow regime, at short times, particles experienced vertical MSD growth close to ballistic motion ($MSD \propto t^2$). On the contrary, at short times, in the quasi-static regime, the vertical MSD increased with time ($MSD \propto t$) or even slower, suggesting a diffusive behaviour. In the quasi-static regime, based on (Choi et al., 2004; Marty and Dauchot, 2005), the authors identified this behaviour to caging effects in which the particles are trapped by the surrounding small particles before being able to rise again once random rearrangements destroy the cage structure.

The two regimes we observed could be linked to the mechanisms observed by Ferdowsi et al. (2017). In our case, we observed that the first stage of the ascent is likely to occur in the transition region between the quasi-static and the liquid regime. Therefore, the motion of the intruder in this area, before the convexity, could be linked to caging effects as described by Ferdowsi et al. (2017) and the low repeatability could arise from the random formation of cages. Once the intruder approaches the transition between the quasi-static and the liquid flow regime, cages tend to disappear and the intruder can rapidly find a configuration in which it can accelerate.

In order to assess our hypothesis, we computed the vertical MSD for each size ratio as $MSD(t) = \Delta z^2(t) = \langle |z(t) - z(t_0)|^2 \rangle$, where t_0 is the initial position. In the region where the slow ascent regime was identified, we found that MSD increases approximatively with time, suggesting that the intruder could have a diffusive behaviour. However, our results were still unclear since the variability was high between the different configurations. We believe that a statistical analysis with DEM simulations could provide clearer results.

The random caging effect could be influenced by the geometry of the flume. Indeed, in the previous section, the effect of the aspect ratio on the segregation time suggests that a higher value of W/d_s leads to a shorter much less dispersed segregation duration. The experiments at $\tau^* = 0.25$ have been performed at $W/d_s = 7.5$ and the aspect ratio is therefore higher than for configurations at $\tau^* = 0.13$, where $W/d_s \sim 3$. We believe that it could explain the lower dispersion and the lower segregation duration observed for $\tau^* = 0.25$. With $W/d_s \sim 3$, the granular flow could be more constrained due to the near presence of sidewalls and the probability of rearrangement for the contact network would be lower, with increased caging. It implies that the aspect ratio of the flume is of major importance when performing experiment in granular media (Jop et al., 2005). Both Shields numbers have been obtained by varying the aspect ratio. As a consequence, it is difficult to determine if the difference in the segregation duration is due to the change of fluid forcing or to the change of aspect ratio (probably both). Thus, we cannot study in detail the impact of the Shields number on the segregation duration.

For a given Shields number, we can study the dependency of the segregation duration on the size ratio. In figure IV.8, for configurations of figure IV.7 (i.e. for particles that segregate), the average final segregation time t_{end} has been plotted as a function of the size-ratio. In order to analyse the segregation duration with the same initial depth, only

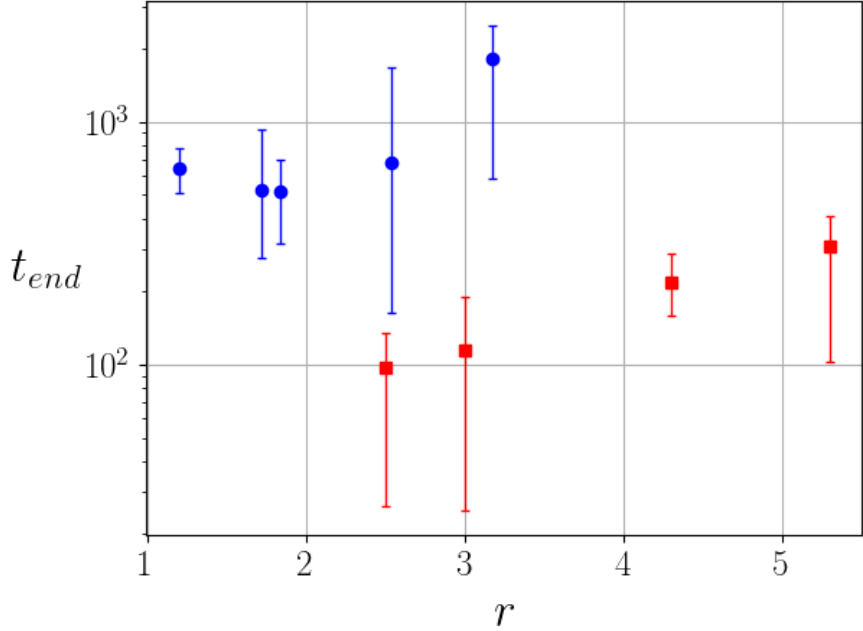


FIG. IV.8: Average segregation final time t_{end} as a function of the size ratio. Blue circles for $\tau^* = 0.13$, red squares for $\tau^* = 0.25$. Errorbars give maximum and minimum segregation final times.

an initial depth between $-1.5d_s$ and $-2.5d_s$ has been selected for $\tau^* = 0.13$ and between $-2.5d_s$ and $-3.5d_s$ for $\tau^* = 0.25$. The errorbars are determined by the extremum values obtained for each size ratio and can be very large for configurations that have a low repeatability. Yet, it is still possible to observe trends. For the highest Shields number (red squares), the segregation duration is positively monotonous with r . For the lowest Shields number (blue circles), an interestingly minimum, or at least a threshold segregation duration seems to emerge around $r = 1.7$ and $r = 1.8$. Regarding our error bars we can also locate it at $r \sim 2$. Such a result is in line with [Guillard et al. \(2016\)](#) and [Jing et al. \(2020\)](#) who reported a maximum segregation force on a large intruder for $r \sim 2$. [Golick and Daniels \(2009\)](#), with shear cell experiments, also observed a minimum segregation duration for $r \sim 2$. The results in figure IV.8 indicate that the bedload configuration, i.e. with an exponential shear rate and the presence of water seems to also exhibit a maximum efficiency of segregation about $r \sim 2$ and thus, that this extremum for the segregation velocity, could be independent on the configuration.

At $\tau^* = 0.13$, $r = 1.7$ and $r = 1.8$ correspond to size ratios for which a change of behaviour is observed in the parametric curve $z(t)$ and in the trajectory $z(x)$. In order to highlight the change of behaviour of the trajectory, the mean slope $\tan \alpha$ is plotted for each size ratio in figure IV.9. It is observed that for $r = 1$ and $r = 1.2$, the slopes are below $\tan \alpha = 0.2$. On the contrary, for higher size ratios, the slopes are almost always above this value showing a clear threshold above $r = 1.7$. In the context of 2D vibrated systems, using a geometrical model, [Duran et al. \(1993\)](#) predicted the change from intermittent to continuous ascent for a size ratio $r \sim 2.8$. Their results confirm the work of [Jullien et al. \(1992\)](#) who found, in a 3D vibrated system, that above $r \sim 2.8$, the

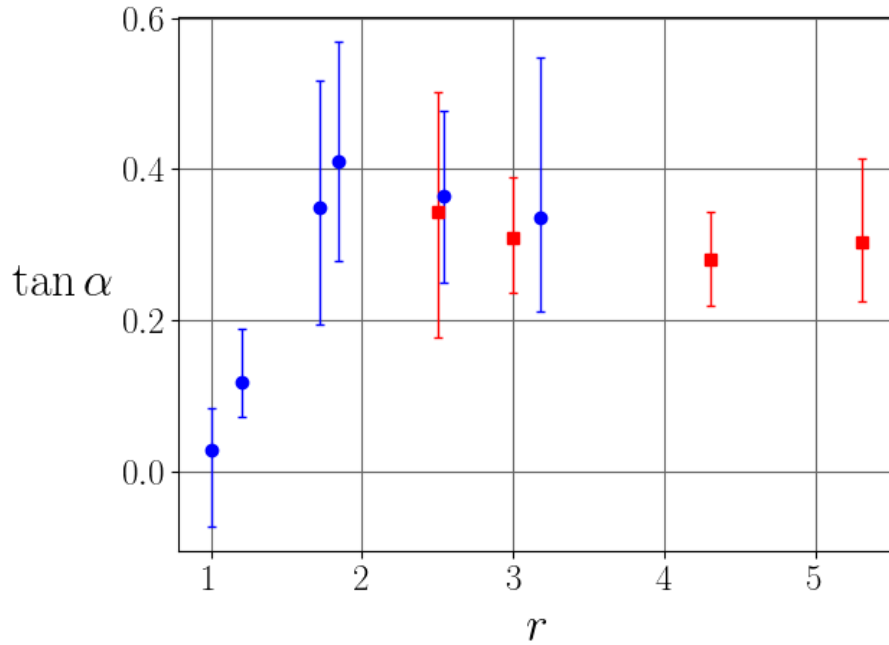


FIG. IV.9: Mean slope measured on the trajectories $z(x)$ for each size ratio. Blue circles for $\tau^* = 0.13$, red squares for $\tau^* = 0.25$. Errorbars give maximum and minimum slope values.

intruder was not limited in its ascent and rose continuously. The size ratio for which a continuous ascent is observed in this study is lower but the bedload configuration is different from vibrated systems as the regime is stationary and the shear uniform. However, it is interesting to observe that a threshold of behaviour with the size ratio is observed in our bedload configuration. Below this threshold, figures IV.5a and IV.6a show that the intruder dynamics exhibits fluctuations in its vertical position because it rises but also falls down. It is hypothesised that for a size ratio close to unity, the intruder is advected in the streamwise direction and is submitted to self diffusion. It can either rise or fall into gaps created in the granular matrix but also being caged. If the size ratio is a bit higher than unity, the segregation mechanism can exist but the size difference is not large enough for the segregation to be efficient and this could explain why for $r = 1.2$ the intruder can segregate but less continuously. As the size ratio increases, the trajectory of the intruder becomes linear. It means that the intruder only rises and reveals that the segregation phenomenon becomes predominant. In the next section, we discuss in more details this linear trajectory with a surprisingly constant slope.

IV.7.2 Origin of the linear trajectory

In this section, we focus on the linear trajectory observed in figures IV.6a and IV.6b for size ratios above $r = 1.7$. As far as we know, the ascent with a linear trajectory was first reported by Duran et al. (1993) in the case of vibrated system. Vibrated configurations are classically considered as different since the deformation of the media is made by agitation which differs from sheared experiments. The trajectory being

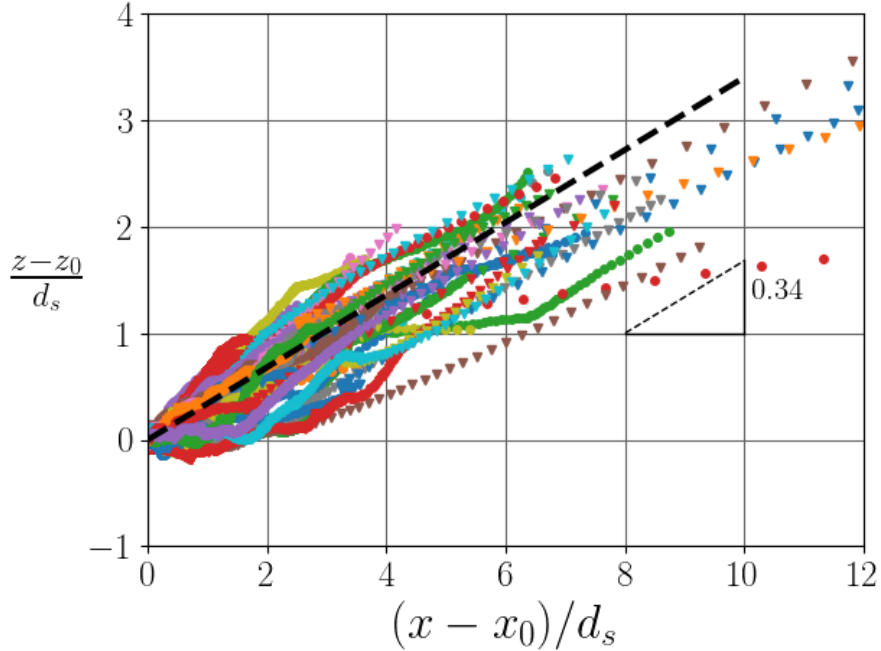


FIG. IV.10: Gathering of all the linear trajectories obtained experimentally. The black dotted line is the averaged slope measured. The standard deviation on the average slope is $\sigma(\tan \alpha) = 9.7 \times 10^{-2}$.

linear in both configurations, it suggests that similarities could exist in the segregation mechanism. Duran et al. (1993) made their experiment with a low deformation, that is to say in the quasi-static regime. They argue that the observed linear trajectory was due to an arching effect where the intruder is carried by the archs created by the force chains in the quasi-static regime. Our linear trajectory could be observed either in the quasi-static or in the liquid flow regime showing that it is not necessarily a consequence of the archs developing in the quasi-static regime.

Trajectories for all repetitions have been plotted in figure IV.10. The black dotted line is the average linear slope on all repetitions. It gives a value of $\tan \alpha = 0.34$ with a standard deviation measured as $\sigma(\tan \alpha) = 9.7 \times 10^{-2}$. The equivalent angle is $\alpha = 19.3^\circ$. Duran et al. (1993) found the slope of the linear trajectory to be around 60° and mentioned that this angle corresponds to the 2D static angle of repose for monodisperse disks. In our flume, with $W/d_s = 7.5$ the critical angle of repose has been determined by measuring the angle at which the dry bed, made of glass beads, starts to flow continuously. This angle was found to be $\theta_{start} = 26.6 \pm 1.2^\circ$ which is higher than the slope of $\alpha = 19.3^\circ$. This result suggests that the slope of the linear trajectory is not controlled by the static angle of repose.

A typical segregation mechanism has been observed during the experiments, which could be responsible for the linear trajectory. This mechanism is shown in figure IV.11. Each column of figure IV.11 corresponds to a particular repetition for a size ratio $r = 2.5$ with $\tau^* = 0.13$. Figure IV.11a shows the initial layout before the process begins. The center of the intruder has been marked in red and two key particles have been marked

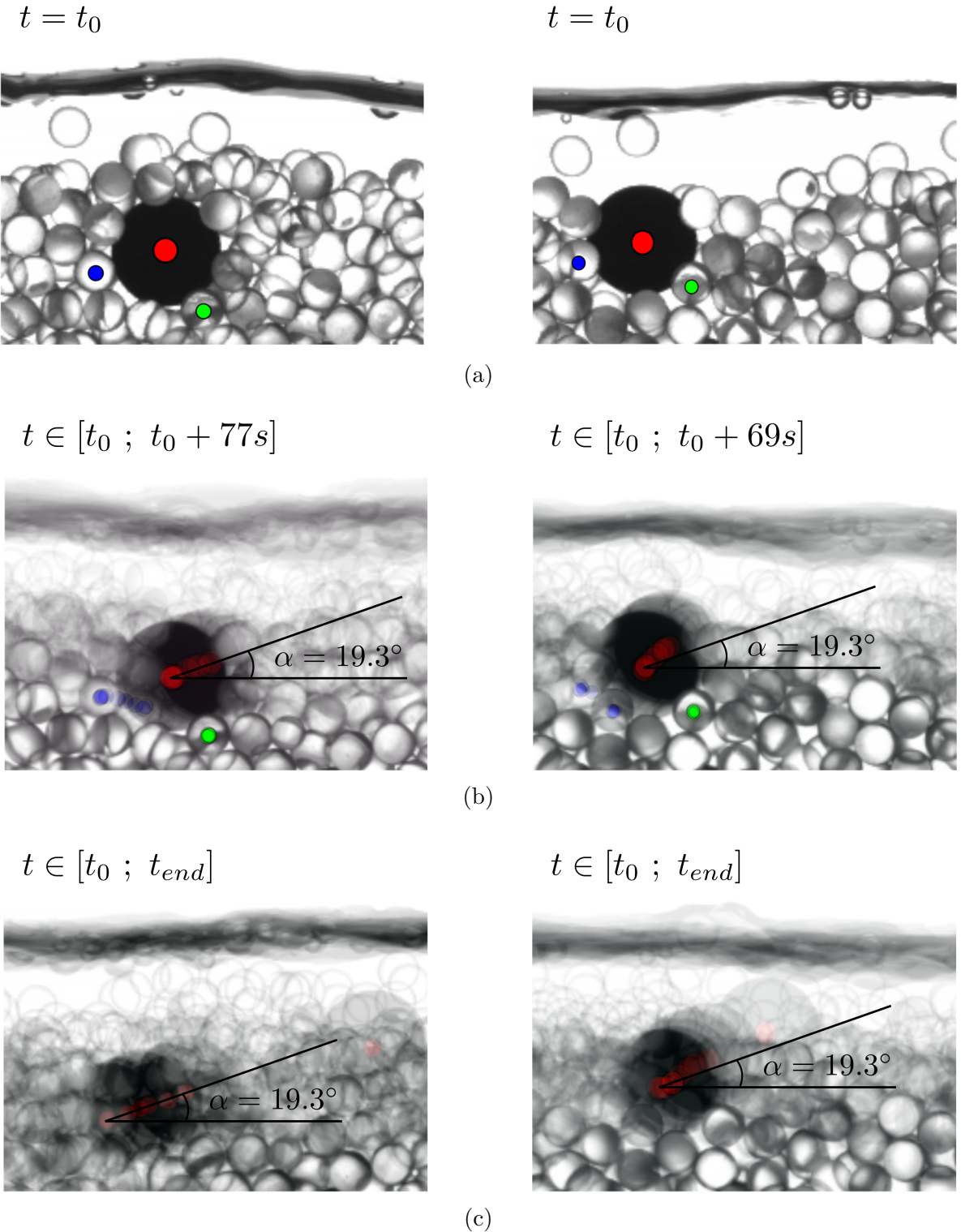


FIG. IV.11: (a) Initial layout before the observed mechanism occurs, for two repetitions with size ratio $r = 2.5$. (b) Mean images over a period $t \sim 70s$, with 1 image/s, after the initial layout presented in figure (a). (c) Mean images until the end of the experiments.

in green and blue. Figure IV.11b represents the mean images over one period of the mechanism. It reveals the displacement of the intruder as well as the displacement of the two markers during the ascent of the intruder. The flow is from the left to the right. On this image, one can see that the intruder segregates upward in the direction of the flow. The red points gather on a line having a slope similar to the averaged slope $\alpha = 19.3^\circ$. While the green marker at the bottom left does not move, the blue marker at the bottom right moves downward to the left. When the blue particle moves below the intruder it seems to push the intruder upward in the streamwise direction. The fact that the green marker does not move suggests that this contact could represent a pivot point over which the intruder is rolling, ultimately leading to an increase of the contact stress at the bottom left of the intruder. Such stress increase at the bottom front of the intruder has been observed by [Guillard et al. \(2014\)](#) and [Van der Vaart et al. \(2018\)](#) who reported an asymmetric stress originating from a complex circulation around the intruder and independent from the mean pressure. Finally, figure IV.11c shows the mean image over the whole experiment for both repetitions. The red points illustrate the linear trajectory observed and still gather on the 19.3° slope. We believe that the mechanism highlighted in figure IV.11b repeat until the intruder has completely segregated.

When the size ratio increases, the number of neighbours around the intruder becomes larger and it is more difficult to observe the displacement of given surrounding particles. Nevertheless, the angle of the linear trajectory seems to be independant on the size ratio, suggesting that the segregation mechanism in figure IV.11 could be universal. In the results section (section IV.6), it was observed that the only change with the size ratio was the time needed for the intruder to segregate. Two options are identified to explain this phenomenon.

The first possibility is that small particles circulate less easily under the intruder and thus it takes more time for the mechanism to occur. A second possibility is that a large number of small particles need to circulate below the intruder to raise it over the same height.

The first option is unlikely since for a large size ratio, the small particles are more mobile and more able to fill the gaps between the intruder and the underlying small particles. For the same Shields number and the same diameter of small particles, the number of rearrangements should be in average the same whatever the size of the intruder. These rearrangements could have a different impact on the intruder following its size, explaining the increase of segregation duration. Therefore the second option seems more relevant and suggests a mass effect. The small particles moving below the intruder carry less momentum compared to what is needed to lift the intruder and the latter has to be lifted by more and more particles as the size ratio increases. This would mean that the dependency on the size ratio could result from a balance between the momentum carried by the small particles and the weight of the intruder to lift.

In this way, even if small particles can segregate downward more easily as the size ratio increases, their effect on the large particle could be different. This idea was suggested by [Van der Vaart et al. \(2015\)](#) who reported an asymmetric velocity between small and large particles showing that the segregation behaviour of the large particle was different from the small particles. This could also explain why [Chassagne et al. \(2020b\)](#) observed

that the segregation velocity of the small particles increases exponentially with the size ratio without an extremum while a maximum segregation efficiency is often observed for $r \sim 2$ for large particles (Golick and Daniels, 2009; Guillard et al., 2016; Jing et al., 2020).

With figure IV.11b, an interpretation of the segregation mechanism in bedload transport has been proposed. It was observed that a small particle at the bottom front of the intruder was not moving, blocking the intruder and possibly increasing the normal stress locally. Ding et al. (2011) studied experimentally and numerically the forces exerted on different long intruder with different cross sections pulled into a granular bed. They were able to measure the local forces on the differential elements of the intruder using a plate at the same depth with an angle having the same angle of attack as the differential element of the intruder (the angle varies between 0° and 180° , with 0° corresponding to the bottom of the intruder). A strong force asymmetry was found between the upper and the lower part of the intruder suggesting that contrary to the fluid case, the force asymmetry is not induced by the geometry but by the specificity of the granular medium. With the setup presented in figure I.5a, the local vertical force f_z they measured as a function of the angle of the elementary surface is shown in figure IV.12.

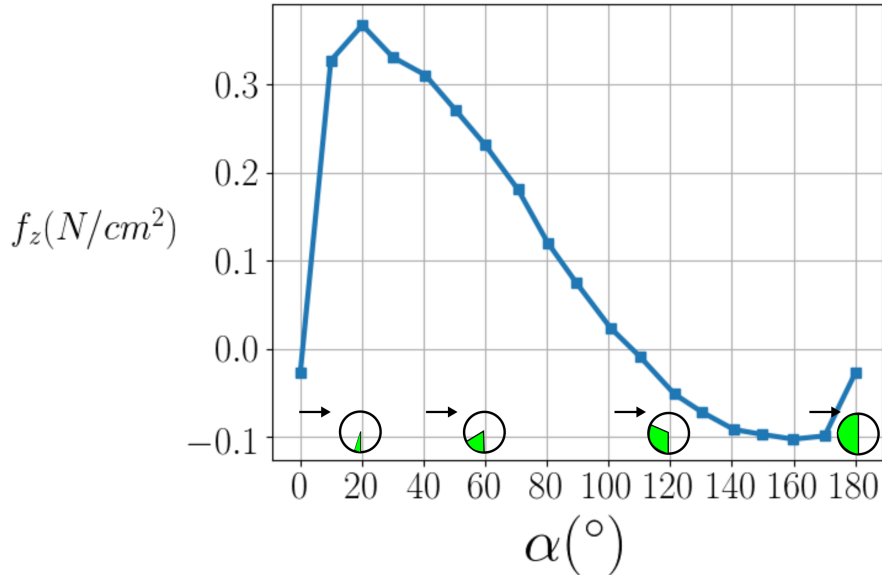


FIG. IV.12: Local vertical force measurement by Ding et al. (2011) for a circular intruder. Black arrows represent the front of the intruder. Green area represent the angle at which the constraint is measured.

One can see that the maximum of the lift force measured by Ding et al. (2011) is located at the bottom front of the intruder, for an angle of approximatively 20° . This value is very close to the angle found for the trajectory of our intruder ($\alpha = 19.3^\circ$), suggesting that both values could be linked. This angle could also correspond to the angle at which the green marker was observed to be a pivot point in figure IV.11b. This suggestion has to be taken cautiously since the configuration of Ding et al. (2011) is

different. Pulling an intruder in a granular media could induce a different circulation of the small particles around the intruder and the kinematics could be different.

In light of the mechanism we have observed and of our hypothesis concerning the size ratio dependency, we can discuss the concept of squeeze expulsion proposed by [Savage and Lun \(1988\)](#). In their experiments, [Savage and Lun \(1988\)](#) assumed that the squeeze expulsion mechanism counterbalanced kinetic sieving and was not size preferential. The process showed in figure [IV.11](#) suggests that the image of a large particle squeezed to the top by small particles is still valid: we observe that the segregation force on the intruder is related to an imbalance in the stress partitioning. This imbalance could develop an overpressure zone around the intruder pushing it to the top (as suggested by [Ding et al. \(2011\)](#) and [Guillard et al. \(2014\)](#)). In this way, it is as if the large particle would be squeezed upward.

However, as we proposed, the size ratio could influence the capacity of the intruder to be lifted. If our hypothesis is verified, in the future, it would imply that the size ratio plays a role in squeezing the intruder contrary to the idea of Savage and Lun (1988).

We believe that a thorough study of this mechanism, with access to the contact forces and the local velocity field of small particles, is necessary. It could allow us to understand how the large intruder modifies the local velocity profile and how it affects its dynamics. Then, it would be necessary to determine if the lift force proposed by [Guillard et al. \(2016\)](#) is accurate enough to model this process. If not, it would reveal that the segregation of a large intruder results from a more complex force. In the next section, we propose to ascertain if the lift force of [Guillard et al. \(2016\)](#) reproduces the linear trajectory with the constant slope. To do so, we compare the results of our Lagrangian model to our experiments.

IV.7.3 Assessing the particle-scale forces with our experiments

In section [II.1](#), a 2D dimensionless Lagrangian equation for a large intruder in a bed of small particles was presented. In this section, we propose to solve these equations with the inertial number I measured in our experiments and compare the results to our experimental data.

The 2D dimensionless equations are:

$$\frac{d\tilde{u}^l}{d\tilde{t}} = \frac{\tilde{u}^s - \tilde{u}^l}{St^p} \quad (\text{IV.6})$$

$$\frac{d\tilde{w}^l}{d\tilde{t}} + \frac{1}{St^p}\tilde{w}^l = -\mathcal{F}_l(\mu)\frac{\partial\tilde{p}^m}{\partial\tilde{z}} \quad (\text{IV.7})$$

where the shear stress gradient $\partial\tilde{\tau}^s/\partial\tilde{z}$ has been neglected since the slope of the flume is low ($\tan\theta = 10\%$). In addition, this low slope implies that $\cos\theta \sim 1$ and the dimensionless pressure gradient is written $\partial\tilde{p}^m/\partial\tilde{z} = \Phi^{max}(\rho^p - \rho^f)/\rho^p$. From equation [\(III.15\)](#), the granular Stokes number is $St^p = I/6c\mu\sqrt{\tilde{p}^m}$. The inertial number I will be computed thanks to image velocimetry processing. The friction coefficient μ will be

determined using the $\mu(I)$ relation (Jop et al., 2005):

$$\mu(I) = \mu_s + \frac{\mu_2 - \mu_s}{I_0/I + 1}, \quad (\text{IV.8})$$

with the coefficients proposed for turbulent bedload configurations by Maurin et al. (2016) $\mu_s = 0.35$, $\mu_2 = 0.97$ and $I_0 = 0.69$. Equation IV.8 predicts the friction coefficient μ to increase with the inertial number I in the liquid flow regime and to tend to $\mu_s = 0.34$ in the quasi-static regime. It is possible that the coefficients proposed by Maurin et al. (2016) differ in the case of our experiments due to sidewall effects. However, there is no mean to access the value of the friction coefficient in our experiment and thus, the coefficients from Maurin et al. (2016) are taken as a first approximation. Because the inertial number and the small particle velocity profile are exponential, there is no analytical solution for this set of equations and it is solved using a simple *odeint* solver with *Python*. The comparison is performed on the case $\tau^* = 0.25$ as the results are more repeatable. For each size ratio, a simulation is made with the initial depth chosen as the mean initial depth on the repetitions.

Figure IV.13 presents the results for the trajectory $z(x)$ and figure IV.14 the temporal results $z(t)$. The blue crosses are the results of equations (IV.6) and (IV.7) with \mathcal{F}_l and c proposed by Guillard et al. (2016) and Tripathi and Khakhar (2013), mentioned in section II: the empirical segregation function is $\mathcal{F}_l(\mu) = 1 - \exp(-70(\mu - \mu_c))$ and the granular drag coefficient is $c = 3$.

In figure IV.13 one can see that the model predicts a non-linear trajectory whereas the trajectory observed in the experiments was linear. Looking at figure IV.14, the temporal curve looks similar to the experimental ones but the order of magnitude for the segregation duration is always shorter. Note that there is no size ratio dependency in equations (IV.6) and (IV.7) so the model predicts the same behaviour for each configuration. The only possible variation between configurations is due to the variability on the measurement of the inertial number with image processing.

In section III.4.2, theoretical and numerical investigations have shown that the granular drag coefficient could be written $c(\phi^s) = 3(1 + 28\phi^s/3)$ and thus should be equal to 31 when there is only one large intruder (i.e. $\phi^s \rightarrow 1$). In addition, a new formulation for the empirical segregation function was proposed as:

$$\mathcal{F}_l(\tilde{p}^m, \phi^s) = \mathcal{F}_0 c(\phi^s) \tilde{p}^m, \quad (\text{IV.9})$$

where $\mathcal{F}_0 = 6S_{r0}\rho^p / (C_0\Phi(\rho^p - \rho^f))$, with S_{r0} being a constant and $C_0 = \sqrt{\tilde{p}^m} I^{0.15} / \mu$. The results obtained with these closures are presented in figures IV.13 and IV.14 with $S_{r0} = 0.005$ (see equation III.4). In figure IV.13, it is interesting to see that the linear trajectory is recovered. However, the slope does not match the average slope obtained in our experiments. We observed that varying the value of the drag coefficient did not change neither the linear behaviour nor the value of the slope.

This result demonstrates that the dependencies in the empirical segregation function \mathcal{F}_l play an essential role in the modeling of the spatial behaviour of the intruder. It is therefore essential to characterise in detail the form of this function.

In figure IV.14, the predicted vertical position with time shows a good agreement with the repetitions for $r = 2.5$, suggesting that the vertical equation of the model is able to capture the accurate dynamics on the vertical axis. For $r = 3$ the agreement is also

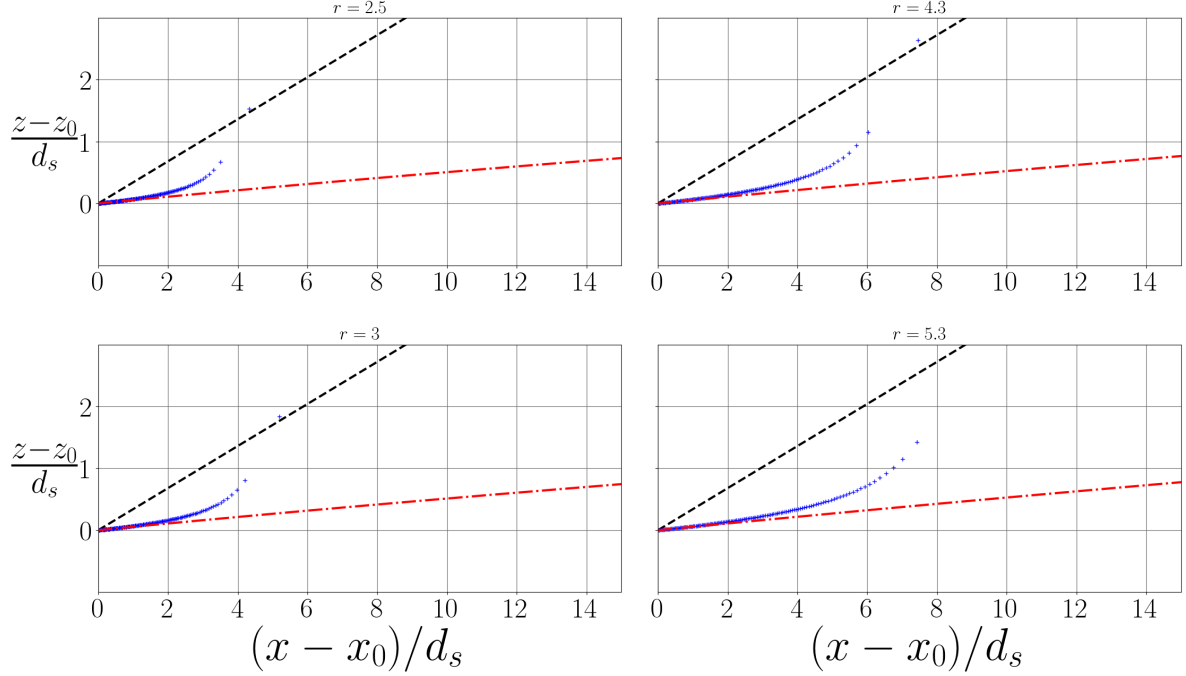


FIG. IV.13: Trajectory $z(x)$ of the intruder predicted by our model with the closures of Guillard et al. (2016) and Tripathi and Khakhar (2013) (+) and the results with the new closures proposed in section III.4.2 (---). The average trajectory measured in our experiments is the black dashed line (----).

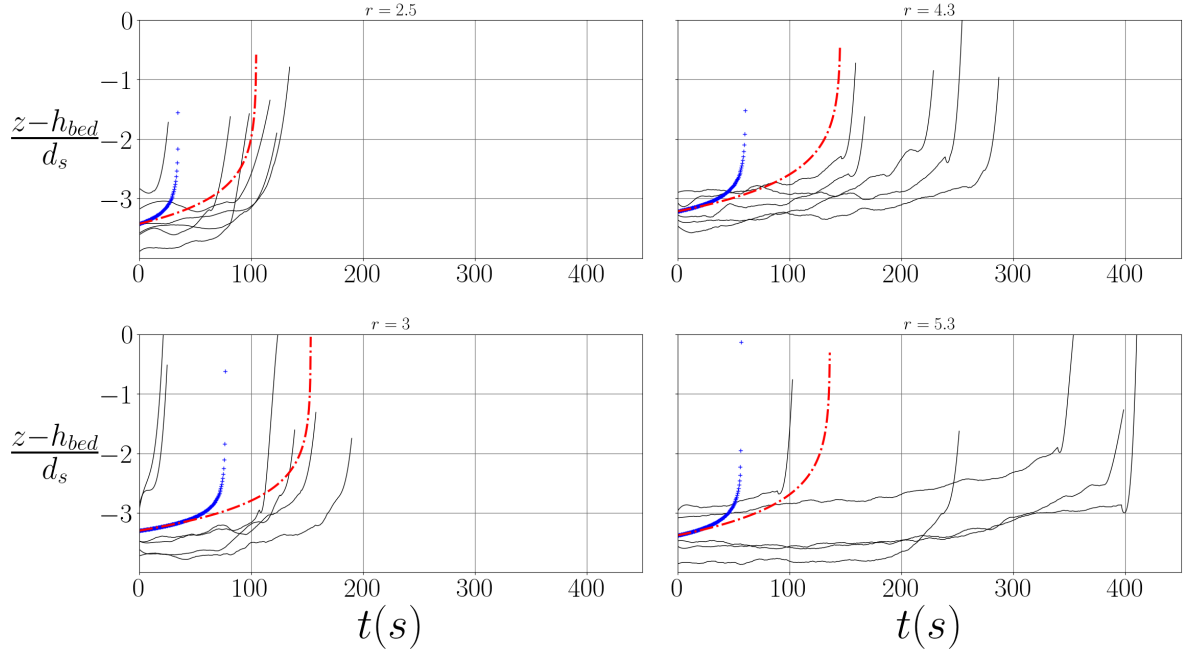


FIG. IV.14: Position of the center of the intruder with time $z(t)$ for the experiments (—), the model with the closures of Guillard et al. (2016) and Tripathi and Khakhar (2013) (+) and the results with the new closures proposed in section III.4.2 (---)

satisfying. However, for higher size ratios the model does not predict the increase of the segregation duration suggesting that a size ratio dependency is missing in our equations.

The equation on the vertical axis (IV.7) shows that at first order, the behaviour of the intruder is accurately modeled. Nevertheless, the lower slope in the trajectory shows that the advection predicted by the model is too strong in the streamwise direction. In other words, equation (IV.6) does not correctly counterbalance the vertical equation (IV.7). First, we added a force to model the effect of sidewalls on the intruder but it revealed that it has no impact on the intruder. This is probably due to sidewall effects already taken into account in the measured particle bed velocity profile used to compute the inertial number.

[Guillard et al. \(2014\)](#) reported that for an intruder pulled in a granular media : “the angular stress distribution on the obstacle is the sum of a symmetric part proportional to the mean pressure or equivalently to the depth, which is responsible for the drag force but do not contribute to the lift, and a asymmetric part which does not depend on the mean pressure and induces lift.” We believe that in the streamwise direction, the drag force from [Tripathi and Khakhar \(2013\)](#) arises from the mean pressure around the intruder but an additional force to model the effect of asymmetric stress in the streamwise direction is needed. From the observation in figure IV.11b, this asymmetric stress could be due to the presence of small particles at the bottom front of the intruder, preventing it to move relatively to the granular bed. We propose to model this phenomenon by adding a drift velocity in the streamwise equation of the intruder. This drift velocity is proposed to be $\beta \tilde{u}^s / St^p$ with β a parameter to be fitted on our experimental trajectory. The set of equation now reads

$$\frac{d\tilde{u}^l}{d\tilde{t}} = \frac{\tilde{u}^s - \tilde{u}^l}{St^p} - \beta \frac{\tilde{u}^s}{St^p} \quad (\text{IV.10})$$

$$\frac{d\tilde{w}^l}{d\tilde{t}} + \frac{1}{St^p} \tilde{w}^l = -\mathcal{F}_l(\tilde{p}^m, \phi^s) \frac{\partial \tilde{p}^s}{\partial \tilde{z}} \quad (\text{IV.11})$$

with the empirical segregation function expressed in (IV.9) and $c = 31$.

With $\beta = 0.9$, the trajectory obtained with these equations (figure IV.15) show good agreement with the average experimental trajectories found in our experiments.

This proposition is not physically based but it shows that further investigations should be performed to model the forces acting on the intruder in the streamwise direction. It should be noted that in our equations, the empirical segregation function is based on our numerical analysis in section III.4 and no experiments have validated this closure in the case of a single large particle. Change in the formulations of these parameters could also impact the trajectory of the intruder.

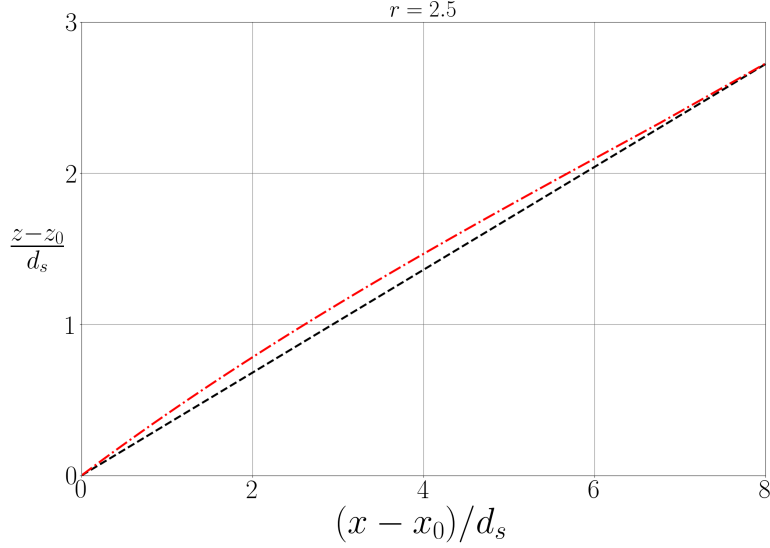


FIG. IV.15: Trajectory of the intruder obtained with equations (IV.10) and (IV.11) (----). The average trajectory measured in our experiments is the black dashed line (---).

IV.8 Conclusion

In this chapter, we have reported laboratory experiments of a single large particle segregating in bedload transport. Thanks to these experiments, it was possible to better understand the mechanisms at play during the segregation of a large particle. We found that a minimum of segregation duration was found around a size ratio $r = 2$, confirming the results of [Golick and Daniels \(2009\)](#); [Guillard et al. \(2016\)](#) and [Jing et al. \(2020\)](#) in other configurations.

In addition, a surprising behaviour was observed. The trajectory of the intruder was found to be linear with a constant slope. A detailed observation of the experiments allowed us to understand the potential origin of the linear trajectory. Finally, we compared our experiments to the results of our Lagrangian equation, the starting point of our upscaling development. This equation seems to be valid at first order to model the segregation of an intruder in bedload transport. It allowed us to highlight the key parameters that should be investigated in the future for a better prediction. The form of the empirical segregation function of [Guillard et al. \(2016\)](#) plays an essential role in the linearity of the trajectory and it would be necessary to refine it. Finally, a better comprehension of the effects acting on the streamwise direction should also enhance prediction.

CHAPITRE V

CONCLUSIONS & PERSPECTIVES

Polydispersity in granular flows can lead to grain-size sorting. In bedload transport, this is responsible for the modification of the sediment rate as well as to the creation of river scale geomorphological patterns. It was identified that these effects could be better predicted by modeling the underlying physical processes at the granular scale into larger scale models. In this PhD thesis, we addressed this issue by deriving a theoretical model starting from the granular scale forces and providing a simple continuum equation for the prediction of vertical concentration and velocity profiles of a bidisperse granular bed in bedload transport. In addition, the behaviour of a large particle segregating among smaller particles in bedload transport was investigated experimentally. This gives new insights on the phenomena and yields data to assess the theoretical model proposed. In this section, we summarise the advances provided by our work and we outline the perspectives.

V.1 Conclusions

As a first step, we developed a theoretical approach to bridge the gap between the size segregation mechanism at the granular scale and its continuum modeling. It was developed for a bidisperse bed of particles sheared by the water flow. The originality of this work was to propose a new multiphase flow approach, derived from a volume averaging method, based on the most recent advances on particle-particle forces, namely the segregation force or lift force from [Guillard et al. \(2016\)](#) and the drag force from [Tripathi and Khakhar \(2013\)](#). The proposed multi-phase flow model formulation is general enough to be applied to any immersed granular flow configuration.

This model was solved numerically in 1D, in the vertical direction, in order to highlight the key physical closures to accurately predict size-segregation. However, the full 3D equations were also provided and their implementation should be possible. The numerical algorithm to solve the 1D vertical model was developed in this PhD and was inspired by [Chauchat et al. \(2017\)](#).

Following the same procedure as in [Thornton et al. \(2006\)](#), an advection-diffusion model was derived from the multi-phase flow equations. This derivation allowed us to identify the dependencies of the advection and diffusion coefficients on the local physical

parameters of the flow such as the volume fraction of small particles, the mixture granular pressure and its gradient, the granular Stokes number and the segregation parameters.

Both models have been tested against Discrete Element Model (DEM) simulations of Chassagne et al. (2020b) for bidisperse turbulent bedload transport. Without any tuning of the forces from Guillard et al. (2016) and Tripathi and Khakhar (2013), both continuum models qualitatively reproduce the main features of size segregation. This demonstrates that the scaling of the advection coefficient with the inertial number observed by Fry et al. (2018) and Chassagne et al. (2020b) can be explained thanks to the dependency of the advection coefficient on the granular Stokes number and the underlying presence of the granular viscosity. Using the DEM results, improved parametrisations for the advection and diffusion coefficients were proposed. They suggest that the empirical segregation function from Guillard et al. (2016) and the drag coefficient from Tripathi and Khakhar (2013) should incorporate a dependency on the small particle concentration. Finally, a dependency of the segregation function on the size ratio was proposed.

The second step consisted in the experimental investigation of the behaviour of a single large particle in bedload transport was investigated experimentally in a flume, for different initial depths, for two different Shields numbers and for different size ratios. The intruder was tracked using an algorithm developed by Lafaye de Micheaux et al. (2018) which enabled us to measure the position and the velocity of the large particle during the experiment. The *OpyFlow* toolbox developed in the PhD thesis of Rousseau (2019) was adapted to our experiment to measure the velocity, the shear rate and the viscosity of the granular bed.

Results of the experiment showed that the intruder rose upward with time, as expected. The intruder displayed two regimes when segregating. At the beginning, a slow ascent regime, occasionally affected by caging effects, was observed. The duration of this regime was shown to vary significantly between the repetitions. For configurations where the intruders initial depth was in the liquid flow, this regime was not observed. By contrast, a second regime characterised by an abrupt acceleration was observed for all the repetitions. In all of the experiments it was found that for a given Shields number and for a given size ratio, the kinematics of the intruder in the accelerating regime was the same whatever the initial depth. Therefore, the segregation duration essentially depended on the first regime. This regime seemed to be influenced by the Shields number, the aspect ratio and the size ratio.

More generally, the segregation duration was found to depend on the size ratio. Above a size ratio $r = 2$, for both Shields numbers, the segregation duration was found to increase monotonically. We were able to provide data varying between $r = 1$ and $r = 2$ only for the lowest Shields number. It was observed that when approaching $r = 2$, the segregation duration had a tendency to diminish. This would correspond to previous works (Golick and Daniels, 2009; Guillard et al., 2016; Jing et al., 2020), which evidenced a minimum segregation duration for a rising large intruder, for a size ratio around $r = 2$.

The trajectory of the intruder was also studied by investigating the vertical displacement as a function of the streamwise displacement. For size ratios above $r = 1.7$,

whatever the initial depth, the size ratio or the Shields number, it was observed that the trajectory was linear with a universal constant slope. This dynamics was linked to the visual observations of the experimental images. The intruder tends to be blocked by small particles located at the bottom front of the intruder while small particles at the rear of the intruder move under it, pushing it upward. Above $r = 2.5$, the segregation duration was found to increase. We believe that the described mechanism is still present but less efficient due to a mass effect. Indeed, when the size ratio increases, the small particles moving down transmit less momentum to the intruder as they become smaller while the larger intruder would require more momentum to rise.

Our original experiments provided a dataset to assess the Lagrangian model of section II.1 which represents the starting point of our theoretical development. With the original parameters from [Guillard et al. \(2016\)](#) and [Tripathi and Khakhar \(2013\)](#), the kinematics of the intruder can be qualitatively predicted but the segregation duration was lower and the linear trajectory was not found. Then, we compared the results with the new closures fitted on the DEM (see section III.4). The segregation duration was closer to the one obtained in the experiments, particularly for the size ratio $r = 2.5$. More interestingly, the linear trajectory was recovered. We found that the shape of the trajectory was determined by the empirical segregation function from [Guillard et al. \(2016\)](#). Indeed, the additional parameters we investigated in section III.4 for this function are essential to predict the linear trajectory.

Nevertheless, the predicted slope was still lower than in our experimental dataset. We found that it could potentially originate from missing forces in the streamwise equation of the intruder. We showed that a drift velocity allows recovering the accurate slope of the intruder trajectory and therefore, we highlighted the necessity to investigate in more details the modeling of the intruder dynamics in the streamwise direction.

V.2 Perspectives

In terms of perspectives for granular flows, the continuum models proposed herein are very general and should as well be applicable to dense dry granular flows. These models represent a general framework for developing and testing improved parametrisations for the segregation and granular drag forces in different flow configurations. Despite this progress, further investigations are needed to improve the closures we proposed. The implementation of the model in 3D and its coupling with river scale model should also be addressed. Lastly, the generalisation of the model to more than two sizes of particles is still an open question.

The experimental work identified new perspectives on the dynamics of the intruder and its modeling but further experiments have to be carried out to bring a full understanding on what we observed and would require more accurate measurements.

V.2.1 Refining closures for granular scale forces

Closures from [Tripathi and Khakhar \(2013\)](#) and [Guillard et al. \(2016\)](#)

Through this PhD work, we saw that the drag and the segregation forces proposed by [Guillard et al. \(2016\)](#) and [Tripathi and Khakhar \(2013\)](#) were appropriate for the

modeling of grain-size segregation. In addition, in section IV.7.2 we observed that the form of the empirical segregation function was decisive for accurately predicting the dynamical behaviour of the intruder. Therefore we believe that it is necessary to keep using those forces while trying to improve their parametrisation. We should also keep questioning their validity in different configurations. Particularly, we saw that the empirical segregation function in the segregation force of [Guillard et al. \(2016\)](#) and the drag coefficient in the drag force of [Tripathi and Khakhar \(2013\)](#) were incomplete. We proposed new formulations for these coefficients based on fits on the DEM simulations of [Chassagne et al. \(2020b\)](#). Yet, it did not allow us to propose formulations that are physically based. In addition, we could not find the origin of the need for additional dependencies. Does it stem from the upscaling to numerous particles or the bedload configuration or are the parametrisations from [Guillard et al. \(2016\)](#) and [Tripathi and Khakhar \(2013\)](#) incomplete?

Concerning the drag coefficient, [Tripathi and Khakhar \(2013\)](#) already suggested that it should depend on the local volume fraction. In a bidisperse case, we showed that it should depend on the local volume fraction of small particles as

$$c(\phi^s) = 3 \left(1 + \frac{28}{3} \phi^s \right). \quad (\text{V.1})$$

With this notation, the value proposed by [Tripathi and Khakhar \(2013\)](#) is recovered when ϕ^s tends to zero (one small particle percolating into a matrix of larger particles) and the drag coefficient increases to 31 when ϕ^s tends to 1 (one large particle in a matrix of small particles). Our experiments on a single intruder showed that the value $c = 31$ provided better results in the model for the large intruder, showing that the parametrisation (V.1) works for a large particle segregating upward. This is not enough to fully validate formulation (V.1). Additional efforts on the granular drag force on a single intruder should be developed to validate the maximum and minimum values of formulation (V.1) and their validity in other configurations, such as dry granular flows, simple shear or dense segregation. The concentration dependency should also be tested against experiments in bidisperse granular flows.

Concerning the empirical segregation function, we showed that it could be written as

$$\mathcal{F}_l(\tilde{p}^m, \phi^s) = \mathcal{F}_0 c(\phi^s) \tilde{p}^m, \quad (\text{V.2})$$

where $\mathcal{F}_0 = 6S_{r0}\rho^p / (C_0\Phi(\rho^p - \rho^f))$, S_{r0} and C_0 being constant which could vary with the configurations. Our work highlighted potential missing dependencies but further work should be carried out to understand the origin of this empirical segregation function. It could help assess our formulation in more general configurations or provide a formulation with the relevant parameters to describe the lift of a single large particle. One could also identify whether the ϕ^s dependency stems for the presence of numerous large particles.

It should be noted that [Van der Vaart et al. \(2018\)](#) proposed that the lift force originates in a granular Saffman effect, providing a theoretical framework for the origin of the lift force. Bridging the gap between this modified Saffman force and the force of [Guillard et al. \(2016\)](#) could possibly help formulate theoretically the empirical segregation function.

Closure for the granular pressure

Another question lies in the definition of the granular pressure. In this work, the pressure on each phase is defined as

$$p^i = \phi^i p^m.$$

This raises two questions. First, from [Tunuguntla, D. R. and Thornton, A. R. \(2017\)](#), this definition is valid as long as concentration between each size of particles are of the same order. However, it is no longer accurate when the concentrations are too different. The continuum model we proposed is therefore only valid as long as this definition of the pressure is valid. The mechanisms of pressure distribution between each phase has to be studied.

Secondly, this definition of the pressure was responsible for the diffusion coefficient. Indeed, in section [II.3](#), we saw that the gradient of this pressure creates the additional term $\tilde{p}^m \partial \phi^s / \partial \tilde{z}$ in the small particle momentum conservation equation which is responsible for the diffusion coefficient in the advection-diffusion equation. Diffusion is usually seen as a stochastic process involving the random behaviour of a single particle amidst the others. It would be interesting to see if this term created by the partial pressure is representative of such stochastic behaviour or if it has to do with another kind of diffusion linked to the behaviour of a collection of particles.

Size ratio dependency

In this PhD thesis, the size ratio dependency in the different closures was somewhat put aside. Nevertheless, in the future, this dependency needs to be integrated to provide more precise predictions.

In section [III.4](#), it was briefly investigated by adding the dependency found by [Chassagne et al. \(2020b\)](#) into the advection coefficient. This dependency was found by analysing the segregation velocity of a layer of small particles and increased exponentially with the size ratio r . On the contrary, in the context of large particles, our experiments and the works of [Golick and Daniels \(2009\)](#); [Guillard et al. \(2016\)](#); [Jing et al. \(2020\)](#) showed a maximum around $r = 2$. This difference could originate from the asymmetry of velocities between small and large particles. It could show that the driving mechanism between both sizes of particle is different. Such an idea should be investigated in the future. Concerning the segregation force determined for a large particle, it would be of great interest to propose a force based on the model of [Guillard et al. \(2016\)](#) that would contain dependencies both on the rheological parameters and on the size ratio. We found with our experiments that the segregation velocity seems to be maximum around $r = 2$. However, there is a subtlety with the works of [Guillard et al. \(2016\)](#) and [Jing et al. \(2020\)](#): the maximum they found for $r = 2$ concerned the segregation force. Does it mean that the dependency on size ratio in the segregation velocity is only given by the dependency in the segregation force?

V.2.2 Upscaling size segregation

Concerning the upscaling of size segregation processes in sediment transport applications two routes are opened. The first one consists in implementing the proposed

multi-phase flow model in a 3D numerical model, such as sedFOAM ([Chauchat et al., 2017](#)), for the simulation of size segregation in complex sediment transport application such as riverbed armouring ([Frey and Church, 2009](#)), scour around an hydraulic structure ([Nagel et al., 2020](#)) or wave-driven sediment transport involving sand mixtures ([O'Donoghue and Wright, 2004](#)).

The second route would be to couple the advection-diffusion model with a shallow water model for the fluid flow. Such a model would make it possible to address size segregation at the river scale while taking into account granular scale processes in a physically consistent way ([Woodhouse et al., 2012](#); [Denissen et al., 2019](#)).

It should be noted that both perspectives are subject to the ability to predict accurately the deformations in the dense and the quasi-static regimes. In the dense regime, the $\mu(I)$ rheology was shown to provide accurate results ([Maurin et al., 2016](#)). In the quasi static regime a model that is able to predict non-local rearrangement would be necessary. [Kamrin and Koval \(2012\)](#) proposed such a model and it could be interesting to adapt it to a bedload configuration. Then, both models should be connected to provide the rheology on the entire bed.

Another perspective regarding the generalisation of our work concerns the size repartition. For the purpose of this PhD thesis, the model was developed for two different particle sizes. However, in rivers, the granular bed is usually made of a broad size distribution. It is therefore necessary, to generalise our multi-phase flow model to a larger size repartition. Such a derivation becomes harder as granular phases are added because one must identify the forces acting between the different phases in the momentum conservation equation. We found no trivial relation between the number of phase and the closures for the momentum conservation equations that would make the model easily generalisable.

We think that a limited number of particle size classes could be representative of the granular bed and therefore efficient for an accurate prediction of size repartitions. This hypothesis should be investigated in the future.

V.2.3 Refining experiments on a single intruder

In this PhD thesis, we performed new experiments on a large particle segregating in bedload transport. These experiments provided data to validate and improve the Lagrangian equation, proposed in chapter [II](#), which is the sarting point for the continuum modeling proposed in this work. It also opened new perspectives for the understanding of the segregation mechanism. However, the set-up presented in chapter [IV](#) limited the range of accessible parameters and influenced the dynamics of the intruder.

A possibility would be to increase the width of the flume. There would be less energy dissipation on the sidewalls and one could perform experiments on a larger range of Shields numbers and aspect ratios. It would diminish the impact of the sidewalls on the behaviour of the intruder and confirm the linear trajectory.

Nevertheless, when increasing the width of the flume one would face the constraints

linked to the detection of the intruder, identified in chapter IV. Indeed, we saw that when the diameter was not sufficiently large compared to the width of the flume, the intruder was hidden by the small particles hampering tracking. To keep the intruder visible, we were obliged to perform experiments at low aspect ratios or to place the intruder against the sidewall, potentially modifying its dynamics due to the friction with the wall (and providing a configuration which is not fully 3D). A solution to tackle this obstacle would be to adjust the refractive index of the fluid to the one of the small particles. Such a method, known as refractive index matching (Aussillous et al., 2013; Ni and Capart, 2015; Rousseau and Ancey, 2020), provides a transparent medium and one could therefore follow the intruder through the granular matrix whatever its position. A refractive index method combined with a laser sheet may also track the dynamics of the intruder in the transverse direction. In addition, it could be possible to map the local layout of the small particles around the intruder. This could give supplementary information on the role of the small particles in the neighbourhood of the intruder. In particular, the number of contact and how it evolves with the size ratio would also be accessible.

Setting such index matching experiments is, in our opinion, very challenging but could provide data with a high value.

V.2.4 DEM simulations

An easier possibility would be to perform DEM simulations of a large intruder segregating in a bedload configuration. One could be more precise on the initial conditions and on the measurements while exploring a large number of repetitions as well as a large range of size ratios and Shields numbers. It would provide data to perform a statistical analysis on the intruder.

Discrete simulations would also give access to better estimations of the concentration, solid pressure, shear stress and shear rate profiles. These fields are necessary to determine the granular viscosity and the inertial number with a higher precision than in experiments and identify physical dependencies more clearly.

As an opening for future works and thanks to Rémi Chassagne and the internship of Robin Jager, such DEM simulations have been performed for a Shields number $Sh = 0.2$, for $r = 2$ and in a 3D configuration (without sidewalls). These first results are very promising. First, figure V.1 shows the depth of the center of the intruder with time. It can be seen that the segregation of the intruder with two different stages is recovered. As observed in our experiments, even with DEM simulations, the behaviour of the intruder with time is poorly repeatable in the first stage of the ascent. This could allow one to study in more details the physics at play during this stage. Secondly, in figure V.2 we observe that the linear trajectory of the intruder is recovered. It gives confidence that the linear trajectory we observed in our set-up was not an artefact. The slope is also found to be constant which could make it possible to generalise our hypothesis concerning the mechanism observed in figure IV.11b. Nevertheless, the slope is lower than in our experiments. Further studies have to be carried out to identify the reason.

Lastly, since DEM simulations give access to particle kinematics and contact forces

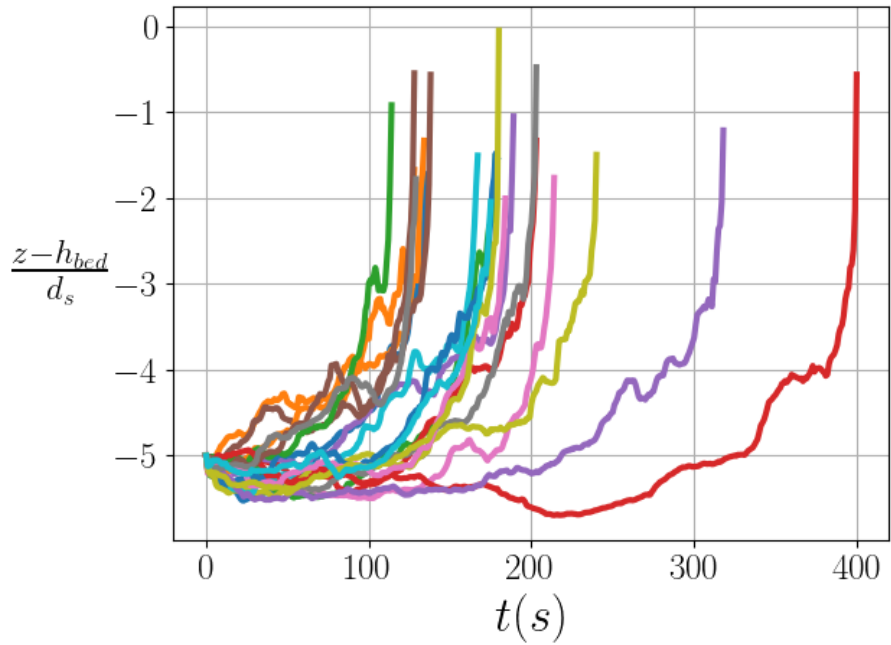


FIG. V.1: Vertical position of the center of the intruders with time obtained with DEM simulations. Size ratio $r = 2$ and Shields number $Sh = 0.2$.

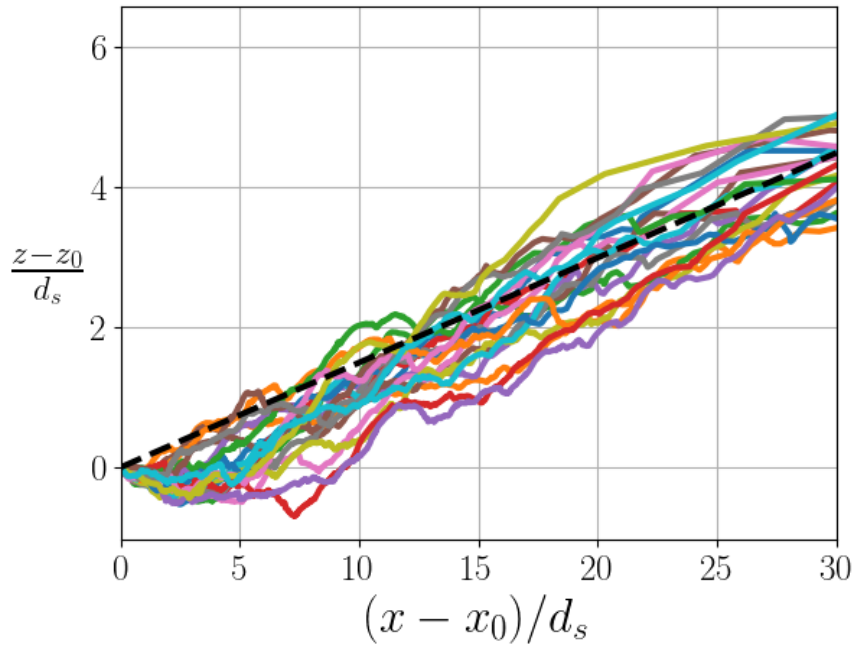


FIG. V.2: Trajectory of the intruders obtained with DEM simulations. Size ratio $r = 2$ and Shields number $Sh = 0.2$. x_0 and z_0 are initial positions and the black dashed line (----) is the mean slope.

surrounding the intruder, one could understand how the large intruder modifies the flow of small particles and how it affects the behaviour of the intruder. It could shed light on the linear ascent and improve the modeling of size segregation.

ANNEXE A

NUMERICAL SCHEME FOR THE MULTI-PHASE FLOW MODEL

In this appendix we present the discretisation of the mass and momentum conservation equations as well as the implementation of the PISO algorithm. The discretisation process is shown for the mixture phase as an example. Then, from the discretised equations, we show how the velocity of each phase are predicted using the PISO algorithm. Finally, we present the Poisson equation to solve the fluid pressure and the corrector step for the velocities.

A.1 Discretisation for the mixture

In order to be solved numerically, the equations of the different phases need to be discretised on the mesh presented in figure A.1. This is done using the finite volume method on a regular mesh made of N volumes. Because the system is one dimensional, these volumes reduce to cells of size Δz . The velocities, the pressures and the volume fractions are solved for each cells j of the mesh. The velocities $\{w^f\}_j$, $\{w^m\}_j$ and $\{w^s\}_j$ are located at the cell faces while the scalar quantities such as volume fractions $\{\Phi\}_j$, $\{\Phi^s\}_j$ and pressures $\{p^f\}_j$, $\{p^m\}_j$ are located at the cell centers. Knowing $\{\Phi\}_j^n$, $\{\Phi^s\}_j^n$, $\{\Phi^l\}_j^n$, $\{\epsilon\}_j^n$, $\{w^m\}_j^n$, $\{w^s\}_j^n$, $\{w^f\}_j^n$ and $\{w^l\}_j^n$ at cell j , at time n , these values are solved to find them at time $n + 1$.

From section II.2.4, the equations that need to be solved are:

- the mixture (small and large particles) and small particle phase mass equations:

$$\frac{\partial \Phi}{\partial t} + \frac{\partial \Phi w^m}{\partial z} = 0, \quad (\text{A.1})$$

$$\frac{\partial \Phi^s}{\partial t} + \frac{\partial \Phi^s w^s}{\partial z} = 0. \quad (\text{A.2})$$

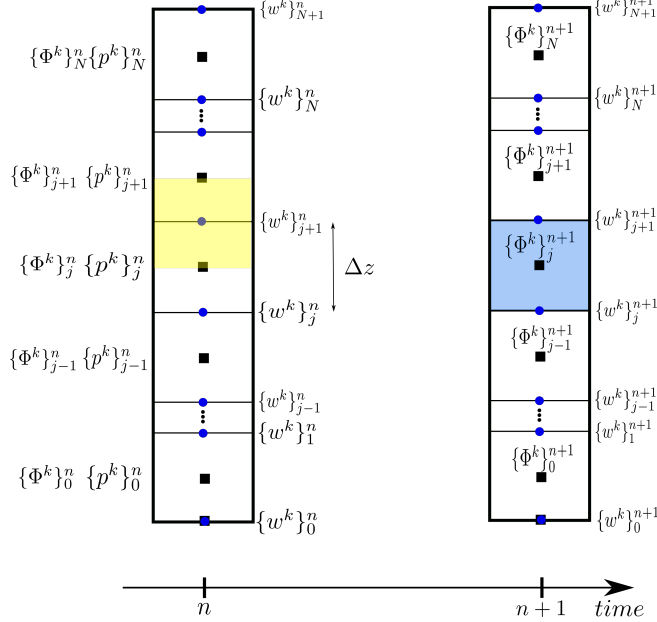


FIG. A.1: The whole domain is meshed in N cells of size Δz for each timestep n . The scalar values such as the volume fractions Φ^k and the pressures p^k are defined at the center of the cells. The velocity vectors w^k are defined at the faces of the cells. The yellow surface represents the j^{th} control volume on which the scalar values are integrated. The blue surface represents the j^{th} control volume on which the velocity fluxes are integrated.

– the momentum equations for the mixture, the small particle and the fluid phases:

$$\begin{aligned} \frac{\partial w^m}{\partial t} + w^m \frac{\partial w^m}{\partial z} + \frac{1}{t_l} w^m = & -\frac{1}{\rho^p \Phi} \frac{\partial p^m}{\partial z} - \frac{1}{\rho^p} \frac{\partial \bar{p}^f}{\partial z} - \left(1 - \frac{\rho^f}{\rho^p}\right) g \cos \theta \\ & + \frac{1}{\Phi} \left(\frac{\Phi^l}{t_l} + \frac{\Phi^s}{t_s}\right) w^f + \frac{\Phi^s}{\Phi} \left(\frac{1}{t_l} - \frac{1}{t_s}\right) w^s, \end{aligned} \quad (\text{A.3})$$

$$\begin{aligned} \frac{\partial w^s}{\partial t} + w^s \frac{\partial w^s}{\partial z} + \left(\frac{1}{t_s} + \frac{\Phi}{t_{ls}}\right) w^s = & -\frac{1}{\rho^p \Phi^s} \frac{\partial p^s}{\partial z} - \frac{1}{\rho^p} \frac{\partial \bar{p}^f}{\partial z} - \left(1 - \frac{\rho^f}{\rho^p}\right) g \cos \theta \\ & + \frac{1}{t_{ls}} w^f + \frac{\Phi}{t_{ls}} w^m + \frac{\Phi^l}{\Phi^s \rho^p} \mathcal{F}(\mu) \frac{\partial p^m}{\partial z}, \end{aligned} \quad (\text{A.4})$$

$$\begin{aligned} \frac{\partial \epsilon w^f}{\partial t} + w^f \frac{\partial \epsilon w^f}{\partial z} + \left(\frac{\rho^p \Phi^s}{\rho^f \epsilon t_s} + \frac{\rho^p \Phi^l}{\rho^f \epsilon t_l}\right) w^f = & -\frac{1}{\rho^p} \frac{\partial \bar{p}^f}{\partial z} \\ & - \frac{\rho^p \Phi^s}{\rho^f \epsilon} \left(\frac{1}{t_s} - \frac{1}{t_l}\right) w^s + \frac{\rho^p \Phi}{\rho^f \epsilon t_l} w^m. \end{aligned} \quad (\text{A.5})$$

In this paragraph, the method to discretise the mass and momentum conservation equations is presented. For the sake of simplicity, the process is only shown for the mass and momentum equations (A.1) and (A.3), describing the mixture phase. Note that other equations follow the same process.

A.1.1 Discretisation of the mixture mass conservation equation

The mass equation (A.1) is integrated in time between n and $n + 1$ and in space between cell j and cell $j + 1$:

$$\int_{t^n}^{t^{n+1}} \int_{z_j}^{z_{j+1}} \left[\frac{\partial \Phi}{\partial t} + \frac{\partial \Phi w^m}{\partial z} \right] dz dt = 0, \quad (\text{A.6})$$

$$(\Phi_j^{n+1} - \Phi_j^n) \Delta z + (w^m \Phi|_N - w^m \Phi|_S) \Delta t = 0, \quad (\text{A.7})$$

The terms $w^m \Phi|_N$ and $w^m \Phi|_S$ represent the convection fluxes at the North and South interfaces of the scalar control volume as shown in the middle panel of figure II.3. A simple first order upwind convection scheme is used and provides the discretised mass conservation equation for the mixture phase:

$$a_S^\Phi \Phi_{j-1}^{n+1} + a_P^\Phi \Phi_j^{n+1} + a_N^\Phi \Phi_{j+1}^{n+1} = H^\Phi, \quad (\text{A.8})$$

where

$$F_S = w_j^m \Delta t / \Delta z \quad \text{and} \quad F_N = w_{j+1}^m \Delta t / \Delta z$$

are the convection fluxes and

$$a_S^\Phi = -\max(F_S, 0) \quad (\text{A.9})$$

$$a_N^\Phi = -\max(-F_N, 0)$$

$$a_P^\Phi = -(a_S^\Phi + a_N^\Phi).$$

$$(\text{A.10})$$

The source term H^Φ reads $H^\Phi = \Phi_j^n$. At the top ($j = N + 1$), the boundary conditions are

$$\frac{d\Phi}{dz} = 0 \quad ; \quad a_S^\Phi = -1 \quad ; \quad a_P^\Phi = 1 \quad ; \quad H^\Phi = 0$$

while at the bottom ($j = 0$), the boundary conditions are

$$F_S = 0 \quad ; \quad F_N = w_1^m \Delta t / (\Delta z / 2) \quad ; \quad H^\Phi = \Phi_0^n$$

The solution of the algebraic system (A.8) provides the solution vector $\{\Phi\}_j^{n+1}$.

A.1.2 Discretisation of the mixture momentum conservation equation

The integration of the momentum equation (A.3) with a first order Euler scheme for the time derivative and a first order upwind scheme for the space derivative gives

$$[A^m]_{jk} \{w^m\}_k^* = \{H^m\}_j - [A^{mf}]_{jk} \{w^f\}_k^* - [A^{ms}]_j \{w^s\}_j^* - \frac{1}{\rho^p} \frac{\partial \{p_f\}_j^*}{\partial z} \quad (\text{A.11})$$

In this equation the index j represents the j^{st} grid node in the mesh. $[A^m]$ is a tridiagonal matrix which contains implicit advection and drag terms (terms solved for $t = n + 1$). The coefficients are given by

$$\begin{aligned} a_S^m \{w^m\}_{j-1}^n + a_P^m \{w^m\}_j^n + a_N^m \{w^m\}_{j+1}^n = \\ \{H^m\}_j - [A^{mf}]_{jk} \{w^f\}_k^* - [A^{ms}]_j \{w^s\}_j^* - \frac{1}{\rho^p} \frac{\partial \{p_f\}_j^*}{\partial z}, \end{aligned} \quad (\text{A.12})$$

We define the convection fluxes as:

$$F_S = 0.5(\{w^m\}_j^n + \{w^m\}_{j-1}^n) \Delta t / \Delta z ; \quad F_N = 0.5(\{w^m\}_j^n + \{w^m\}_{j+1}^n) \Delta t / \Delta z$$

giving

$$\begin{aligned} a_S^m &= -\max(F_S, 0) \\ a_N^m &= -\max(-F_N, 0) \\ a_P^m &= -(a_S^m + a_N^m) \end{aligned}$$

$\{H^m\}$ contains explicit source terms (terms solved for $t = n$) including temporal derivative, gravity, explicit drag term (mixture phase contribution) and reads

$$\{H^m\}_j = \{w^m\}_j^n - \frac{\Delta t}{\rho^p \{\Phi^w\}_j^{n+1}} \frac{\{p^m\}_j^{n+1} - \{p^m\}_{j-1}^{n+1}}{\Delta z} - \Delta t \left(1 - \frac{\rho^f}{\rho^p} \right) g.$$

Since the velocities are defined on the faces of each cell, the volume fraction Φ_j^w , is the mixture volume fraction at the face of cell j . It is obtained by interpolation as

$$\{\Phi^w\}_j^{n+1} = 0.5(\{\Phi\}_j^{n+1} + \{\Phi\}_{j-1}^{n+1}).$$

$[A^{mf}]$ and $[A^{ms}]$, the coupling matrix, are diagonal matrix containing respectively the explicit drag term coming from the fluid phase and the small particle phase:

$$\begin{aligned} [A^{mf}]_{jj} &= -\frac{\Delta t}{\{\Phi^w\}_j^{n+1}} \left(\frac{\{\Phi^{lw}\}_j^{n+1}}{\{t_l\}_j} + \frac{\{\Phi^{sw}\}_j^{n+1}}{\{t_s\}_j} \right), \\ [A^{ms}]_{jj} &= -\frac{\Delta t \{\Phi^{sw}\}_j^{n+1}}{\{\Phi^w\}_j^{n+1}} \left(\frac{1}{\{t_l\}_j} - \frac{1}{\{t_s\}_j} \right). \end{aligned}$$

The boundary conditions needs to be particularised as:

$$\frac{dw^m}{dz} = 0 ; \quad a_S^m = -1 ; \quad a_P^m = 1 ; \quad H^m = 0$$

at the top boundary ($j=N$) and as:

$$w^m = 0 ; \quad a_P^m = 1 ; \quad H^m = 0$$

at the bottom boundary ($j=0$).

A.2 Velocity predictor step

The equations for each phase are discretised with the same process as described above. The first step of the PISO algorithm consists in solving each momentum conservation equation without the excess pressure \bar{p}^f (fluid pressure without the hydrostatic) gradient. This predicts a velocity vector $\{w^i\}^*$ for each phase i , that does not account for the excess pressure. The discretised momentum conservation equation on each phase are presented below.

Mixture

From the discretised form (A.11), the predicted velocity vector $\{w^m\}^*$ at time $n + 1$ reads

$$\{w^m\}^* = [A^m]^{-1} \left[\{H^m\} - [A^{mf}] \{w^f\}^n - [A^{ms}] \{w^s\}^n \right] \quad (\text{A.13})$$

Small particles phase

The momentum conservation equation for the small particle phase reads

$$\begin{aligned} \frac{\partial w^s}{\partial t} + w^s \frac{\partial w^s}{\partial z} + \left(\frac{1}{t_s} + \frac{\Phi}{t_{ls}} \right) w^s &= -\frac{1}{\rho^p \Phi^s} \frac{\partial p^s}{\partial z} - \frac{1}{\rho^p} \frac{\partial \bar{p}^f}{\partial z} - \left(1 - \frac{\rho^f}{\rho^p} \right) g \cos \theta \\ &\quad + \frac{1}{t_{ls}} w^f + \frac{\Phi}{t_{ls}} w^m + \frac{\Phi^l}{\Phi^s \rho^p} \mathcal{F}(\mu) \frac{\partial p^m}{\partial z}. \end{aligned} \quad (\text{A.14})$$

At the predictor step, it can be discretised without its excess fluid pressure gradient as

$$\{w^s\}^* = [A^s]^{-1} \left[\{H^s\} - [A^{sf}] \{w^f\}^n - [A^{sm}] \{w^m\}^n \right] \quad (\text{A.15})$$

with its explicit part defined for cell j as

$$\{H^s\}_j = \{w^s\}_j^n - \Delta t \left(1 - \frac{\rho^f}{\rho^p} \right) g - \Delta t \frac{\{\Phi^{lw}\}_j^{n+1}}{\rho^p \{\Phi^{sw}\}_j^{n+1}} \{\mathcal{F}(\mu)\}_j \frac{\{p^m\}_j^{n+1} - \{p^m\}_{j-1}^{n+1}}{\Delta z}$$

and

$$[A^{sf}]_{jj} = -\frac{\Delta t}{\{t_s\}_j}$$

$$[A^{sm}]_{jj} = -\frac{\Delta t \{\Phi^w\}_j^{n+1} K_{ls}}{\{\Phi^{sw}\}_j^{n+1} \rho^p} \quad \text{with} \quad K_{ls} = \frac{18 \{\eta_p\}_j}{d_l^2}$$

Fluid phase

The momentum conservation equation for the fluid phase reads

$$\begin{aligned} \frac{\partial \epsilon w^f}{\partial t} + w^f \frac{\partial \epsilon w^f}{\partial z} + \left(\frac{\rho^p \Phi^s}{\rho^f \epsilon t_s} + \frac{\rho^p \Phi^l}{\rho^f \epsilon t_l} \right) w^f &= -\frac{1}{\rho^p} \frac{\partial \bar{p}^f}{\partial z} \\ &\quad - \frac{\rho^p \Phi^s}{\rho^f \epsilon} \left(\frac{1}{t_s} - \frac{1}{t_l} \right) w^s + \frac{\rho^p \Phi}{\rho^f \epsilon t_l} w^m. \end{aligned} \quad (\text{A.16})$$

At the predictor step, it can be discretised without is excess fluid pressure gradient as

$$\{w^f\}^* = [A^f]^{-1} [\{H^f\} - [A^{fm}] \{w^m\}^n - [A^{fs}] \{w^s\}^n] \quad (\text{A.17})$$

where the term $\{H^f\}$ is given by:

$$\{H^f\}_j = \{w^f\}_j^n$$

and the coupling matrix are given by:

$$\begin{aligned} [A^{fm}]_{jj} &= -\frac{\Delta t \rho^p \{\Phi^w\}_j^{n+1}}{\rho^f \{\epsilon\}_j^{n+1} \{t_l\}_j} \\ [A^{fs}]_{jj} &= -\frac{\Delta t \rho^p \{\Phi^{sw}\}_j^{n+1}}{\rho^f \{\epsilon\}_j^{n+1}} \left(\frac{1}{\{t_s\}_j} - \frac{1}{\{t_l\}_j} \right) \end{aligned}$$

A.3 Computing the pressure $\{p_f\}^*$

In this section, we show how the predicted velocities are used in the continuity equation to solve the excess fluid pressure \bar{p}^f . Once corrected, the total velocity field $\{w\}_j^{**} = \{\epsilon^w\}_j^n \{w^f\}_j^{**} + \{\Phi^w\}_j^n \{w^m\}_j^{**}$ should be divergence-free. This means that

$$\begin{aligned} \frac{\partial \{w\}^{**}}{\partial z} &= 0 \\ \Leftrightarrow \frac{\partial}{\partial z} \left(\{\epsilon^w\}_j^n \{w^f\}_j^{**} + \{\Phi^w\}_j^n \{w^m\}_j^{**} \right) &= 0 \end{aligned} \quad (\text{A.18})$$

$$\begin{aligned} \frac{\partial}{\partial z} \left[\left(\frac{\{\epsilon^w\}_j^{n+1} \Delta t}{\rho^f} [A^f]^{-1} + \frac{\{\Phi^w\}_j^{n+1} \Delta t}{\rho^p} [A^m]^{-1} \right) \frac{\partial \{p_f\}^*}{\partial z} \right] &= \\ \frac{\partial}{\partial z} \left(\{\epsilon^w\}_j^{n+1} \{w^f\}_j^* + \{\Phi^w\}_j^{n+1} \{w^m\}_j^* \right) & \quad (\text{A.19}) \end{aligned}$$

The finite volume formulation of Poisson equation gives:

$$\Leftrightarrow \left(\frac{\{\epsilon^w\}_{j+1}^{n+1}}{\rho^f} \Delta t [A^f]_{j,j+1}^{-1} + \frac{\{\Phi^w\}_{j+1}^{n+1}}{\rho^p} \Delta t [A^m]_{j,j+1}^{-1} \right) \frac{\{p_f\}_{j+1}^* - \{p_f\}_j^*}{\Delta z} - \left(\frac{\{\epsilon^w\}_j^{n+1}}{\rho^f} \Delta t [A^f]_j^{-1} + \frac{\{\Phi^w\}_j^{n+1}}{\rho^p} \Delta t [A^m]_j^{-1} \right) \frac{\{p_f\}_j^* - \{p_f\}_{j-1}^*}{\Delta z} = \{\epsilon^w\}_{j+1}^{n+1} \{w^f\}_{j+1}^* + \{\Phi^w\}_{j+1}^{n+1} \{w^m\}_{j+1}^* - \left(\{\epsilon^w\}_j^{n+1} \{w^f\}_j^* + \{\Phi^w\}_j^{n+1} \{w^m\}_j^* \right) \quad (\text{A.20})$$

By introducing the following notations: $\{w\}^* = \{\epsilon^w\}^{n+1} \{w^f\}^* + \{\Phi^w\}^{n+1} \{w^m\}^*$ and $[A] = \frac{\{\epsilon^w\}^{n+1}}{\rho^f} \Delta t [A^f]^{-1} + \frac{\{\Phi^w\}^{n+1}}{\rho^p} \Delta t [A^m]^{-1}$, this equation can be rewritten in compact form as:

$$[A]_{j,j+1} \frac{\{p_f\}_{j+1}^* - \{p_f\}_j^*}{\Delta z} - [A]_{j,j} \frac{\{p_f\}_j^* - \{p_f\}_{j-1}^*}{\Delta z} = \{w\}_{j+1}^* - \{w\}_j^* \quad (\text{A.21})$$

This equation can be recasted in a matrix form $[B]$ using the tridiagonal matrix coefficients:

$$\begin{aligned} a_N &= \frac{\Delta t}{\Delta z} [A]_{j,j+1} \\ a_S &= \frac{\Delta t}{\Delta z} [A]_{j,j} \\ a_P &= -(a_N + a_S) \end{aligned}$$

and the source term is written as:

$$H = \{w\}_{j+1}^* - \{w^m\}_j^*$$

In terms of boundary conditions, at the top boundary ($j = N$) a homogeneous Dirichlet condition is used, the fluid pressure is set to zero:

$$\bar{p}_f = 0 ; B_N = 1 ; H_N = 0.$$

At the bottom boundary ($j=0$), the pressure gradient is set to balance the mixture velocity flux:

$$\frac{\Delta t}{\Delta z} [A]_{11} \frac{d\bar{p}_f}{dz} = \{w^m\}_1^* ; [B]_{j,j+1} = 1/\Delta z ; [B]_{j,j} = 1/\Delta z ; H_j = \frac{\{w\}_1}{\Delta t [A]_{1,1}}$$

In a one-dimensional problem the solution of this equation is cheap and a simple double sweep algorithm can be used (Thomas, 1995) however for three-dimensional problems this can become very expensive as Bi-Conjugate Gradient algorithms might become necessary to resolve the algebraic system associated with the pressure equation.

A.4 Velocity corrector step

Using the newly computed excess pressure field $\{p_f\}^*$, we can correct the velocity fields:

$$\begin{aligned}\{w^f\}^{**} &= \{w^f\}^* - \frac{\Delta t}{\rho^f} [A^f]^{-1} \frac{\partial \{p_f\}^*}{\partial z} \\ \{w^m\}^{**} &= \{w^m\}^* - \frac{\Delta t}{\rho^p} [A^m]^{-1} \frac{\partial \{p_f\}^*}{\partial z} \\ \{w^s\}^{**} &= \{w^s\}^* - \frac{\Delta t}{\rho^p} [A^s]^{-1} \frac{\partial \{p_f\}_j^*}{\partial z}\end{aligned}$$

ANNEXE B

IMAGE VELOCIMETRY PROCESSING

The experimental velocity of the granular bed was determined using the *OpyFlow* package, developed by [Rousseau and Ancey \(2020\)](#) for the study of turbulent flows over permeable beds in mountain rivers. This toolbox is implemented in *Python* and is based on an optical flow method. The image velocimetry algorithm is briefly presented below but the interested reader will find more details in the PhD thesis of [Rousseau \(2019\)](#). This appendix is essentially dedicated to the validation of the velocity results provided by this toolbox.

B.1 The *OpyFlow* toolbox

The *OpyFlow* toolbox is based on the OpenCV library, written in Python. In *OpyFlow*, OpenCV provides the optical flow measurement algorithm, a method that allows one to determine the velocity fields on movies or image sequences. The algorithm is based on four steps.

B.1.1 Step 1: Selecting the *good features to track*

A first step consists in analysing the *good features to track* ([Shi and Tomasi, 1994](#)). These features are defined by the intersection between two edges, representing a high contrast point that can be robustly detected and therefore, that should provide an accurate estimation of the velocity when followed over the successive images. As an example, the good features detected for a bedload experiment, are shown with red markers in figure B.1. One can see that the features mainly correspond to the edge of the particles. Some outliers exist but they are usually not recovered in the next image and thus are not taken into account for the velocity estimation. Therefore, the velocities measured by the displacement of the good features correspond to the velocity of the granular bed.

With Particle Image Velocimetry (PIV) methods, the analysis is performed on the whole domain and the data providing a low-quality for the velocity estimation are discarded with post processing algorithms. Analysis of the *good features to track* avoids this post processing step and accelerates the process. Each feature detected is noted $\mathbf{c}_i = (x, z)_i^T$ and the velocimetry processing is performed on these points.

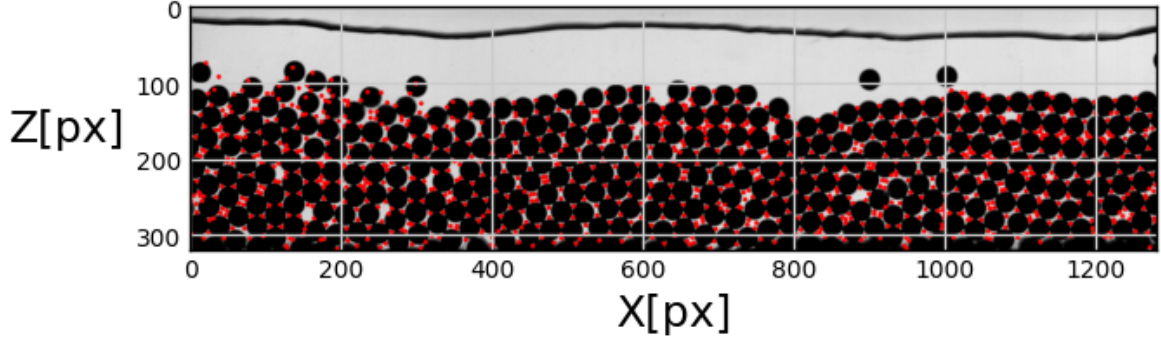


FIG. B.1: Good features to track (in red) detected on an image. One can see that the good features generally correspond to the edge of the particles.

B.1.2 Step 2: Velocimetry processing

The velocimetry processing is performed using an optical flow method which is based on two assumptions:

- The pixels in the neighbourhood $\mathbf{c}_i = (x, z)_i^T$ have the same velocities.
- The pixel intensities of a point $\mathbf{c}_i = (x, z)_i^T$ do not change with time.

From the second assumption, the intensity $\mathbf{I}(\mathbf{c}_i, t)$ of each feature $\mathbf{c}_i = (x, z)_i^T$ follows

$$\mathbf{I}(\mathbf{c}_i + \mathbf{d}\mathbf{c}_i, t + \delta t) = \mathbf{I}(\mathbf{c}_i, t), \quad (\text{B.1})$$

where $\mathbf{d}\mathbf{c}_i = (dx, dz)_i$ is the displacement of a feature between two consecutive images separated by a timestep δt .

With a Taylor series approximation, equation (B.1) can be linearised as

$$\frac{\partial \mathbf{I}}{\partial t} = \frac{\partial \mathbf{I}}{\partial x} u_i^s + \frac{\partial \mathbf{I}}{\partial z} w_i^s. \quad (\text{B.2})$$

Equation (B.2) contains two unknown variables, the streamwise velocity u_i^s and the vertical velocity w_i^s of the feature, which correspond respectively to the local streamwise and vertical granular bed velocities.

Several methods exist to determine both velocities from the single equation (B.2). The one implemented in OpenCV is based on a pyramidal implementation of the Lucas-Kanade method. With this method, the velocities are obtained thanks to a least square fit method on equation (B.1). For the reader interested, more details are given in the thesis of Rousseau (2019). The pyramidal implementation is a method consisting in reducing the resolution of the image in order to capture larger displacements. Each pyramidal level (1,2,3,...) makes it possible to divide successively the number of pixels in windows on the image and thus, a large displacement becomes a small displacement. In this experiment, we limit the method to 16×16 pixel windows and three pyramidal levels.

B.1.3 step 3: Interpolation scheme

The results of step 2 gives the local velocities u_i^s and w_i^s for each feature. In order to obtain a velocity field, Rousseau (2019) proposed to interpolate the velocity between

each value. Before the interpolation, two filters detect and delete potential outliers. The first filter deals with the isolated feature while the second filter compare the velocity of the feature with the local averaged velocity.

The interpolation is a Gaussian interpolation which uses the Visualization ToolKit (VTK) library that provides efficient detection of the closest neighbours. This step gives a velocity field over the image for both the streamwise and vertical velocities. These velocity fields are matrix of size $m \times n$ where m is the number of row and n the number of column. n and m do not have necessarily the same size as the image since the interpolation can be performed with a step made of several pixels. In this experiment, the interpolation step is chosen as 2 pixels in order to diminish the interpolation duration.

The interpolation can be made at each timestep or at the end, over all the velocities measured along the experiment duration. The first method is well adapted for unstationary flows, where the velocities at a given depth can change during the experiment. However, in our case, both the water and granular flows are supposed stationary and for a given depth, the velocities of each features should be similar. Performing the interpolation at the end, allows us to accumulate all the velocities over the experiment to obtain more data to interpolate. With this method, the interpolation should give more precise velocities.

B.1.4 step 4: Streamwise velocity profile

In the matrix $\bar{\mathbf{u}}^s$, each row corresponds to a depth and contains the streamwise velocities measured for this depth. In order to obtain the streamwise velocity profile, the values of each row are averaged:

$$\mathbf{u}^s = \left(\frac{1}{n} \sum_{j=0}^n \bar{\mathbf{u}}_{1j}^s, \frac{1}{n} \sum_{j=0}^n \bar{\mathbf{u}}_{2j}^s, \dots, \frac{1}{n} \sum_{j=0}^n \bar{\mathbf{u}}_{mj}^s \right)^T. \quad (\text{B.3})$$

B.2 Validation of the results

Some bedload experiments of Frey et al. (2020) (figure B.2) and Dudill et al. (2018) (figure B.3) were performed with a monodisperse bed in 2D ($W/d_s = 1$). Therefore, it was possible to track individually each particle using a PTV (Particle Tracking Velocimetry) algorithm (Lafaye de Micheaux et al., 2018). It provides datasets to assess the velocity profile predicted with the *OpyFlow* toolbox. Figures B.2 and B.3 present the results of the comparison. The images in B.2a and B.3a represent the velocity profiles detected with the PTV algorithm (orange circles) and the velocity profiles obtained with the optical flow method (red crosses). The images in B.2b and B.3b show the linear fits on these profiles. The bottom figures (in B.2c and B.3c) shows the error (in percent) on the fit of the velocity profile u^{opyf} obtained with the *OpyFlow* toolbox compared with the reference value u^{ref} obtained thanks to the PTV algorithm.

The linear fits in figures B.2b and B.3b show that the exponential profile of the granular bed streamwise velocity profile is recovered, with the optical flow method, down to five diameters for the experiment in figure B.2b and four diameters for the experiment in figure B.3c. The error plots B.2c and B.3c show that the error increases with depth. This is because for a given timestep δt , the displacements become smaller as the depth increases, making it difficult for the optical flow to detect the displacement deep in the bed. A solution consists in taking two consecutive images separated by a higher timestep. However, in this case, the optical flow method is not able to recover accurately the displacement near the bedline since the displacements will become too large. As our experiments are performed in the near bedline region, we preferred to have a small error in this region.

For the error plot B.2c, one can see that the error is lower than 70% until three diameters below the bedline and reaches 140% five diameters below the bed surface. We consider that this error is reasonable to validate the optical flow algorithm in this configuration. For the error plot B.3c, one can see that the error is lower than 100% until two diameters below the bedline and reaches 160% three diameters below the bed surface. The error is still reasonable in the near bed region but becomes more rapidly important with depth in this configuration.

The use of this algorithm seems to be easier than a classical PIV algorithm and Rousseau (2019) showed that it was more efficient. In addition, for porous media, the window on which the least square fit method is performed (see step 2) is lower due to the small pore size. This provides a highest quality of measurement and makes this method more accurate than PIV algorithm for porous bed (Rousseau, 2019). Regarding the results, I assume that this parametrisation of the optical flow algorithm can be validated for measuring the streamwise velocity profile of the granular bed in the near bedline region (until $h_b - z/d_s \sim 4$). This imposed to perform experiments between h_b and $h_b - z/d_s \sim 4$.

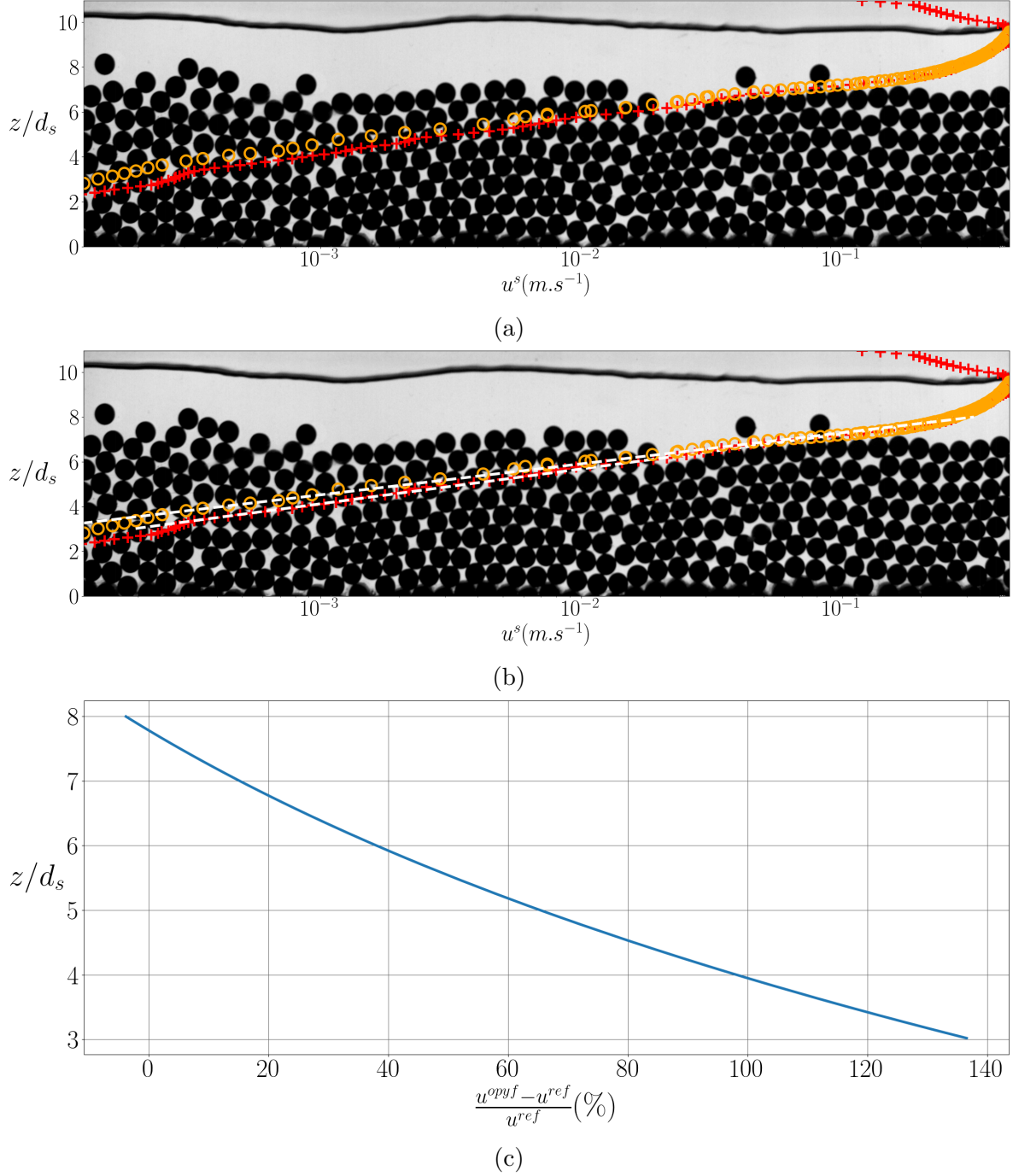


FIG. B.2: (a): Streamwise velocity profile of the granular bed measured with the PTV algorithm (○) and the *OpyFlow* toolbox (+) for the experiments of Frey et al. (2020). (b): Linear fits performed on both velocity profiles (white dashed lines). (c): Error, in percent, of the velocity measured with the *OpyFlow* toolbox u^{opyf} compared with the velocity measured with the PTV u^{ref} .

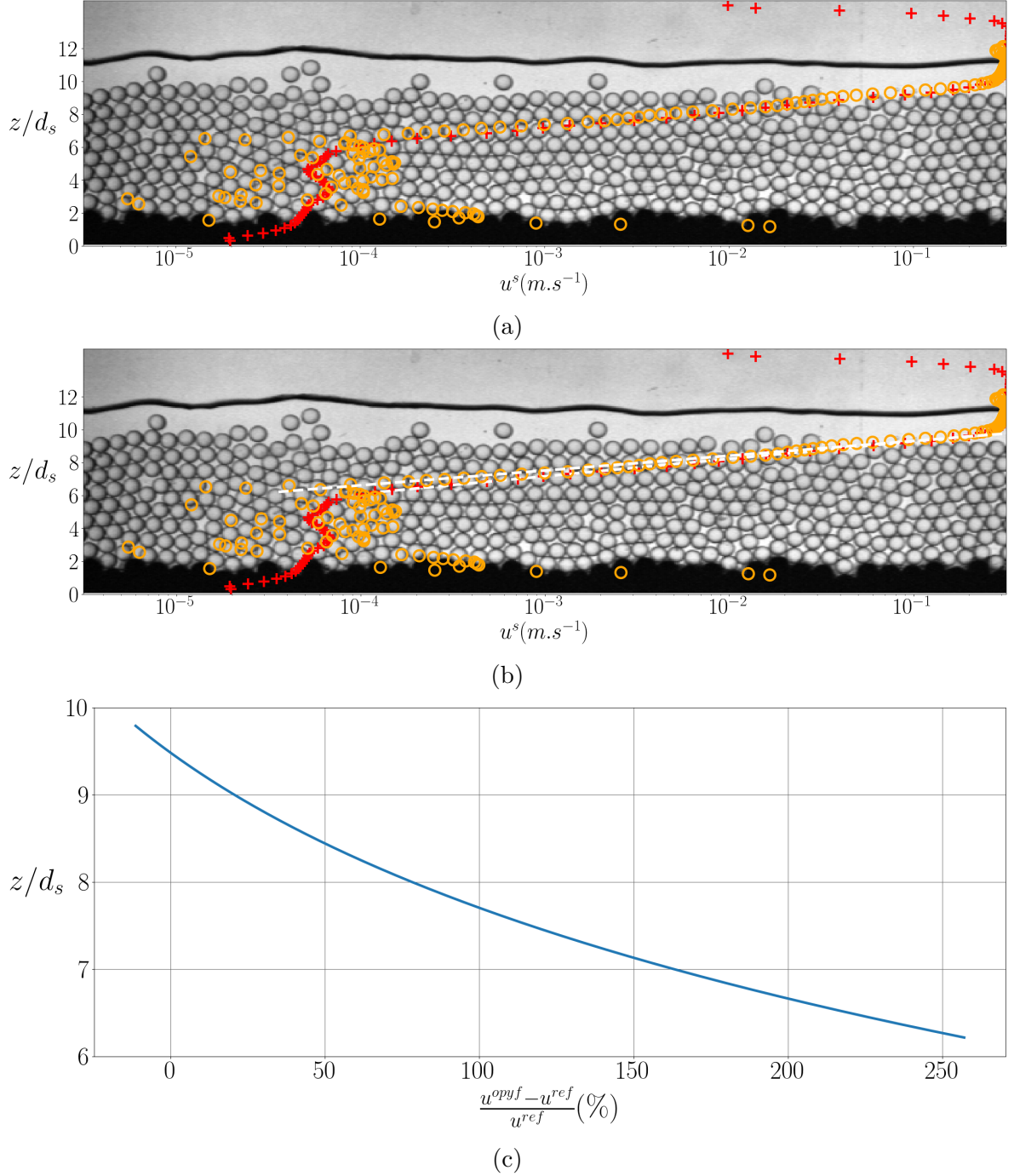


FIG. B.3: (a): Streamwise velocity profile of the granular bed measured with the PTV algorithm (\circ) and the *OpyFlow* toolbox ($+$) for the experiments of [Dudill et al. \(2018\)](#). (b): Linear fits performed on both velocity profiles (white dashed lines). (c): Error, in percent, of the velocity measured with the *OpyFlow* toolbox u^{opyf} compared with the velocity measured with the PTV u^{ref} .

ANNEXE C

VANONI AND BROOKS SIDEWALL CORRECTION

For steady and uniform flows, with slopes $\tan \theta = 0.1$, the dimensionless bed shear stress (called Shields number) is defined as (see equation (IV.5)):

$$\tau^* = \frac{R_h S}{(s - 1)d_{50}}, \quad (\text{C.1})$$

where $S = \sin \theta \sim \tan \theta$ since the angle of inclination θ (see figure IV.1) is small. However, this definition does not take into account the effect of the walls exerting a resistive force to the flow and thus diminishing the slope of energy. By dissipation of the energy, the bottom shear stress calculated with the water depth is therefore higher than it should be. To account for the wall effect, a bottom hydraulic radius R_{hb} is classically used and given by *Vanoni and Brooks*(1957). R_{hb} is the hydraulic radius that could be measured for the same mean velocity of the flow U in a flume without walls (infinitely large). As a consequence, R_{hb} is used to define dimensionless values, such as the Shields number, with no dependency with the geometry. Following *Vanoni and Brooks*(1957),

$$f_b = f + \frac{2h}{W}(f - f_w), \quad (\text{C.2})$$

where f , f_w and f_b are the Darcy Weissbach coefficients, respectively global, at the sidewalls and at the bottom. Using the equality between the slope

$$\theta = f \frac{U^2}{8R_h g} = f_w \frac{U^2}{8R_{hw} g} = f_b \frac{U^2}{8R_{hb} g}, \quad (\text{C.3})$$

one can obtain the following relation between the hydraulic radiiuses:

$$\frac{f}{R_h} = \frac{f_w}{R_{hw}} = \frac{f_b}{R_{hb}} \quad (\text{C.4})$$

The Reynold numbers are expressed with the hydraulic radius through:

$$Re_i = \frac{4R_{hi} U}{\nu} \quad (\text{C.5})$$

where i denotes for the wall, the bottom or the global coefficient. Introducing (C.5) in (C.4) it gives:

$$\frac{f}{Re} = \frac{f_w}{Re_w} = \frac{f_b}{Re_b} \quad (\text{C.6})$$

In equation (C.4), the only known values with global hydraulic radius are $R_h = hW/(2h + W)$,

$$f = \frac{8R_h g \theta}{U^2}$$

and f_b from equation (C.2).

Thus, f_w needs to be determined. From the Blasius smooth wall law (for $4000 < Re < 10000$):

$$f_w = \frac{0.24}{Re_w^{0.25}}$$

Using equation (C.6) it gives:

$$\rightarrow f_w = \frac{0.24}{(Re f_w/f)^{0.25}}$$

$$\rightarrow f_w^{1.25} = \frac{0.24}{(Re/f)^{0.25}},$$

which gives

$$f_w = \frac{0.320}{(Re/f)^{0.2}}. \quad (\text{C.7})$$

Using equations (C.2), (C.4) and (C.7), one can finally obtain

$$R_{hb} = \frac{R_h}{f} \left(f + \frac{2h}{W} \left(f - \frac{0.320}{\left(\frac{Re}{f}\right)^{0.2}} \right) \right) \quad (\text{C.8})$$

ANNEXE D

DETERMINATION OF THE PARTICLE VOLUME FRACTION

In a 2D configuration ($W/d_s = 1$), the granular volume fraction is accessible since all the particles are visible. When $W/d_s > 1$, the local number of particles per unit volume is not accessible anymore. In such a configuration, the use of the refractive index matching method associated with a laser sheet can be used (Rousseau and Ancey, 2020) to map the granular matrix and find the granular volume fraction. As the refractive index matching method is not developed in this work, another method is developed to approximate the maximum local volume fraction. It consists in taking off a volume V^{tot} on a portion of the bed defined between two sticks. This volume is presented in figure D.1 for a bed of 2mm. Then, the volume V^{tot} is weighted to determine its mass M .

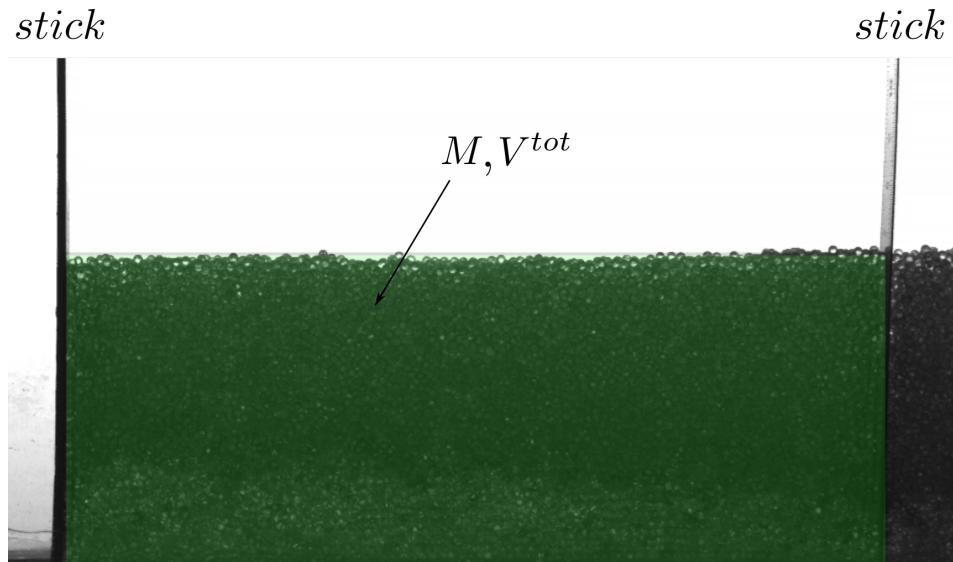


FIG. D.1: Image of the granular bed in the flume. The green area corresponds to the volume of particles that has been removed for the measuring of the volume fraction.

This gives the maximum volume fraction at rest in the bed $\Phi_{max} = M/\rho^p V^{tot}$, which is in particular used in the resolution of the Lagrangian equation of section IV.7.3. It is assumed that this value stays constant in the quasi-static regime since particle velocity fluctuations are small. Above, in the flowing regime, the dilatancy law could give the

link between the inertial number I and the local volume fraction $\Phi(z)$ as (Da Cruz et al., 2005; Jop et al., 2006)

$$\Phi(I) = \Phi_{max} - bI. \quad (\text{D.1})$$

Therefore, knowing the inertial number profile, one could determine the full volume fraction profile $\Phi(z)$ of the bed.

BIBLIOGRAPHIE

- Ancey, A. (2020). Bedload transport: a walk between randomness and determinism. part 2. challenges and prospects. *Journal of Hydraulic Research*, 58(1):18–33.
- Ancey, C., Coussot, P., and Evesque, P. (1999). A theoretical framework for granular suspensions in a steady simple shear flow. *Journal of Rheology*, 43(6):1673–1699.
- Andreotti, B., Forterre, Y., and Pouliquen, O. (2013). *Granular Media: Between Fluid and Solid*. Cambridge University Press.
- Aussillous, P., Chauchat, J., Pailha, M., Médale, M., and Guazzelli, E. (2013). Investigation of the mobile granular layer in bedload transport by laminar shearing flows. *Journal of Fluid Mechanics*, 736:594–615.
- Baumgarten, A. S. and Kamrin, K. (2019). A general fluid–sediment mixture model and constitutive theory validated in many flow regimes. *Journal of Fluid Mechanics*, 861:721–764.
- Berzi, D., Jenkins, J. T., and Richard, P. (2020). Extended kinetic theory for granular flow over and within an inclined erodible bed. *Journal of Fluid Mechanics*, 885:A27.
- Beschta, R. L. and Jackson, W. L. (1979). The intrusion of fine sediments into a stable gravel bed. *Journal of the Fisheries Research Board of Canada*, 36(2):204–210.
- Bouguet, J. (2000). Pyramidal implementation of the lucas kanade feature tracker. *Intel Corporation, Microprocessor Research Labs*.
- Bridgwater, J. (1976). Fundamental powder mixing mechanisms. *Powder Technology*, 15(2):215–236.
- Bridgwater, J., Foo, W., and Stephens, D. (1985). Particle mixing and segregation in failure zones—theory and experiment. *Powder Technology*, 41(2):147–158.
- Cai, R., Xiao, H., Zheng, J., and Zhao, Y. (2019). Diffusion of size bidisperse spheres in dense granular shear flow. *Physical Review E*, 99(3).
- Chassagne, R. (2020). *Discrete and continuum modelling of grain size segregation: application to bedload transport*. PhD thesis, Grenoble Alpes University.
- Chassagne, R., Frey, P., Maurin, R., and Chauchat, J. (2020a). Mobility of bidisperse mixtures during bedload transport. *Phys. Rev. Fluids*, 5:114307.
- Chassagne, R., Maurin, R., Chauchat, J., Gray, J. M. N. T., and Frey, P. (2020b). Discrete and continuum modelling of grain size segregation during bedload transport. 895:A30.
- Chauchat, J. (2018). A comprehensive two-phase flow model for unidirectional sheet-flows. *Journal of Hydraulic Research*, 56(1):15–28.

BIBLIOGRAPHIE

- Chauchat, J., Cheng, Z., Nagel, T., Bonamy, C., and Hsu, T.-J. (2017). SedFoam-2.0: A 3-D two-phase flow numerical model for sediment transport. *Geoscientific Model Development*, 10(12):4367–4392.
- Choi, J., Kudrolli, A., Rosales, R. R., and Bazant, M. Z. (2004). Diffusion and mixing in gravity-driven dense granular flows. *Phys. Rev. Lett.*, 92:174301.
- Cui, Y., Parker, G., Lisle, T. E., Gott, J., Hansler-Ball, M. E., Pizzuto, J. E., Allmendinger, N. E., and Reed, J. M. (2003). Sediment pulses in mountain rivers: 1. experiments. *Water Resources Research*, 39(9).
- Da Cruz, F., Emam, S., Prochnow, M., Roux, J.-N., and Chevoir, F. (2005). Rheophysics of dense granular materials: Discrete simulation of plane shear flows. *Physical Review E*, 72(2).
- Denissen, I. F. C., Weinhart, T., Te Voortwijk, A., Luding, S., Gray, J. M. N. T., and Thornton, A. R. (2019). Bulbous head formation in bidisperse shallow granular flow over an inclined plane. *Journal of Fluid Mechanics*, 866:263–297.
- Ding, Y., Gravish, N., and Goldman, D. I. (2011). Drag Induced Lift in Granular Media. *Physical Review Letters*, 106(2):028001.
- Dolgunin, V., Kudy, A., and Ukolov, A. (1998). Development of the model of segregation of particles undergoing granular flow down an inclined chute. *Powder Technology*, 96(3):211–218.
- Dolgunin, V. N. and Ukolov, A. A. (1995). Segregation modeling of particle rapid gravity flow. *Powder Technology*, 83(2):95–103.
- Duan, Y., Umbanhowar, P. B., Ottino, J. M., and Lueptow, R. M. (2020). Segregation models for density-bidisperse granular flows. *Phys. Rev. Fluids*, 5:044301.
- Dudill, A., Frey, P., and Church, M. (2017). Infiltration of fine sediment into a coarse mobile bed: A phenomenological study. *Earth Surface Processes and Landforms*, 42(8):1171–1185.
- Dudill, A., Lafaye de Micheaux, H., Frey, P., and Church, M. (2018). Introducing Finer Grains Into Bedload: The Transition to a New Equilibrium. *Journal of Geophysical Research: Earth Surface*, 123(10):2602–2619.
- Duran, J., Rajchenbach, J., and Clément, E. (1993). Arching effect model for particle size segregation. *Phys. Rev. Lett.*, 70:2431–2434.
- Egiazaroff, I. V. (1965). Calculation of nonuniform sediment concentrations. *Journal of the Hydraulics Division*, 91(4):225–247.
- Einstein, H. A. (1942). Formulas for the transportation of bed load. *Transactions of the American Society of Civil Engineers*, 107(1):561–577.
- Fan, Y., Schlick, C. P., Umbanhowar, P. B., Ottino, J. M., and Lueptow, R. M. (2014a). Modelling size segregation of granular materials: The roles of segregation, advection and diffusion. *Journal of Fluid Mechanics*, 741:252–279.
- Fan, Y., Schlick, C. P., Umbanhowar, P. B., Ottino, J. M., and Lueptow, R. M. (2014b). Modelling size segregation of granular materials: the roles of segregation, advection and diffusion. *Journal of Fluid Mechanics*, 741:252–279.
- Fan, Y., Umbanhowar, P. B., Ottino, J. M., and Lueptow, R. M. (2015). Shear-rate-independent diffusion in granular flows. *Phys. Rev. Lett.*, 115:088001.
- Ferdowsi, B., Ortiz, C. P., Houssais, M., and Jerolmack, D. J. (2017). River-bed armouring as a granular segregation phenomenon. *Nature Communications*, 8(1).

- Ferguson, R. and Church, M. (2004). A simple universal equation for grain settling velocity. *Journal of Sedimentary Research*, 74(6):933–937.
- Ferguson, R. I., Prestegaard, K. L., and Ashworth, P. J. (1989). Influence of sand on hydraulics and gravel transport in a braided gravel bed river. *Water Resources Research*, 25(4):635–643.
- Forterre, Y. and Pouliquen, O. (2008). Flows of dense granular media. *Annual Review of Fluid Mechanics*, 40(1):1–24.
- Frey, P. and Church, M. (2009). How River Beds Move. *Science*, 325(5947):1509–1510.
- Frey, P. and Church, M. (2011). Bedload: A granular phenomenon. *Earth Surface Processes and Landforms*, 36(1):58–69.
- Frey, P., Lafaye de Micheaux, H., Bel, C., Maurin, R., Rorsman, K., Martin, T., and Ducottet, C. (2020). Experiments on grain size segregation in bedload transport on a steep slope. *Advances in Water Resources*, 136:103478.
- Fry, A. M., Umbanhowar, P. B., Ottino, J. M., and Lueptow, R. M. (2018). Effect of pressure on segregation in granular shear flows. *Physical Review E*, 97(6-1):062906.
- Fry, A. M., Umbanhowar, P. B., Ottino, J. M., and Lueptow, R. M. (2019). Diffusion, mixing, and segregation in confined granular flows. *AICHE Journal*, 65(3):875–881.
- GDR MiDi (2004). On dense granular flows. *The European Physical Journal E*, 14(4):341–365.
- Gibson, S., Abraham, D., Heath, R., and Schoellhamer, D. (2010). Bridging process threshold for sediment infiltrating into a coarse substrate. *Journal of Geotechnical and Geoenvironmental Engineering*, 136(2):402–406.
- Gilbert, G. K. and Murphy, E. C. (1914). *The Transportation of Debris by Running Waters*. Professional paper 86, U.S. Geological Survey, Washington DC, 261 pp.
- Golick, L. A. and Daniels, K. E. (2009). Mixing and segregation rates in sheared granular materials. *Physical Review E*, 80(4):042301.
- Gomez, B. (1991). Bedload transport. *Earth-Science Reviews*, 31(2):89–132.
- Graf, W. H. and Pazis, G. C. (1977). Desposition and erosion in an alluvial channel. *Journal of Hydraulic Research*, 15(2):151–166.
- Gray, J. and Thornton, A. (2005). A theory for particle size segregation in shallow granular free-surface flows. *Proceedings of the Royal Society A: Mathematical, Physical and Engineering Sciences*, 461(2057):1447–1473.
- Gray, J. M. N. T. (2018). Particle Segregation in Dense Granular Flows. *Annual Review of Fluid Mechanics*, 50(1):407–433.
- Gray, J. M. N. T. and Ancey, C. (2011). Multi-component particle-size segregation in shallow granular avalanches. *Journal of Fluid Mechanics*, 678:535–588.
- Gray, J. M. N. T. and Chugunov, V. A. (2006). Particle-size segregation and diffusive remixing in shallow granular avalanches. *Journal of Fluid Mechanics*, 569:365–398.
- Guazzelli, Å., Morris, J. F., and Pic, S. (2011). *Shear flow*, pages 155–191. Cambridge Texts in Applied Mathematics. Cambridge University Press.
- Guillard, F., Forterre, Y., and Pouliquen, O. (2014). Lift forces in granular media. *Physics of Fluids*, 26(4):043301.
- Guillard, F., Forterre, Y., and Pouliquen, O. (2016). Scaling laws for segregation forces in dense sheared granular flows. *Journal of Fluid Mechanics*, 807:R1.

BIBLIOGRAPHIE

- Hergault, V., Frey, P., Métivier, F., Barat, C., Ducottet, C., Böhm, T., and Ancey, C. (2010). Image processing for the study of bedload transport of two-size spherical particles in a supercritical flow. *Experiments in Fluids*, 49(5):1095–1107.
- Hill, K. and Tan, D. (2014). Segregation in dense sheared flows: gravity, temperature gradients, and stress partitioning. *Journal of Fluid Mechanics*, 756:54–88.
- Hill, K. M., Gaffney, J., Baumgardner, S., Wilcock, P., and Paola, C. (2017). Experimental study of the effect of grain sizes in a bimodal mixture on bed slope, bed texture, and the transition to washload. *Water Resources Research*, 53(1):923–941.
- Houssais, M. and Lajeunesse, E. (2012). Bedload transport of a bimodal sediment bed. *Journal of Geophysical Research: Earth Surface*, 117(F4).
- Ikeda, H. and Iseya, F. (1988). *Experimental Study of Heterogeneous Sediment Transport*. Environmental Research Center papers. Environmental Research Center, University of Tsukuba.
- Iseya, F. and Ikeda, H. (1987). Pulsations in bedload transport rates induced by a longitudinal sediment sorting: A flume study using sand and gravel mixtures. *Geografiska Annaler: Series A, Physical Geography*, 69(1):15–27.
- Jackson, R. (1997). Locally averaged equations of motion for a mixture of identical spherical particles and a Newtonian fluid. *Chemical Engineering Science*, 52(15):2457–2469.
- Jackson, R. (2000). *The Dynamics of Fluidized Particles*. Cambridge Monographs on Mechanics. Cambridge University Press, Cambridge ; New York.
- Jenkins, J. T. and Richman, M. W. (1985). Kinetic theory for plane flows of a dense gas of identical, rough, inelastic, circular disks. *The Physics of Fluids*, 28(12):3485–3494.
- Jha, S. K. and Bombardelli, F. A. (2010). Toward two-phase flow modeling of nondilute sediment transport in open channels. *Journal of Geophysical Research: Earth Surface*, 115(F3).
- Jing, L., Ottino, J. M., Lueptow, R. M., and Umbanhowar, P. B. (2020). Rising and sinking intruders in dense granular flows. *Phys. Rev. Research*, 2:022069.
- Johnson, P. C. and Jackson, R. (1987). Frictional–collisional constitutive relations for granular materials, with application to plane shearing. *Journal of Fluid Mechanics*, 176:67–93.
- Jones, R. P., Isner, A. B., Xiao, H., Ottino, J. M., Umbanhowar, P. B., and Lueptow, R. M. (2018). Asymmetric concentration dependence of segregation fluxes in granular flows. *Physical Review Fluids*, 3(9).
- Jop, P. (2015). Rheological properties of dense granular flows. *Comptes Rendus Physique*, 16(1):62–72. Granular physics / Physique des milieux granulaires.
- Jop, P., Forterre, Y., and Pouliquen, O. (2005). Crucial role of sidewalls in granular surface flows: consequences for the rheology. *Journal of Fluid Mechanics*, 541:167–192.
- Jop, P., Forterre, Y., and Pouliquen, O. (2006). A constitutive law for dense granular flows. *Nature*, 441(7094):727–730.
- Jullien, R., Meakin, P., and Pavlovitch, A. (1992). Three-dimensional model for particle-size segregation by shaking. *Phys. Rev. Lett.*, 69:640–643.
- Kamrin, K. and Koval, G. (2012). Nonlocal constitutive relation for steady granular flow. *Phys. Rev. Lett.*, 108:178301.

- Knight, J., Jaeger, J., and Nagel, S. (1993). Vibration-induced size separation in granular media: The convection connection. *Physical Review Letters*, 70(24):3728–3731.
- Lafaye de Micheaux, H., Ducottet, C., and Frey, P. (2018). Multi-model particle filter-based tracking with switching dynamical state to study bedload transport. *Machine Vision and Applications*, 29(5):735–747.
- Lafaye de Micheaux, H., Dudill, A., Frey, P., and Ducottet, C. (2015). Image processing to study the evolution of channel slope and water depth in bimodal sediment mixtures. In *10th Pacific Symposium on Flow Visualization and Image Processing*, number 43, pages 735–747.
- Lajeunesse, E., Malverti, L., and Charru, F. (2010). Bed load transport in turbulent flow at the grain scale: Experiments and modeling. *Journal of Geophysical Research: Earth Surface*, 115(F4).
- Lantman, M. P. v. S., van der Vaart, K., Luding, S., and Thornton, A. R. (2021). Granular buoyancy in the context of segregation of single large grains in dense granular shear flows. *Phys. Rev. Fluids*, 6:064307.
- Lee, C.-H. and Huang, Z. (2018). A two-phase flow model for submarine granular flows: With an application to collapse of deeply-submerged granular columns. *Advances in Water Resources*, 115:286–300.
- Marty, G. and Dauchot, O. (2005). Subdiffusion and cage effect in a sheared granular material. *Phys. Rev. Lett.*, 94:015701.
- Maurin, R., Chauchat, J., Chareyre, B., and Frey, P. (2015). A minimal coupled fluid-discrete element model for bedload transport. *Physics of Fluids*, 27(11):113302.
- Maurin, R., Chauchat, J., and Frey, P. (2016). Dense granular flow rheology in turbulent bedload transport. *Journal of Fluid Mechanics*, 804:490–512.
- Maurin, R., Chauchat, J., and Frey, P. (2018). Revisiting slope influence in turbulent bedload transport: consequences for vertical flow structure and transport rate scaling. *Journal of Fluid Mechanics*, 839:135–156.
- Meyer-Peter, E. and Müller, R. (1948). Formulas for bed-load transport. Technical report, IAHR.
- Montgomery, D. R., Panfil, M. S., and Hayes, S. K. (1999). Channel–bed mobility response to extreme sediment loading at mount pinatubo. *Geology*, 27(3):271–274.
- Morland, L. W. (1992). Flow of viscous fluids through a porous deformable matrix. *Surveys in Geophysics*, 13(3):209–268.
- Nagel, T., Chauchat, J., Bonamy, C., Liu, X., Cheng, Z., and Hsu, T.-J. (2020). Three-dimensional scour simulations with a two-phase flow model. *Advances in Water Resources*, 138:103544.
- Ni, W. and Capart, H. (2015). Cross-sectional imaging of refractive-index-matched liquid-granular flows. *Experiments in Fluids*, 56(163).
- O'Donoghue, T. and Wright, S. (2004). Concentrations in oscillatory sheet flow for well sorted and graded sands. *Coastal Engineering*, 50(3):117 – 138.
- Proffitt, G. and Sutherland, A. (1983). Transport of non-uniform sediments. *Journal of Hydraulic Research*, 21(1):33–43.
- Recking, A. (2010). A comparison between flume and field bed load transport data and consequences for surface-based bed load transport prediction. *Water Resources Research*, 46(3).

BIBLIOGRAPHIE

- Recking, A. (2013). An analysis of nonlinearity effects on bed load transport prediction. *Journal of Geophysical Research: Earth Surface*, 118(3):1264–1281.
- Recking, A., Liébault, F., Peteuil, C., and Jolimet, T. (2012). Testing bedload transport equations with consideration of time scales. *Earth Surface Processes and Landforms*, 37(7):774–789.
- Richardson, J. F. and Zaki, W. N. (1954). The sedimentation of a suspension of uniform spheres under conditions of viscous flow. *Chemical Engineering Science*, 3(2):65–73.
- Rosato, A., Strandburg, K. J., Prinz, F., and Swendsen, R. H. (1987). Why the brazil nuts are on top: Size segregation of particulate matter by shaking. *Phys. Rev. Lett.*, 58:1038–1040.
- Rousseau, G. (2019). *Turbulent Flows over Rough Permeable Beds in Mountain Rivers: Experimental Insights and Modeling*. PhD thesis, Lausanne, EPFL.
- Rousseau, G. and Ancey, C. (2020). Scanning piv of turbulent flows over and through rough porous beds using refractive index matching. *Experiments in Fluids*, 61(172).
- Rousseau, H., Chassagne, R., Chauchat, J., Maurin, R., and Frey, P. (2021). Bridging the gap between particle-scale forces and continuum modelling of size segregation: application to bedload transport. *Journal of Fluid Mechanics*, 916:A26.
- Rusche, H. (2003). *Computational fluid dynamics of dispersed two-phase flows at high phase fractions*. PhD thesis, Imperial College London (University of London).
- Savage, S. B. and Lun, C. K. K. (1988). Particle size segregation in inclined chute flow of dry cohesionless granular solids. *Journal of Fluid Mechanics*, 189:311–335.
- Schlick, C. P., Fan, Y., Isner, A. B., Umbanhowar, P. B., Ottino, J. M., and Lueptow, R. M. (2015). Modeling segregation of bidisperse granular materials using physical control parameters in the quasi-2d bounded heap. *AICHE Journal*, 61(5):1524–1534.
- Shi, J. and Tomasi (1994). Good features to track. In *1994 Proceedings of IEEE Conference on Computer Vision and Pattern Recognition*, pages 593–600.
- Shields, A. (1936). Application of similarity principles and turbulence research to bed-load movement. Technical report, California Institute of Technology.
- Stokes, G. G. (1851). *Mathematical and Physical Papers*. Cambridge University Press, Cambridge.
- Thomas, J. (1995). *Numerical Partial Differential Equations: Finite Difference Methods*. Springer-Verlag New York.
- Thomas, N. (2000). Reverse and intermediate segregation of large beads in dry granular media. *Physical Review E*, 62(1):961–974.
- Thornton, A. R., Gray, J. M. N. T., and Hogg, A. J. (2006). A three-phase mixture theory for particle size segregation in shallow granular free-surface flows. *Journal of Fluid Mechanics*, 550:1–25.
- Tripathi, A. and Khakhar, D. V. (2011). Numerical simulation of the sedimentation of a sphere in a sheared granular fluid: A granular stokes experiment. *Phys. Rev. Lett.*, 107:108001.
- Tripathi, A. and Khakhar, D. V. (2013). Density difference-driven segregation in a dense granular flow. *Journal of Fluid Mechanics*, 717:643–669.
- Tunuguntla, D. R. and Thornton, A. R. (2017). Balancing size and density segregation in bidisperse dense granular flows. *EPJ Web Conf.*, 140:03079.

- Turowski, J. M., RICKENMANN, D., and DADSON, S. J. (2010). The partitioning of the total sediment load of a river into suspended load and bedload: a review of empirical data. *Sedimentology*, 57(4):1126–1146.
- Umbanhowar, P. B., Lueptow, R. M., and Ottino, J. M. (2019). Modeling segregation in granular flows. *Annual Review of Chemical and Biomolecular Engineering*, 10(1):129–153. PMID: 30883215.
- Van der Vaart, K., Gajjar, P., Epely-Chauvin, G., Andreini, N., Gray, J. M. N. T., and Ancey, C. (2015). Underlying Asymmetry within Particle Size Segregation. *Physical Review Letters*, 114(23).
- Van der Vaart, K., van Schroyenstein Lantman, M. P., Weinhart, T., Luding, S., Ancey, C., and Thornton, A. R. (2018). Segregation of large particles in dense granular flows suggests a granular Saffman effect. *Physical Review Fluids*, 3(7).
- Venditti, J. G., Dietrich, W. E., Nelson, P. A., Wydzga, M. A., Fadde, J., and Sklar, L. (2010). Effect of sediment pulse grain size on sediment transport rates and bed mobility in gravel bed rivers. *Journal of Geophysical Research: Earth Surface*, 115(F3).
- Wiederseiner, S., Andreini, N., Epely-Chauvin, G., Moser, G., Monnereau, M. L., Gray, J. M., and Ancey, C. (2011). Experimental investigation into segregating granular flows down chutes. *Physics of Fluids*, 23(013301).
- Wilcock, P. R. and Crowe, J. C. (2003). Surface-based transport model for mixed-size sediment. *Journal of Hydraulic Engineering*, 129(2):120–128.
- Wong, M. and Parker, G. (2006). Reanalysis and correction of bed-load relation of meyer-peter and müller using their own database. *Journal of Hydraulic Engineering*, 132(11):1159–1168.
- Woodhouse, M. J., Thornton, A. R., Johnson, C. G., Kokelaar, B. P., and Gray, J. M. N. T. (2012). Segregation-induced fingering instabilities in granular free-surface flows. *Journal of Fluid Mechanics*, 709:543–580.
- Zhu, Y., Delannay, R., and Valance, A. (2020). High-speed confined granular flows down smooth inclines: scaling and wall friction laws. *Granular Matter*, 22:22.